FPGA-based algorithms for the stability improvement of high-flux X-ray spectrometric imaging detectors.

Cinzia de Cesare

Communauté
UNIVERSITÉ Grenoble Alpes

THÈSE

Pour obtenir le grade de

DOCTEUR DE LA COMMUNAUTÉ UNIVERSITÉ GRENOBLE ALPES

Spécialité : NANO ELECTRONIQUE ET NANO TECHNOLOGIES

Arrêté ministériel : 25 mai 2016

Présentée par

Cinzia DE CESARE

Thèse dirigée par **Olivier ROSSETTO**, UGA

préparée au sein du **Laboratoire CEA/LETI**
dans **l'École Doctorale Electronique, Electrotechnique, Automatique, Traitement du Signal (EEATS)**

Traitements numériques pour l'amélioration de la stabilité des détecteurs spectrométriques à fort flux pour l'imagerie X

FPGA-based algorithms for the stability improvement of high-flux X-ray spectrometric imaging detectors.

Thèse soutenue publiquement le **17 octobre 2018**,
devant le jury composé de :

Monsieur OLIVIER ROSSETTO
MAITRE DE CONFERENCES, UNIVERSITE GRENOBLE ALPES, Directeur de thèse
Monsieur LEONARDO ABBENE
PROFESSEUR ASSOCIE, UNIVERSITE DE PALERME - ITALIE, Rapporteur
Monsieur GILLES BAN
PROFESSEUR, ENSICAEN, Rapporteur
Monsieur FRANCIS CALMON
PROFESSEUR, INSA LYON, Président
Monsieur JOHANN COLLOT
PROFESSEUR, UNIVERSITE GRENOBLE ALPES, Examinateur
Monsieur ANDREA BRAMBILLA
INGENIEUR DE RECHERCHE, CEA GRENOBLE, Examinateur

LIST OF ACRONYMS

ADC	Analog to Digital Converter
ASIC	Application Specific Integrated Circuit
BLR	BaseLine Restorer
BD	Ballistic Deficit
CT	Computed Tomography
CR	Compute Radiography
DR	Digital Radiography
CSA	Charge Sensitive Amplifier
CSM	Charge Summing Mode
CSD	Charge Sharing Discrimination
CSA	Charge Sharing Addition
CDM	Cross Detection Method
DSO	Digital Storage Oscilloscope
DPP	Digital Pulse Processing
EMA	Exponential Moving Average
FPGA	Field Programmable Gate Array
FWHM	Full Width at Half Maximum
LDET	Laboratory DETector
MSEC	Multi-Site Event Cancellation
MEPCD	Multi-energy Photon Counting Detector
MA	Moving Average
NTD	Non-Destructive Test
PCD	Photon Counting Detector
PMT	Photo-Multiplier
PET	Positron Emission Tomography
PUR	Pile-up Rejection
PSHA	Pulse Shape Height Analysis
PHS	Pulse Height Spectrum
SDL	Single Delay Line
SNR	Signal to Noise Ratio
SPM	Single Pixel Mode
TFA	Time Filter Amplifier
TCA	Time Coincidence Analysis
TOT	Time Over Threshold
TCW	Time Coincident Window
TW	Time Window
XRF	X-Ray Florescence
VHDL	Very high speed integrated circuit Hardware Description Language

LIST OF SYMBOLS

CdTe	Cadmium Tellurium
CdZnTe	Cadmium Zinc Tellurium
cps	Counts per Second
E_{gap}	Energy gap
E_W	Weighting field
ϵ	Ionization potential
ΔT	Acquisition Time Window
Ge	Germanium
HPGe	Hyper Pure Germanium
N(E)	Number of incident photons with energy E
ρ	Density
σ	Standard deviation
Si	Silicon
T_D	Delay time
T_P	Peaking time
T_{clock}	Clock time
τ_F	Decay time
$Q_{induced}$	Induced charge
V_W	Weighting potential
Z	Atomic number

Contents

Introduction

Since the discovery of X-rays by Röntgen in 1895, numerous applications for X-ray imaging have emerged, ranging from medical diagnostic to security and Non-Destructive Testing (NTD) for industry. Significant advances can be observed in the design of all X-ray system components such as X-ray tubes, generators, detectors, collimators, computed tomography (CT) gantries and signal processing algorithms. In the last few decades important progress in X-ray detection technology have been achieved. In particular, in the beginning of the 1990s, analog film detection has been replaced by the digital technique known as Computed Radiography (CR). Then, in early 21st century, real-time digital X-ray detection technology, known as Digital Radiography (DR), has been introduced. This type of detectors convert X-rays into electrical signals either through indirect or direct conversion. For the last few years, new digital X-ray detector capabilities have been investigated. For a given pixel, conventional X-ray detectors provide a signal proportional to the photon energy deposited into the detector element, integrated on the total energy range. Recently-emerged room-temperature semiconductor photon counting detectors (PCDs) exhibit the ability to classify photons into several discrete energy channels, the number of which varies from a few bins (typically from 2 to 8) [1]-[7] to 256 or more, depending on the electronic circuit [8]-[11]. This new technology allows the development of energy-resolved imaging for all current X-ray applications [11]. Spectral imaging can provide compositional information on the analysed object, which can be exploited for material identification. This capability is used in the luggage control field to detect illegal materials [12]-[14] and in the medical field, for the quantification of tissue composition and contrast agent concentrations [15]-[17].

The photon fluxes involved in spectrometric applications are high (up to 10^8 $X/mm^2/s$) and with the increase of the flux the phenomenon of pile-up becomes more and more important. In order not to lose pulses during the digital signal processing, it is important to use a fast shaping circuit, that correctly distinguishes the pulses affected by pile-up and recovers the right energy information from them.

If the shaping time employed is faster than the charge collection time, the detector works in ballistic deficit regime [18]-[21]. The energy information obtained is still proportional to the released energy by the photon in the detector. However, we have observed that the ballistic deficit is variable and that the response of the detector varies over time. These variations are attributed to the modification of the internal electrical field profile as a result of trapping and de-trapping phenomena. The resulting instability of the response has a detrimental effect on the detector performances.

The objective of this thesis work is to develop a real-time digital algorithm implementable in FPGA that corrects these variations and gives a stable response of the detector over time at very high fluxes. The CdTe pixel detector (4x4) is coupled to an innovative custom-designed digital readout electronics able to continuously digitize and process the signals from each pixel (16 in total), providing the energy binning (up to 256 channels) and performing analysis even at very high fluxes. The digital pulse processing (DPP) for the compensation of the detector instabilities uses a fast shaping filter for the distinction of pile-up events and a slow shaping filter for the estimation of the total collected charge and thus of the ballistic deficit. It is then possible to compensate the effect of the variation of the ballistic deficit over time while preserving the energy resolution and the count rate capability of the system both at low and high flux.

This document is divided in 6 Chapters. Chapter 1 presents the different X-ray imaging detectors focusing on spectrometric detectors. It discusses the physics of these detectors together with the effect of pile-up, charge sharing, weighting potential cross-talk and ballistic deficit. Moreover, it presents the state of the art of the correction techniques used to process these effects.

In Chapter 2, the read-out electronic developed in LDET is presented together with the pulse processing algorithm adapted to the spectrometric pixel detector. In this Chapter we also present the characterization of the pixel detector performed during this thesis work. Special attention is given to the shaping circuit configuration which determines the performance of the detector in terms of energy resolution and counting rate. We will show that the use of a Single Delay Line shaping amplifier with a short time constant and an appropriate pre-filter stage is a good compromise for high count rate spectrometric applications, despite the fact that it introduces a ballistic deficit.

Chapter 3 and 4 are the heart of the work of this thesis. In Chapter 3 the mechanisms responsible of the instability of the detector response are described in detail. An accurate study on the causes of this instability performed through experimental observations and model simulations show that instabilities are related to fluctuation of the ballistic deficit due to the modification of the internal electrical field profile over time. Chapter 4 describes the main contributions of this thesis work and introduces a novel method for the compensation of the unstable response of the detector over time. Its principle and its characterization are first described. After this, we discuss the importance of rejecting undesirable effects such as pile-up, charge sharing and weighting potential cross-talk affecting the correct compensation of the ballistic deficit. At the end of the Chapter, we discuss the implementation of the proposed method on FPGA and the adaptations done in order to obtain a suitable version working in real-time.

In Chapter 5 we evaluate the real-time digital algorithm implemented on FPGA by measurements at low count rate with a ^{57}Co and ^{241}Am γ-ray sources and at high count rates with an X-ray beam, with a count rate up to 2 Mc/s. It follows a discussion on the results obtained.

Finally, we will conclude with a global overview on the results, the improvement obtained with this method in relation to the already existing approaches for the mitigation or elimination of the detector instability and the future perspectives of this thesis work.

Chapter 1

X-ray detectors

1.1 Detectors for X-ray imaging

X-ray detectors are devices used to measure the intensity, the spatial and energy distribution of X-rays beams. Since the discovery of X-rays, different technologies have been developed and many of them are still in use. We can distinguish two types of detectors: the *indirect* conversion detectors and the *direct* conversion one. Indirect conversion detectors are able to convert the incident X-ray photon in light, as Fig. 1.1 shows. The light is converted in electrical signal by a photo-multiplier (PMT) or by photo-diode array. In this first category we can find anger cameras made by scintillator layers and PMT for nuclear medicine applications, scintillator with photo-diodes for digital radiology applications [22] and avalanche photo-diodes for positron-emission tomography (PET) [23].

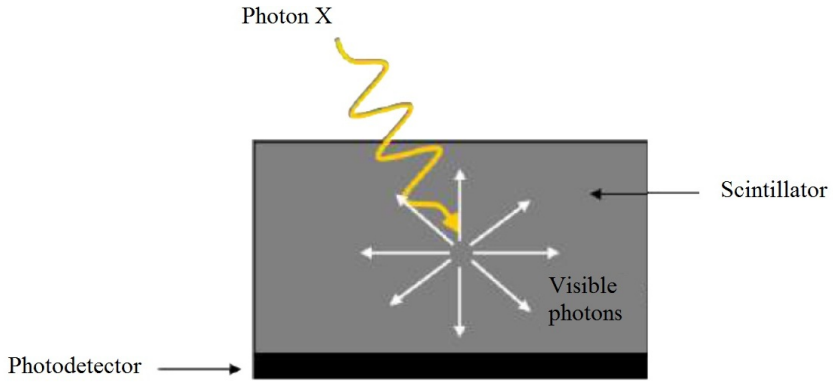

Figure 1.1: Scheme of the principle of indirect conversion detector.

Direct conversion detectors are based on semiconductor materials, such as Silicon (Si), Selenium (Se) or Cadmium Telluride (CdTe), responsible of the X-ray photon conversion in electrical signal. The principle of the direct conversion is illustrated in Fig. 1.2.

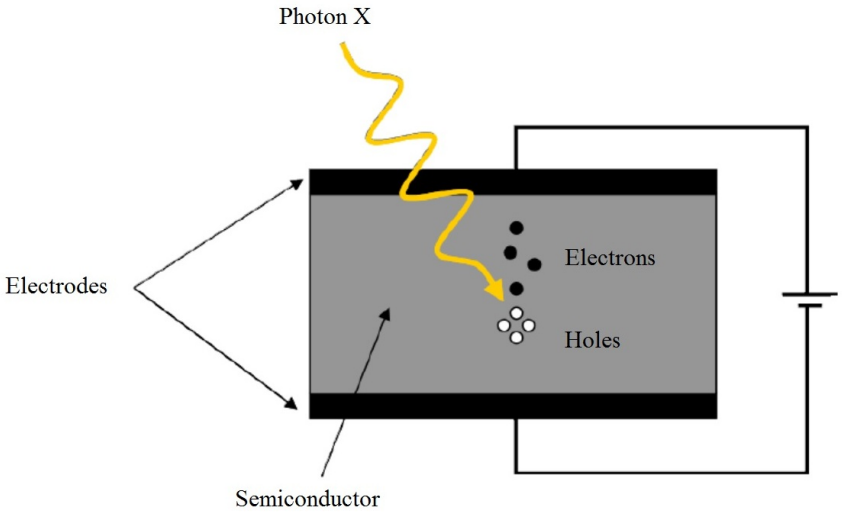

Figure 1.2: Scheme of the principle of direct conversion detector.

The semiconductor detector is composed by two electrode, one called *cathode* and the second one called *anode*. Once the photon interacts inside the semiconductor material, a quantity of charges proportional to the energy released by the interaction is produced. These charges (electrons and holes) migrate under the effect of the electric field in the direction of the electrode with opposite polarity (anode and cathode, respectively). The direct conversion provides a better energy resolution and a better efficiency between the received photon and the measured electrical signal. In this way a better signal to noise ratio (SNR) is obtained. When a direct conversion system produces ∼10000 charges, an indirect conversion one produces only 1000 [25]. In this category we can find flat panel detectors mainly used in mammographies [26], CdTe (or CdZnTe) for γ cameras [27] and Si, GaAs and CdTe as photon counting detectors [28],[29].

In both cases the detector can works in *Integration mode* and provide a signal proportional to the total energy deposited in the conversion layer. Another category of detector operates in *Counting mode*, in which individual X-rays are detected. Finally, *Spectrometric mode* detectors are capable to detect each single X-ray and measure its energy.

1.1.1 Detection modes

The detector presented above can operate in different detection modes, Integration, Counting or Spectrometric, according to the application in which they are involved. In this Section an overview of these detection modes it is presented.

In *Integration mode* the current from the detector is integrated during all the acquisition time, as shown in Fig. 1.3.

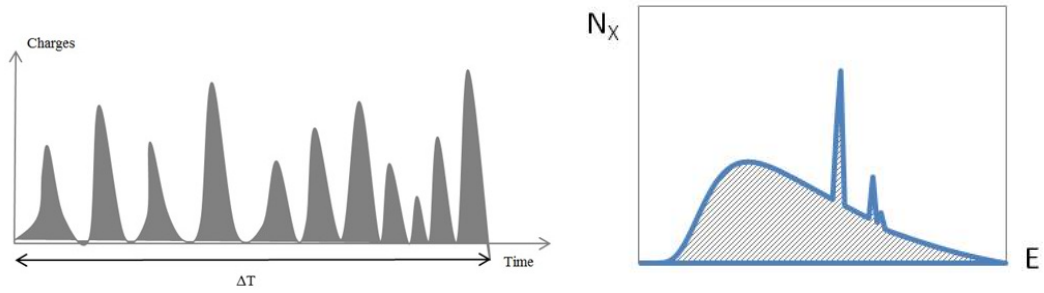

Figure 1.3: (Left) Measured signals with an integration mode detector. All pulses during the time ΔT are integrated. (Right) Corresponding X-ray spectrum obtained in Integration mode.

The signal is proportional to the energy deposited in the detector during the acquisition time window, ΔT:

$$N_{integration} = \int_{E_{min}}^{E_{max}} N(E) \cdot E \cdot dE \tag{1.1}$$

where E_{max} is the maximum energy of the spectrum and N(E) is the number of incident photons with the energy "E".

In *Counting mode* the individual X-rays are detected. The operation requires a certain number of energy thresholds. The Timepix chip [36] has a single energy threshold. The threshold can be adjusted for each pixel in order to obtain uniform performances of the whole pixel matrix. In this operation mode it is possible to use more than 1 energy threshold in order to obtain information on more energy channels.

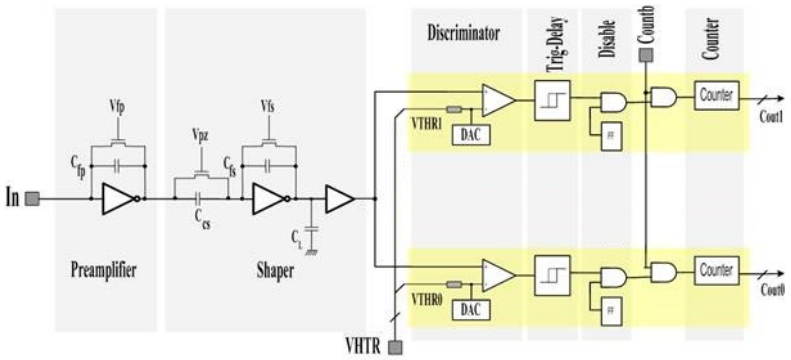

Figure 1.4: Schematic block of one pixel working in counting mode with two energy thresholds [2].

Fig. 1.4 represents a standard architecture for a counting mode detection with two energy thresholds but the concept can be easily extended to a bigger number of thresholds and counters. In the diagram we can notice the presence of a first block, i.e. a Charge Sensitive Amplifier (CSA). Thereafter, the shaped signal is compared to two threshold for the selection of the energies. Finally, it is necessary to store inside one or more memories the information about the number of energies detected. In the literature, the number of these memories, and consequently, the energies detected, is limited (up to 8) ([12],[30]). Fig. 1.5 represents the measured pulses identified by two energy thresholds and the corresponding bi-energy spectrum.

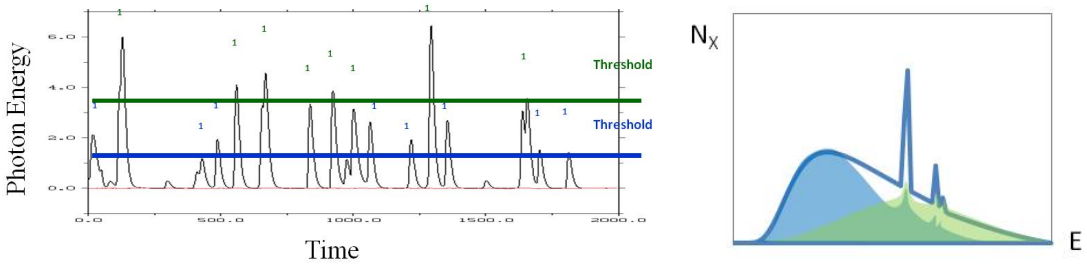

Figure 1.5: Measured pulses from counting bi-energy mode (on the left) and the corresponding X-ray spectrum (on the right). [31]

Spectrometric detectors have the great ability to sort the photons in different channels according to their energy. Spectrometric X-ray detectors can give way to energy-resolved X-ray imaging for all current modalities (e.g. radiography, CT ...). The resulting image quality advantages are substantial [33]. An example of electronic circuit able to reproduce a spectroscopic acquisition mode with several number of channels (up to 256), is represented in the Fig. 1.6.

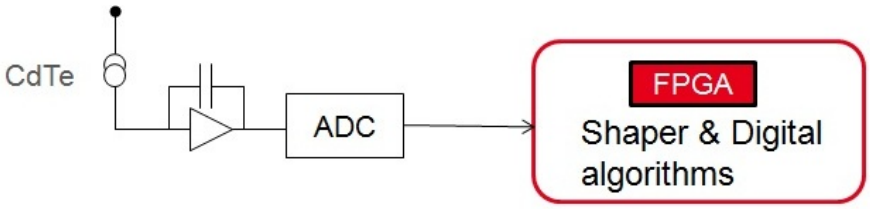

Figure 1.6: Schematic block of one pixel working in multi-energy mode.

For these detectors the signals from the CSA are directly digitized and processed by an FPGA. In the FPGA we can find processing algorithms such as the shaping circuit, the correction algorithm for the charge sharing and pile-up and the processing for the reconstruction of the energy spectra. Fig. 1.7 represents the measured pulses identified by their energy and the corresponding multi-energy spectrum. Each energy detected is represented in the spectrum with different colors.

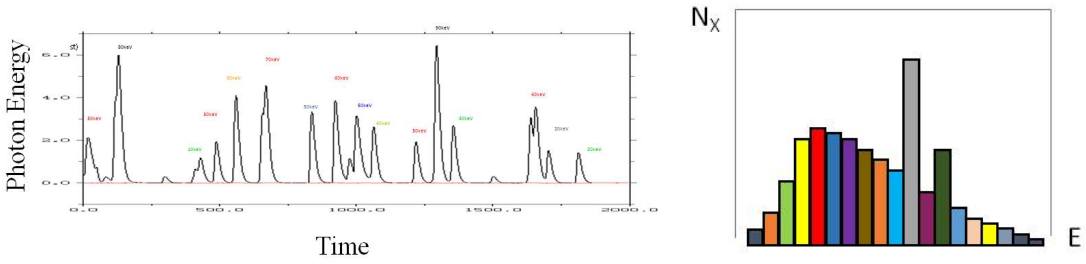

Figure 1.7: Measured pulses from multi-energy mode (on the left) and the corresponding X-ray spectrum (on the right).

1.2 Energy resolved imaging

The progresses in the domain of the materials and electronics have allowed to develop detectors able to work in counting mode. This type of detector are called Photon Counting Detector (PCD). Their ability is to count the number of photons with the energy above a fixed threshold. An example of PCD is the detector XPAD which can be hybridized with different semi-conductors [34] with one threshold, or MEDIPIX with 8 thresholds [35]. From now on, there are types of detector able to classify photons according to the value of their energy. These spectrometric detectors are subject to some constraints due to the material and to the electronics.

1.2.1 Material for the MEPCD

Many materials were studied for the X-ray detectors for which their properties were compatible with the use of Multi-Energy Photon Counting Detector (MEPCD). Among these material we can find mono-crystalline Silicon (Si), Germanium (Ge), Cadmium Tellurium (CdTe), Thallium Bromide (TlBr) or Mercury Iodide (HgI_2). Mono-crystalline Silicon is one of the most used material. The use of this material is limited to the detection of low energy photons (0 - 20 keV) because of its low Z and density (Z=14 and ρ = 2,33 g $\cdot cm^{-3}$). The main field of application of the Silicon detectors is for X-Ray Fluorescence (XRF) analysis. For high resolution spectrometry, Germanium detectors are the most suitable but they have to be cooled to low temperatures.

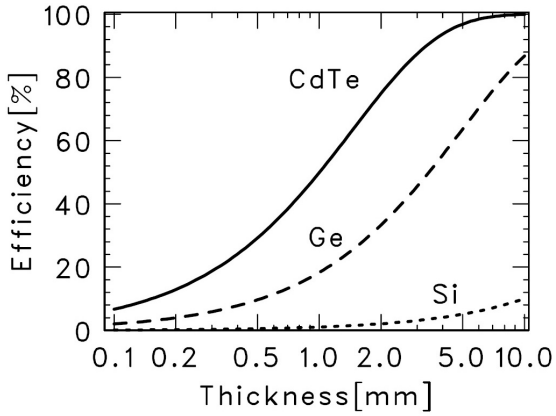

Figure 1.8: Detection efficiency for 100 keV X-ray photon in various thickness of CdTe, Si and Ge [1].

The CdTe and CdZnTe offer an higher stopping power (Z=48/52 and ρ = 6,2 g $\cdot$cm^{-3}). Moreover, as for the Silicon, it is possible to use them at room temperature (band gap $\sim$ 1,2 eV). Fig. 1.8 illustrates the efficiency of such detector material compared to the Si and Ge.

An alternative to the CdTe is the Gallium Arsenide (GaAs, Z=31/33 and ρ = 5,3 g $\cdot$cm^{-3}), mainly used in the energy range of 10-30 keV. So, for the energy range used for radiography or security applications (20 - 150 keV) these detector are not good. Finally, the TlBr and HgI_2 are equally studied for their use in X-ray detectors and they are potentially interesting for the good transport properties and good stopping power. Unfortunately, they are not commercially available. Moreover, they are not provided by the same technological maturity of CdTe, Si, Ge or GaAs.

Semiconductor	ρ (g/cm^3)	Z	E_{gap} (eV)	ϵ (eV)
Si	2,33	14	1,12	3,6
Ge	5,33	32	0,67	2,9
CdTe	5,85	48-52	1,44	4,43
CdZnTe	5,81	48-52	1,6	4,6
HgI	6,4	80-53	2,13	4,2

Table 1.1: Properties of the semiconductors discussed. E_{gap} is the band gap energy, ϵ is the ionization potential, Z is the atomic number and ρ the material density [1].

Tab. 1.1 shows the physical characteristics of the elemental and compound semiconductors. Among the range of semiconductor detectors available for X-ray detection, CdTe (and CdZnTe) have a privileged position because of their high density and the high atomic number of their components, as well as a wide band-gap.

It is now clear that the proprieties of the CdTe and CdZnTe are the most suitable for the multi-energy photon counting detectors in the energy range of 20 - 160 keV. Imaging systems utilizing CdTe or CdZnTe (CZT) detectors have great potential to replace currently used imaging systems composed of scintillating materials, such as, NaI(Tl) and CsI(Tl), coupled to either photomultiplier tubes (PMTs) or photo-diodes. However, the main advantage of CdTe and CdZnTe detectors over scintillator detectors is their superior energy resolution at room temperature.

1.2.2 Hybrid Photon Counting Detectors

Numerous researchers are interested in the development of new systems including X-ray PCD semiconductor detectors. This research subject is still active and many prototypes, according to the specific goal, were developed. Fig. 1.9 shows and compares some ASICS for spectral computed tomography (CT). The state of the art will be presented focusing the attention on particular goals, such as the dealing with high fluxes or the number of channels used.

Name	Matrix	Pixel side (μm)	Energy thresholds	Peaking time (ns)	Maximum count rates (Mcps/pixel)	Maximum count rates (Mcps/mm²)	Electronics Noise or energy resolution	Power per channel (μW)	CMOS node
Medipix3 (FPM-SPM)[1]	256x256	55	2	120	2.5	826.5	1.37keV FWHM @ 10KeV	7.5	0.13μm
Medipix3 (FPM-CSM)[2]	256x256	55	1+1	120	5.0E-01	163.5	2.03keV FWHM @10KeV	9.3	0.13μm
Timepix3 (CERN)[3]	256x256	55	10bits	30	1.6E-03	0.53	4.07kev FWHM at 59.5keV	15.2	0.13μm
Pixirad Pixie II[4]	512x476	55.6	2	300	5.0E-01	161.5	1.45keV FWHM @ 20keV	12.5	0.18μm
Samsung PC[5]	128x128	60	3	NS	NS	NS	68 e- r.m.s.	4.6	0.13μm
Pixirad Pixie III[6]	512x402	62	2	125	1.0	260.1	6.6% FWHM @ 60keV	34	0.16μm
Eiger[7]	256x256	75	1	30	4.2	711.1	121e- r.m.s. (low noise settings)	8.8	0.25μm
PXD23K (AGH)[8]	128x184	75	2	48	8.5	1519.5	89e- r.m.s.	25	0.13μm
X-Counter PC (PDT25-DE)[9]	256x256	100	2	NS	1.2	120	8.3keV FWHM @20keV 10keV FWHM @60keV	NS	NS
PXD18K (AGH)[8]	96x192	100	2	30	5.8	580	168e- r.m.s.	23	0.18μm
FPDR90 (AGH)[8]	40x32	100	2	28	8.5	854.7	106e- r.m.s.	42	90nm
AGH_Fermilab[10]	18x24	100	2	48	NS	NS	84e⁻ (Single pixel), 168e⁻ (Charge summing)	34	40nm
Medipix3 (SM-SPM)[11]	128x128	110	8	120	4.5	375.7	1.43keV FWHM @ 10keV	30	0.13μm
Medipix3 (SM-CSM)[12]	128x128	110	4+4	120	3.4E-01	28.1	2.2keV FWHM @10keV	37.2	0.13μm
XPAD3[13]	80x120	130	2	150	2.0	118.3	127e- r.m.s.	40	0.25μm
Pilatus 2[14]	60x97	172	1	110	6.0	202.8	1keV FWHM @ 8keV	20.2	0.25μm
Pilatus 3[15]	60x97	172	1	110	15.0	507.0	1keV FWHM @ 8keV	20.2	0.25μm
Telesystems [16]	40x40	200	4	300-500	8.0E-01	20	5.36keV FWHM @ 122keV	94.4	0.25μm
Dosepix (CERN)[17]	16x16	220	16	287	1.6	33.9	150 e- r.m.s.	14.6	0.13μm
Siemens PC[18]	64x64	225	2	20	40.0	790.1	NS	NS	NS
Hexitec[19]	80x80	250	14bits	2000	1.0E-03	0.016	800eV FWHM @ 60keV, 1.1keV @ 141keV	220	0.35μm
Philips Chromaix [20]	4x16	300	4	20	38.0	422.2	4.7keV @60keV (1 channel)	3000	0.18μm
Ajat-0.35 (PC)[21]	32x64	350	1	1000	2.2	18.0	4keV FWHM @122keV	390.6	0.35μm
Ajat-0.35 (ADC)[22]	32x64	350	64	1000	4.9E-05	4.0E-04	4keV FWHM @122keV	390.6	0.35μm
CIX 0.2 (Bonn)[23]	8x8	353.6	1	NS	12.0	96	330e- r.m.s. (counting channel)	3200	0.35μm
KTH_Lin_SPD [24]	160 ch.	447.2	8	10-20-40	272.0	1360	1.09keV @ 15keV (measured at 40kcps)	80000	0.18μm
DxRay-Interon[25]	16x16	500	4	10	13.3	53	7keV FWHM @60keV, Min TH20keV	NS	NS
Ajat-0.5[26]	44x22	500	2	1000-2000	NS	NS	4.7keV @122keV (1 channel)	413.2	0.35μm
Hamamatsu[27]	64 ch.	632.5	5	NS	5.5	13.75	12keV FWHM @ 120keV	NS	NS
IDEAS[28]	64 ch.	894.4	6	50	4.0	5	7keV FWHM @60keV	4200	0.35μm
GE-DxRay [29]	128 ch.	1000	2	30	11.6	11.6	4.75% at 122keV, CZT, 5pF Cin (1 Channel noise= 4.8keV FWHM)	2100	0.25μm
BNL [30]	64 ch.	1241.0	5	40-80-160-320	4.0	5.5	5.5keV at 40ns peaking time/2.15keV at 320ns peaking time	4700	0.25μm

Figure 1.9: Review of ASICS for spectral CT. From the workshop on "Medical Applications of Spectroscopic X-ray detectors", CERN, 20-23 April 2015. [37]

Each detector here presented is coupled to a readout circuit working in counting mode with the use of one ore more energy thresholds. They are conceived for different and specific applications and thus optimized according to their use. Some of them were optimized in the number of channels used, other for the count rate achievable and others were optimized changing the geometry of the detector itself in order to get better spatial resolution.

MEDIPIX

One of the most famous family presented in the table is the MEDIPIX one. It is a family of photon counting and particle tracking pixel detectors developed by an international collaboration, hosted by CERN. The fist chip consisted in a matrix of 64x64 pixels of 170 μm size [29]. Fig. 1.10 represents the principle of the phonon counting in a single pixel, adopted for the fist generation of MEDIPIX. The radiation generates electron-hole pairs (charge) in the sensor. The charge is collected by the appropriate pixel, amplified and compared with an energy threshold. The counter is then increased if the detected pulse is above the energy level.

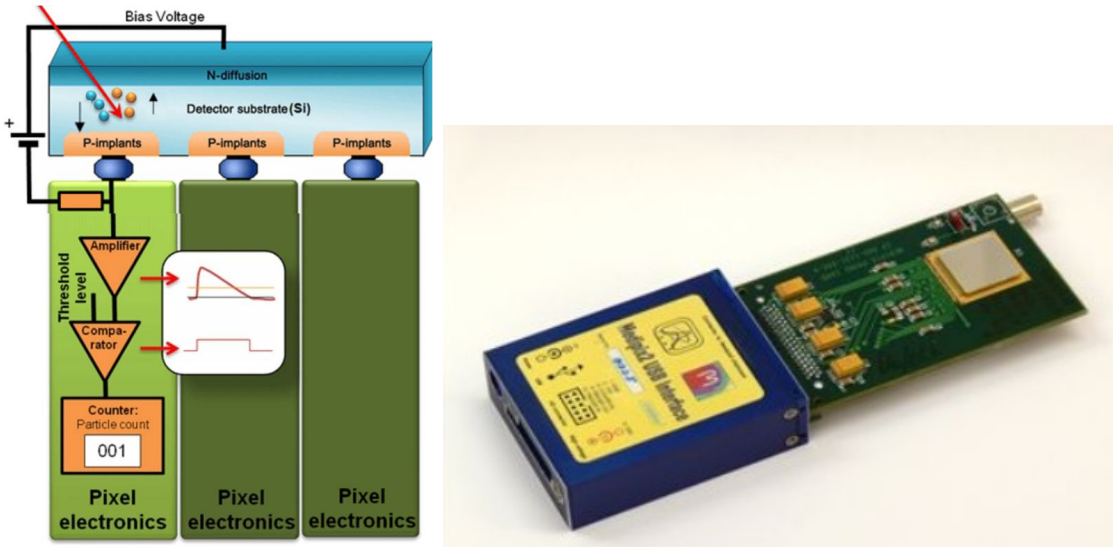

Figure 1.10: (Left) Principle of the photon counting in a single pixel.(Right) Standard, single chip MEDIPIX carrier board with USB readout.

The next generation, MEDIPIX-2, has a readout electronics consisting of an array of 256x256 readout channels with a size of 55 μm. The number of energy threshold was increase in this version and it was used in many scientific experiments. Other projects which aim to add new functionality or increase chip performances, have been developed. The great novelty in MEDIPIX-3, is the correction of charge sharing events with the technique of clustering the pixels [38]. This technique will

be explained in detail when the phenomenon of charge sharing will be presented in the next Section.

Xpad

Another family using one single threshold is the XPAD. This family has been developed in France for synchrotron applications, where mono-energetic beams are involved. Therefore one single energy threshold is used. The latest XPAD-3 version has been realized in 0,25 μm IBM technology with the pixel matrix of 80x120 elements of single pixel size of 130μm x 130μm. The chip presents two versions, one called XPAD3-S (S = Si), working with charge generated by photons in the energy range from 4 keV to 40 keV. The other version is the XPAD3-C (C = CdTe), working with charge generated by photons in the energy range from 6 keV to 60 keV. [34]

PCD for high count rate applications

Another important aspect to take into account for X-ray imaging is the output count rate achievable for dealing with high flux applications. In Tab. 1.9 we can find some examples of devices characterized by a maximum count rate per pixel higher than others (DX-Ray[39], ChromaAIX [40], Siemens [41]). These devices are characterized by a relatively short peaking time. The peaking time is the time required for a pulse shaped by processing electronics to reach its maximum amplitude. In order to reduce the pile-up, it is necessary to use a short peaking time. This approach is often cause of energy resolution degradation because of the phenomenon of the ballistic deficit.

1.2.3 Spectrometric Detectors

CEA-LETI has developed a readout circuit able to measure high resolution spectra with 256 energy bins. The prototype works in the energy range of 20 - 160 keV and and ADC continuously digitizes the signals at 100 MHz on 10 bit. An FPGA is responsible of performing signal processing in real-time. Fig. 1.11 represents a diagram of the readout electronic developed in CEA-LETI. The proposed architecture, which includes one ADC per pixel, is feasible for a linear pixel detector array but it can be easily extended to larger sensors. Such sensors can replace standard dual layer sandwich detectors used for explosive detection in luggage inspection, providing much more complete energy information on the X-ray transmission function of inspected materials [9].

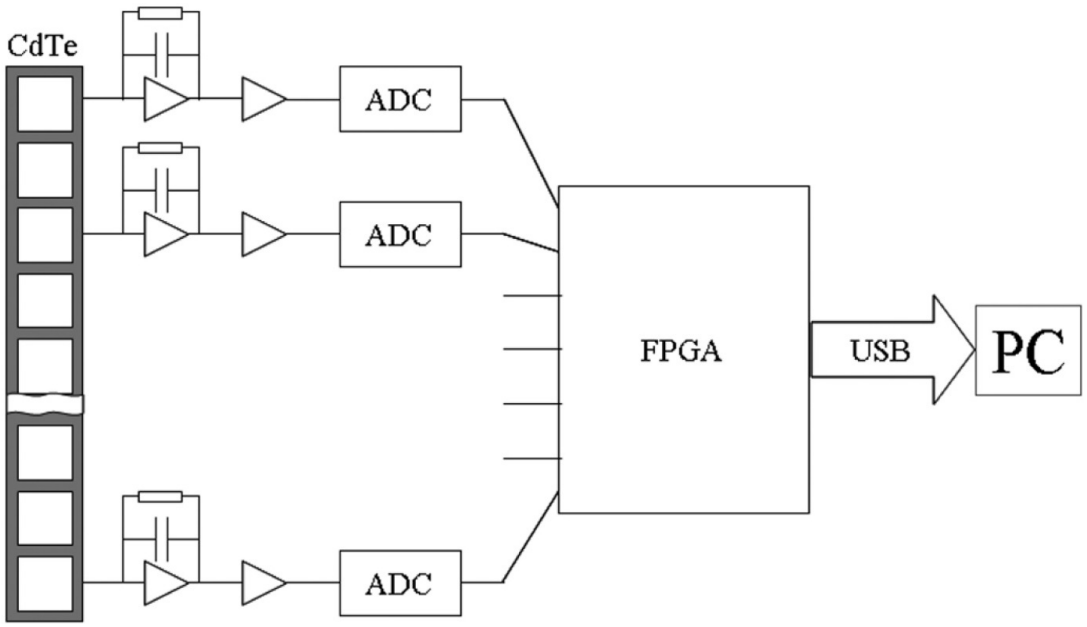

Figure 1.11: Diagram of the architecture developed at CEA-LETI [9].

This concept was transferred to MULTIX company (2010), which has developed a commercial detector module, called ME100, based on this architecture.

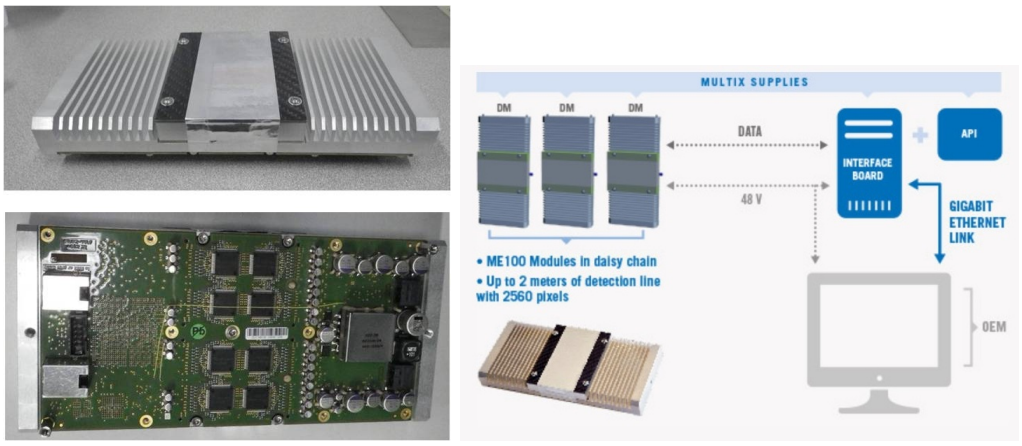

Figure 1.12: (Left)Up view (top) and down view (bottom) of the device.(Right) Modular architecture built up from separate detection modules (DM) of ME100 device [42].

ME100 is a multi-energy detector able to measure the correct energy of an interacting photon X at high rate ([43], [44], [45]). Thanks to the counting system working in real-time, ME100 is able to reconstruct the energy spectra in the energy range of 20 - 160 keV. The detector module is a CdTe composed by 4 linear array of 32 pixels, for a total or 128 pixels of 800 μm size. Fig. 1.12 (on the right side) represents a possible modular architecture built up from single separate modules of the ME100 device (Fig. 1.12 on the left side). We can summarize its outstanding

main performances in a saturation level at 7 Mc/s/pixel and an energy resolution equal to 5,8 keV at 60 keV.

A similar approach is presented in [46]. Here are underlined the performances of a pixellated CdTe (4x4) coupled to a custom digital readout electronic for high flux measurements. The detector in use is based on an array of 16 pixel with a size of 600 μm. The readout electronics is able to continuously digitize and process the signal from each pixel even at high fluxes. The work describes the spectroscopic results and the high flexibility of the digital readout electronics. The system is able to provide good energy resolution at low (test at 200 c/s) and high count rate (test at 1,1 Mc/s) by using a novel Digital Pulse Processing (DPP) characterized by two shaping circuits, one fast mainly responsible of the pile-up rejection and one slow totally responsible of the pulse shape and height analysis for the reconstruction of energy spectra at very high resolution.

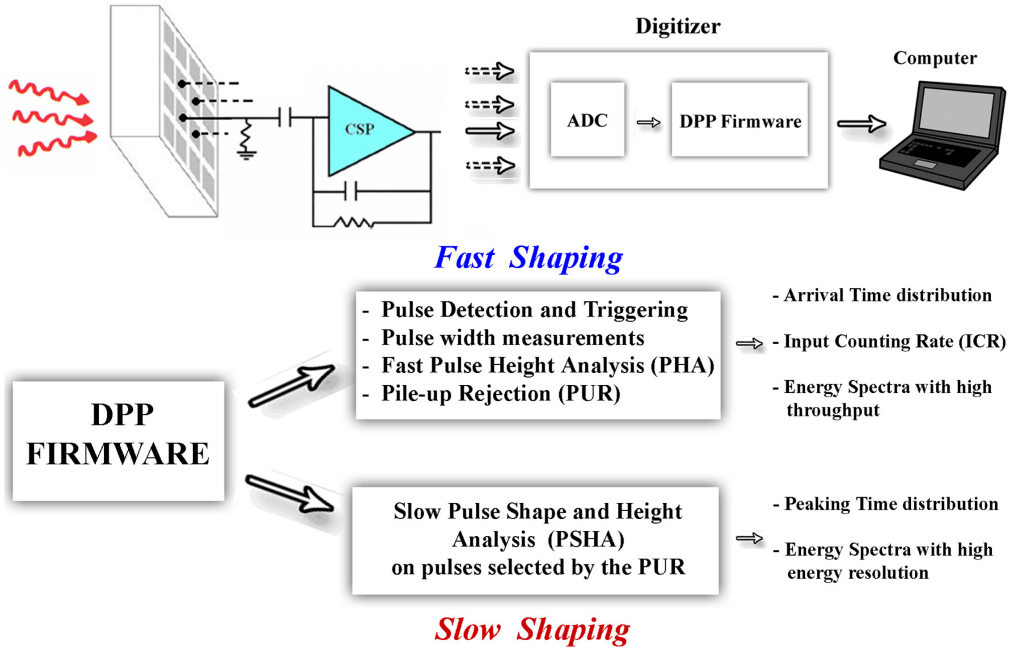

Figure 1.13: A schematic view of the readout electronic circuit architecture and the main operations of the DPP firmware in [46].

Fig. 1.13 represents a diagram of the processing described in [46] and the main operation of the DPP firmware. The readout electronics described here opens up to many X-ray imaging applications which need different throughput and energy resolution conditions.

In the previous examples, the circuit architecture with a fast ADC is adapted for linear detector (1D). In order to work with a 2D matrix detector, a new architec-

ture for spectral imaging inside the pixel is presented in [47]. The different operations performed by the FPGA are now developed inside the pixel by a front-end analog circuit. Each pixel has an ADC able to record the amplitude of the pulses processed by the analog front end circuit. The pixel architecture has been measured at 8 Mcps/pixel while embedding on-chip spectral cleaning corrections, such as charge sharing, weighting potential cross-talk and pile-up. The improvements compared to antecedent works dated from 2008 until 2012 are significant. Even if the number of pixel of the prototype is limited compared to other works, the step forward done in the number of bin used for the spectra reconstruction is significant. Moreover, the correction of the undesirable effect inside the pixel maintaining a maximum output count rate at 8 Mcps/pixel represents a big evolution in spectroscopic detectors. Fig. 1.14 represents the pixel layout of the designed chip.

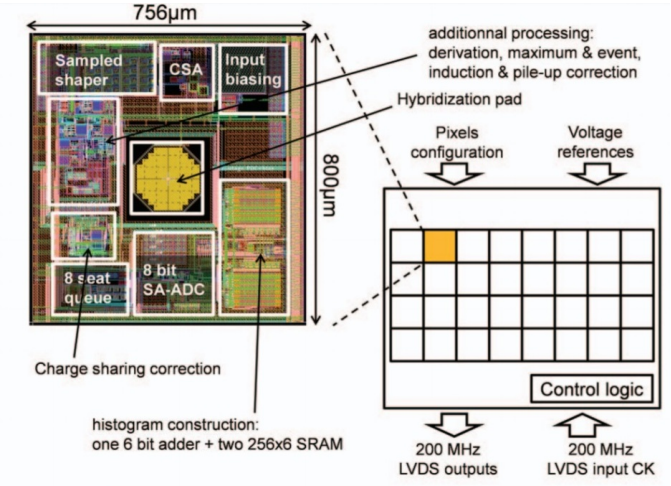

Figure 1.14: Pixel layout and overall diagram of the designed chip. [47]

1.3 Physics of pixel detectors

The aim of this Section is to present the signal induction in semiconductor pixel detectors and the effect that pixelization and high fluxes have on the detector response.

1.3.1 Induced signal in semiconductor detectors

When a charge moves between two electrodes, a charge proportional to the distance travelled is induced on the surface of them. Fig. 1.15 represents a parallel electrodes detector (a) and a pixel one (b) where a voltage V is applied. In the case of a planar detector, the induced charge on the collecting electrode is:

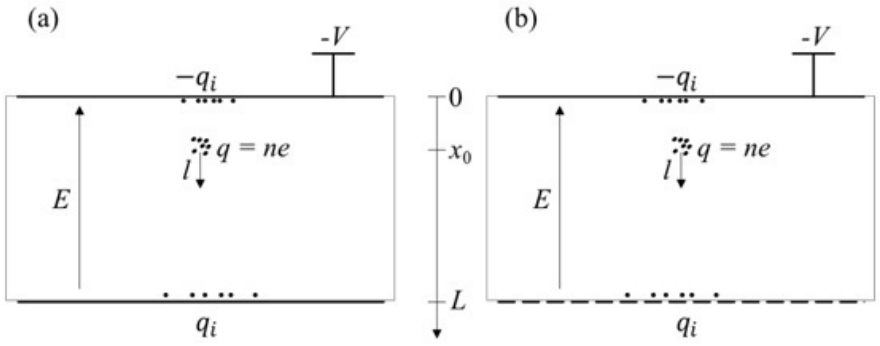

Figure 1.15: Induced charge on a planar detector (a) and on a pixel one (b).

$$i(t) = n \cdot e \cdot \frac{v}{L} \tag{1.2}$$

Where n is the number of charges in the charge cloud, e is the elementary charge, v the charge velocity and L is the distance between the cathode and the anode. The total charge induced on the electrode by the electron cloud generated in a point x_0 in the detector volume is the integral of Eq. 1.2:

$$q = \int_{t=0}^{\frac{L-x_0}{v}} \frac{n \cdot e}{L} \cdot \frac{dx}{dt} \cdot dt = n \cdot e \cdot \frac{L - x_0}{L} \tag{1.3}$$

The induced charge is proportional to the number of deposited charge and to the distance travelled by the charges.

When a pixel detector is used, the charge induce by the drift of the electrons is shared among several pixels. The total charge is then equivalent to the one in Eq. 1.3 but only a fraction of it is induced on the collecting pixel. The rest of the charge is actually shared among the neighbouring pixels. Shockley and Ramo have shown that the transient signal on the electrode is computed from a *weighting field* [48], [49], [50]:

$$i(t) = n \cdot e\overrightarrow{E_w} \cdot \overrightarrow{v(t)} \tag{1.4}$$

Where $\overrightarrow{E_w} = -\overrightarrow{\nabla}(V_w)$ is the *weighting field* and V_w is called *weighting potential*. V_w is a virtual potential obtained by setting the potential of the considered electrode to 1 and setting all the others to 0. From Eq. 1.4 it is possible to calculate the induced charge, as follow:

$$Q_{induced}(t) = \int i \cdot dt = n \cdot e \int \overrightarrow{E_w} \cdot d\overrightarrow{x} = n \cdot e \cdot \{V_w[x(t)] - V_w[x(t=0)]\} \tag{1.5}$$

Fig. 1.16 represents the weighting potential measured at the center of a collecting pixel and at the center of its neighbouring one. As a comparison, the weighting field for a planar detector is represented.

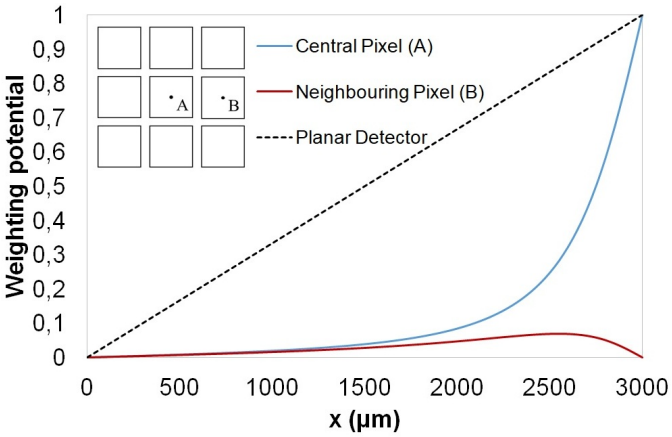

Figure 1.16: Weighting potential measured at the center of the collecting pixel (blue) and at the center of the neighbouring pixel (red) for a 3 mm thickness and 800 μm pitch pixel.

From Fig. 1.16 it is possible to notice that the signal is weak in the first mm of the pixel thickness. When the electron cloud is around 1 mm far from the electrode the charge increase significantly.

Eq. 1.5 shows that the charge induced in pixel detectors is proportional to the shape of the weighing potential. The consequence of this result is that if the pixel size is smaller compared to the detector thickness, the *small pixel effect* occurs. Compared to a planar detector, the dependence of the weighting potential on the depth interaction is no more linear.

1.3.2 Weighting potential cross-talk

An important consequence of the small pixel effect is the induction of a transient signal on the neighbouring pixel. We call this effect *weighting potential cross-talk* [90]. Fig. 1.16, which represents the weighting potential cross-talk calculated on the neighbouring pixel, shows that a small transient signal is induced. As long as the charges are far from the pixel, we observe a small positive current. When the electrons reach the collecting pixel, a negative current is induce on the neighbouring pixel. A typical example of pulses induced by weighting potential cross-talk is presented in Fig. 1.17, showing the signal from two adjacent pixels [52]. The large pulse corresponds to the pixel where the X-ray photon is absorbed and the generated charge is collected. A smaller bipolar pulse is observed in the neighbouring pixel

induced by the phenomenon. In the pixel no charges are collected, because the shaping circuit acts such as the integral of the signal is equal to zero. In certain cases its amplitude can be large enough to be detected and confused by a low-energy photon. We will see in Chapter 2 that it is possible to reject pulses induced by weighting potential cross-talk with a dedicated pulse processing [52].

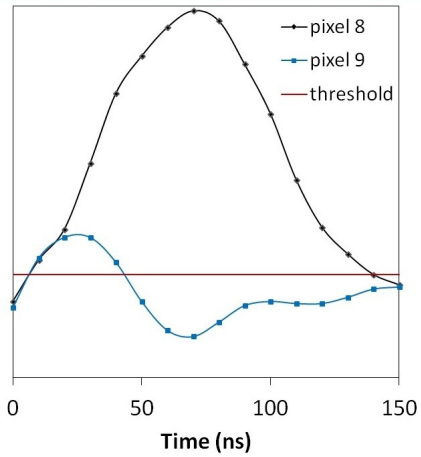

Figure 1.17: Overlap of pulses on neighbouring pixels induced by weighting potential cross-talk [52].

1.3.3 Charge sharing

The weighting potential cross-talk is responsible for the lower part of the pulse-height spectra where there is a large number of pulses with an amplitude slightly above the detection threshold. However, other type of undesirable effect have been observed. Fig. 1.18 represents the spectra measured by a prototype 16 pixel linear (1D) spectrometric CdTe detector using a radioactive source of ^{57}Co.

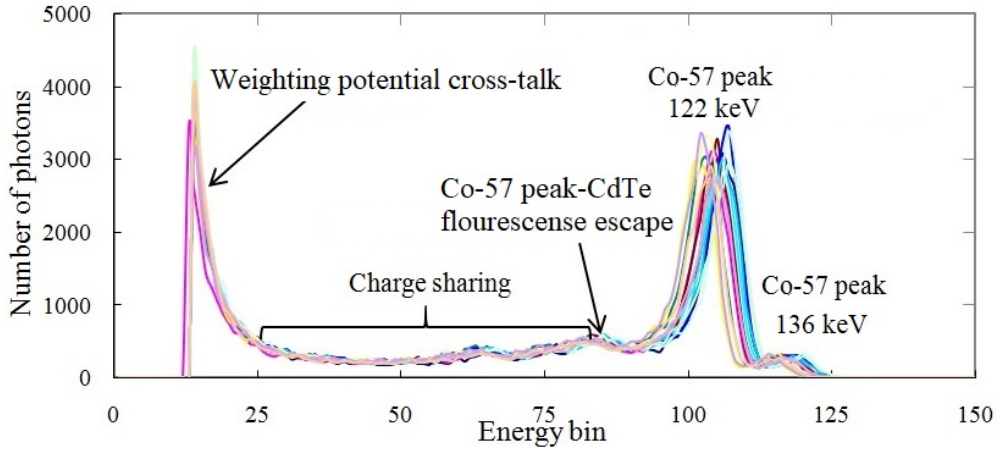

Figure 1.18: Spectral response measurements for 16 different pixels (various colors) of a spectrometric detector. Channel width is equal to 1,2 keV. [53]

Ideally one would expect a single peak around the energies 122 keV and 136 keV. However, the low energy tail of the pulse height spectra is mainly due to charge loss, *charge sharing* and *weighting potential cross-talk*. Many physical phenomena can lead to amplitude loss, such as Compton scattering, K-shell fluorescence, as well as thermal diffusion of the photo-generated charge carriers. [53]

Charge sharing is the result of the spread of the charge cloud generated from a single X-ray photon. The charges are collected by two adjacent pixels (Fig. 1.19). An example of pulses affected by charge sharing is shown too.

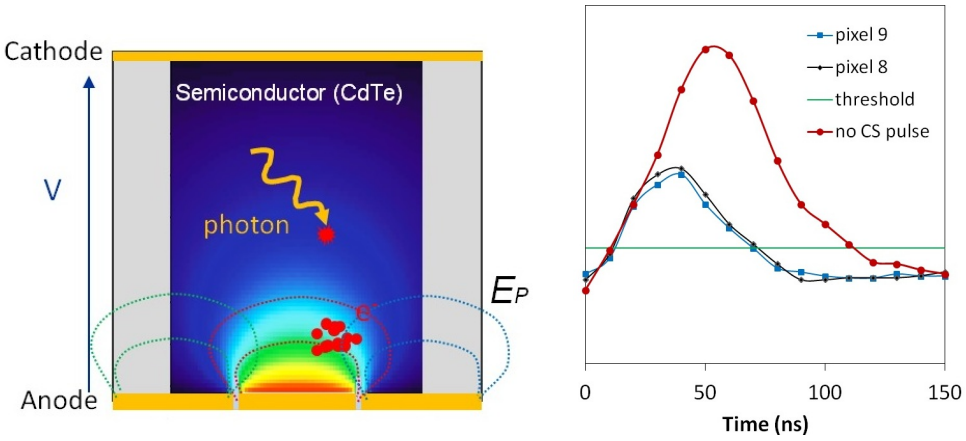

Figure 1.19: (Left) Simulation of the charge cloud shared by two neighbouring pixels causing the phenomenon of the charge sharing. (Right) Overlap of pulses on neighbouring pixels induced by charge sharing [52]. In red the pulse not affected by charge sharing.

In this example, we observe that the sum of the amplitudes of two pulses detected on neighbouring pixels is equal to that of a normal pulse without charge sharing. If all the charges are properly collected by the two neighbouring pixels, the correct incident photon energy is obtained by summing the amplitude of the two pulses on adjacent pixels.

1.3.4 Pile-up

Another source of error due to the rate of events per second is the *pile-up* effect. Pile-up happens when pulses arrive in a temporal window shorter than the resolution time of the system. Fig. 1.20 represents a simulation of the detector output where we can distinguish the data from the detector itself with each component of the train of pulse pile-up.

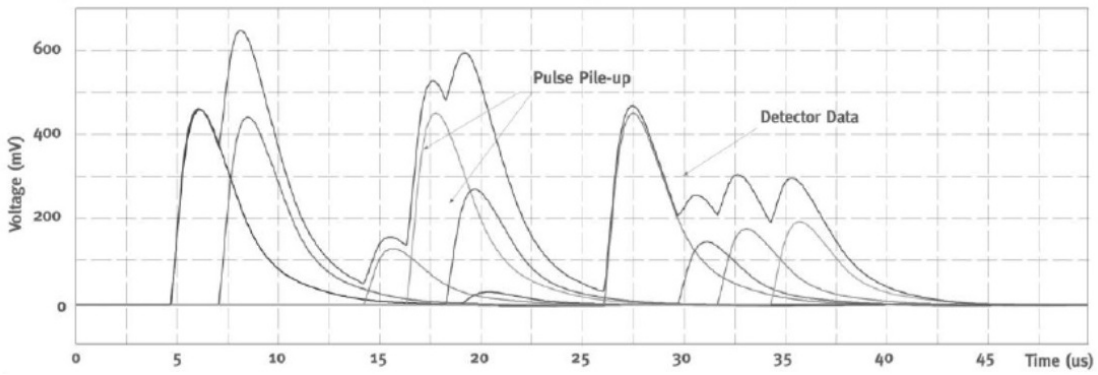

Figure 1.20: Example of pulse pile-up.

With count rates as high as those required for CT and XR medical imaging, two types of pulse pile-up effects are observed: *peak pile-up* and *tail pile-up*. Coincidences during the initial part of a pulse are recorded as a single count at a higher energy than the original pulse's energies. This is called peak pile-up. The long tail of the pulse affects the recorded energy of subsequent events. A peak overlapping the tail of a preceding pulse, results in a higher recorder energy. This is called tail pile-up. Both peak and tail pile-up distort the recorded spectrum, and the amount of distortion depends strongly on the count rate. The impact that pile-up has on a measured spectrum is represented in Fig. 1.21.

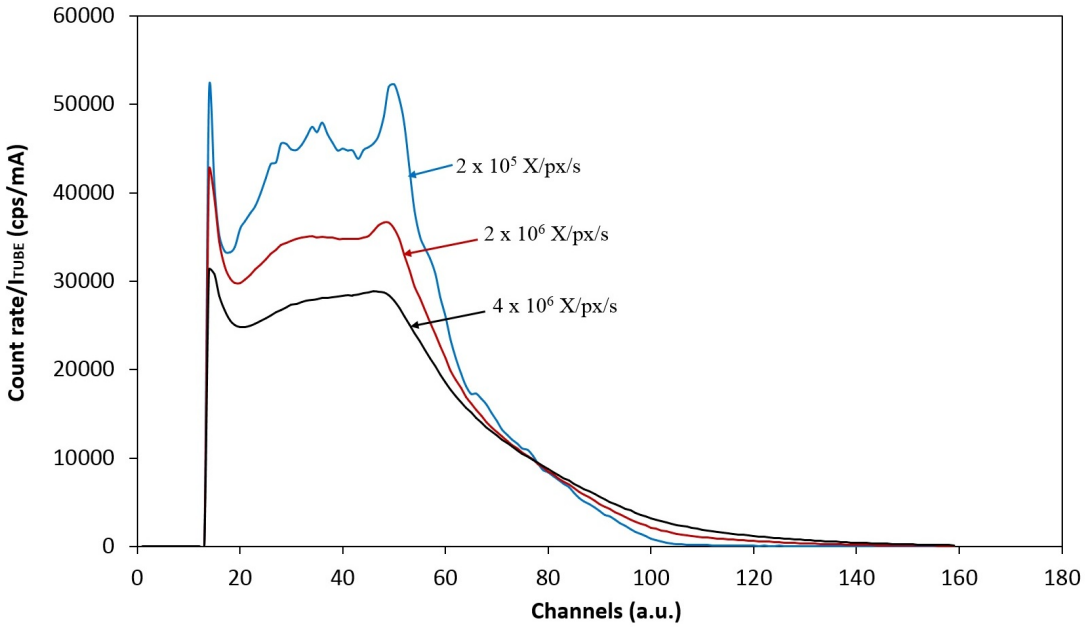

Figure 1.21: Examples of measured X-ray spectra at 3 different count rates, normalized by the tube current. [53]

The spectra are measured by a prototype spectrometric CdTe detector developed at CEA-LETI Detector laboratory (LDET) using an X-ray source at 120 kV with

different currents of the tube in order to obtain different count rates [9]. In absence of pile-up, the three spectra normalized by the tube current should be identical. When the pile-up rate increases we notice a decreasing on the number of output count rate with an increasing on the number of photons in high energy range. This is due to the peak pile-up. Moreover, we can notice a distortion of the pulse height spectra caused by the tail pile-up, responsible of the energy resolution degradation, that can be observed on the fluorescence peak of Tungsten (W), around the channel 55.

1.3.5 Ballistic deficit

Semiconductor detectors converts the deposed energy from the absorbed interaction in electrical signals. The interaction creates free charges (electrons or holes) collected by the electrode under the effect of an electrical field. The drift of these charges induces an electrical current on the electrode that is converted in voltage signal by the CSA. The voltage pulse is then processed by a shaping circuit with the goal of shorten the temporal width of the signal and increase the SNR. We call *peaking time*, T_p, the duration between the beginning and the maximum of the pulse.

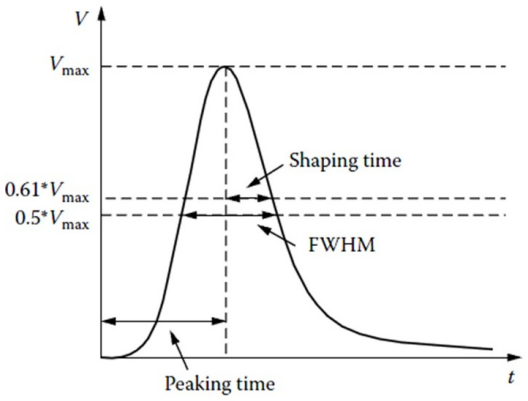

Figure 1.22: An illustration of the definition of peaking time of an output pulse from a shaping circuit.

Fig. 1.22 represents the definition of T_p. In an ideal case T_p is large compare to the charge collecting time, in order to measure all the signal. In the opposite case, a fraction of charge will not be collected. This phenomenon is calle *ballistic deficit*. This effect can have an important impact impact on the energy resolution of the system. Fig. 1.23 shows an illustration of the ballistic deficit.

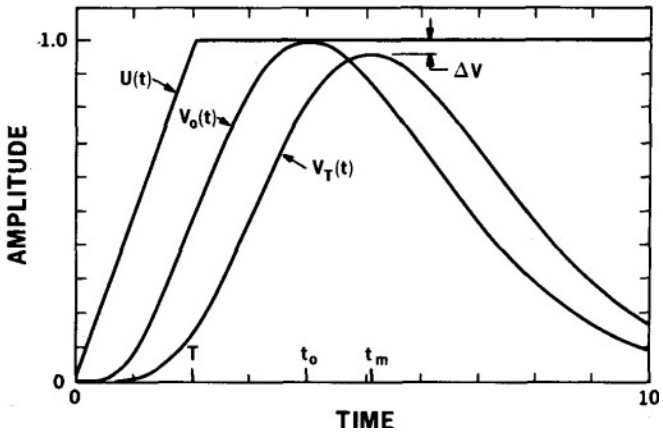

Figure 1.23: An illustration of the ballistic deficit. [20]

For a given pulse shaper (Gaussian filter in Fig. 1.23), there is an impulse response output function $V_0(t)$ when all the charges are collected instantly. If the charge collection time is finite, the input function, U(t), will reach its maximum at a time T, and the output $V_T(t)$ will reach its peak amplitude at t_m. This maximum amplitude is generally less than the one of the impulse response function. The ballistic deficit (BD) is therefore defined as:

$$BD = \Delta V = V_0(t_0) - V_T(t_m) \tag{1.6}$$

1.4 Correction techniques

In this Section the state of the art of the existing techniques for the phenomena of charge sharing, pile-up and ballistic deficit will be presented.

1.4.1 Charge sharing correction

Here we are going to present the state of the art corresponding to the phenomenon of charge sharing in pixel detectors of different thickness and pitches. Normally, the detection of charge sharing events is performed through a Time Coincidence Analysis (TCA), by detecting the events of adjacent pixels in temporal coincidence within a selected Time Coincidence Window (TCW). After the detection of these events the signal processing is responsible of treat them in order to recover or reject the amplitude information. The processing we can find in the literature are based on two different approaches. A first approach is called *Charge Sharing Discrimination* (CSD) and it is responsible of the rejection of the recognized pulses induced by charge sharing. The goal of this technique is to obtain pulse height spectra (PHS) of better quality, accepting the decrease of statistic. Another

approach is the *Charge Sharing Addition* (CSA) which consists in the recuperation of the correct amplitude information of charge sharing events performing the sum of them. With this technique the goal is to correct the spectral information degraded by the phenomenon of charge sharing without losing photons but accepting a slight degradation of the energy resolution. In Tab. 1.2 are grouped some works we can find in the literature for the correction of charge sharing events.

Author,Year	**Application field**	**Method**
[55] Mathieson et al. - 2002	Hybrid Si X-ray detector	CSD
[56] Abdalla et al. - 2006	Medical Imaging	CSD
[57] - [58] Ballabriga et al. - 2007/2010	MEDIPIX	CSD and CSA
[59] - [60] Veale et al. - 2011/2014	Medical Imaging	CSD and CSA
[52] Brambilla et al. - 2012	X-ray spectroscopy	CSA
[61] Abbene et al. - 2018	X-ray spectroscopy	CSD and CSA

Table 1.2: State of the art of the charge sharing correction methods.

Charge Sharing Discrimination

In 2011, Veale [59] described the discrimination of charge sharing events for the PIXIE-ASIC. It consist on four arrays of 3x3 pixels which can be bonded to a single CdTe or CdZnTe detector, represented in Fig. 1.24. The detector anode consist of four different geometries, and the comparison of two of them are here presented: the arrays with pixels size of 250 μm and 500 μm.

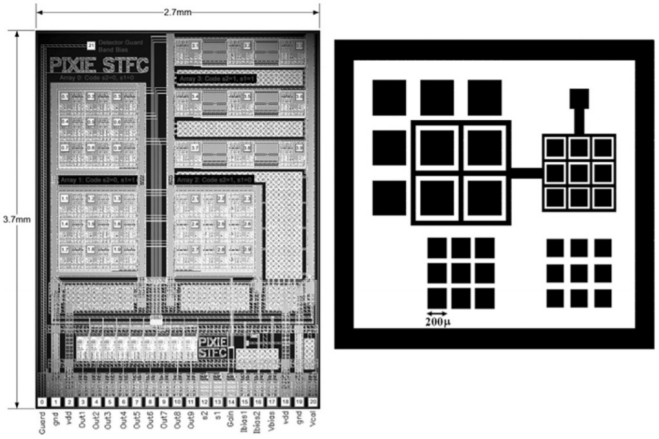

Figure 1.24: (Left) The PIXIE ASIC.(Right) The anode geometry of the PIXIE detector [59].

For the charge sharing correction a low energy threshold was set for both the two configurations. Charge sharing involving energies of less than these thresholds will remain uncorrected as they will not be registered as an event. During an event if two or more pixels are found to be above the set threshold then the event is recognized as charge sharing and removed from the spectrum. Fig. 1.25 shows the measured spectra for two different pixel sizes with and without CSD.

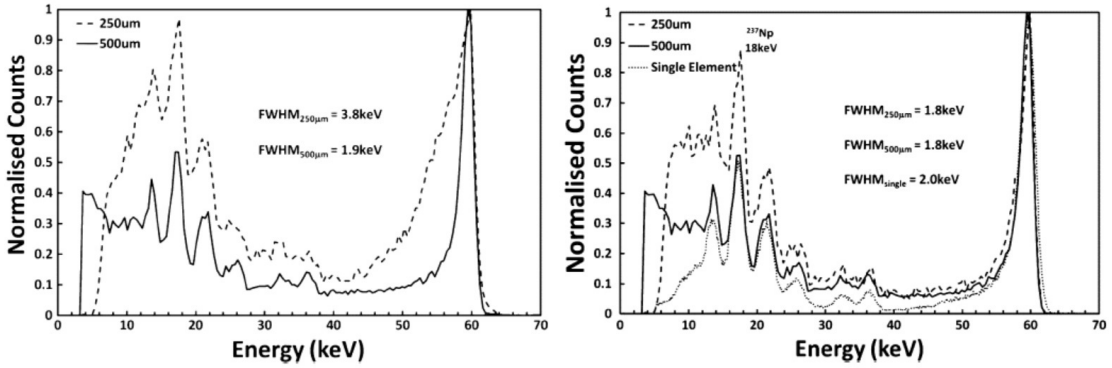

Figure 1.25: (Left) ^{241}Am spectrum of the array 3 (250 μm) and 4 (500 μm) before correction of charge sharing events (left) and after the charge sharing discrimination (right). [59]

For comparison the raw spectrum obtained without correction of charge sharing is also represented. The result shows that the CSD algorithm improves the FWHM of the peak investigated on the ^{241}Am for the pixel of 250 μm from 3,8 keV to 1,8 keV. For the array of 500 μm the improvement on the energy resolution is slighter, from 1,9 keV to 1,8 keV, because of a slighter impact of the phenomenon.

Charge Sharing Addition

The same team developed another approach for the treatment of the charge sharing events involving the CSA algorithm [59]. The CSA technique detects charge sharing events on neighbouring pixels and sum the amplitude of the detected pulses on the pixel that originally received the largest proportion of the energy. The detector consists now of 80x80 pixels on a 250 μm pitch. This work demonstrates that the resulting spectra obtained from the CSA operation mode have improved sensitivity (97%) compared to the raw and CSD corrected data (63%), but suffer from a reduction of energy resolution due to an increase in noise and errors in the addition process from 1,8 keV in CSD to 1,9 keV in CSA [60].

The MEDIPIX team studied also the effect of charge sharing in X-ray imaging application. In 2007 a prototype pixel detector readout chip has been developed

with a new front-end architecture aimed at eliminating the spectral distortion produced by charge diffusion in highly segmented semiconductor detectors (MEDIPIX3) [57]-[58]. Two different operation mode were developed through the years. Fig. 1.26 represents a simulated response function for irradiation with 15 keV photons obtained with the two studied mode of operation.

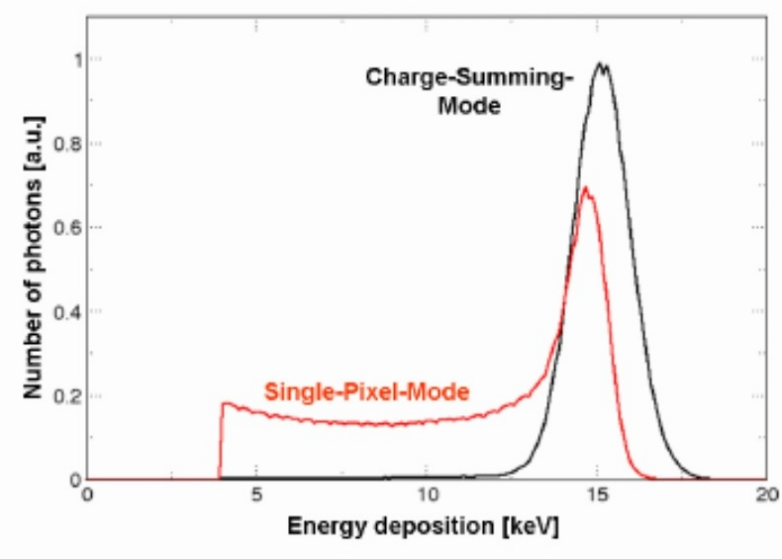

Figure 1.26: Response function in the two pixel configurations operated in SPM (red) and one CSM (black). [57]

The first approach, *Single Pixel Mode* (SPM), provides each pixel completely autonomous of its neighbours. In SPM, each pixel works independently of its adjacent pixels, hence charge sharing effect distorts the energy response of small detector pixels [57]. To remove this effect, *Charge Summing Mode* (CSM) of operation was introduced. In this mode, clusters of four pixels are formed. Deposited charges in each cluster is reconstructed through inter pixel communication, and then arbitration counter assigns it to the pixel in which maximum portion of the charge was deposited. In [58] a comparison of the two mode of operation is proposed. The chip can be configured such that only one input pad in 4 is connected to each channels of the 8x8 matrix with a pitch of 110μm. In this case, up to 8 discriminators and counters are available per pixel and charge summing can take place over a total area of 220μm x 220μm. The results obtained from the comparison show that the front-end noise is 75 e^-rms in SPM and 150 e^-rms in CSM. The count rate has been measured in both modes indicating monotonic behaviour in SPM and up to 17 $\cdot 10^6$ ph/mm2/s in CSM. Moreover, in SPM the image quality is superior compared to the one obtained in CSM. This is caused by the fact that if a pixel has a lower energy threshold compared to its neighbours, then it is possible to count more in this pixel and thus with a false hit allocation.

For this reason, in [62] the new architecture of MEDIPIX3RX was developed. Its goal is to correct the misallocation of hit carried by the previous version. The local charge deposited in the semiconductor detector material by a single event is compared with a threshold. The output of the comparator is fed into an arbitration network to determine which pixel received the largest charge. A counter in the pixel with the largest charge deposited increases if the reconstructed charge in one of its neighbouring summing circuits exceeds the programmed threshold.

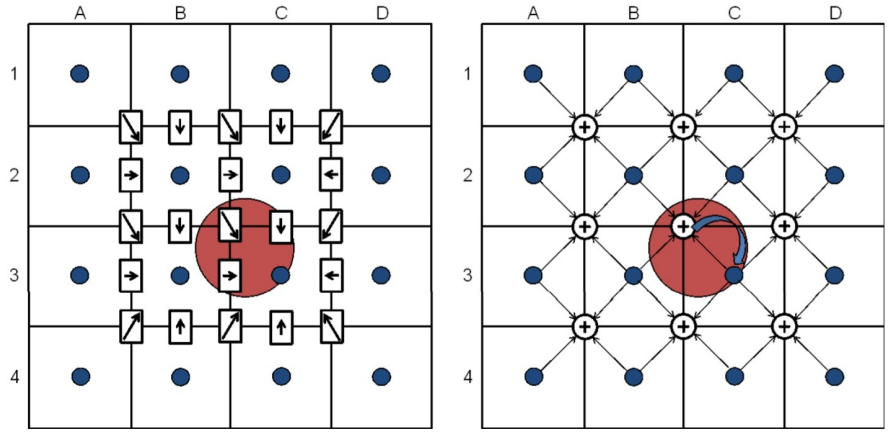

Figure 1.27: Illustration of the CSM algorithm. [62]

Fig. 1.27 represents a simple scheme of the cluster. The MEDIPIX3RX has successfully corrected the limitations of its previous version.

1.4.2 Pile-up rejection and pile-up recovery

In the literature we can find two different approaches in the processing of pulse pile-up, i.e. *Pile-up recovery* or *Pile-up rejection*. The aim of the first approach is to identify the pulses affected by pile-up and recover their correct energy information. The second approach is based more on the detection and consequent rejection of these pulses. According to the application we prefer to use an approach rather than the other. In cases in which the goal is to preserve the energy resolution of the detector response, the rejection of pulse pile-up is used. In case in which the degradation of the energy resolution is less important than the count loss, the technique of pile-up recovery is used. In this Section we are going to present different pulse processing for these phenomenon.

Pile-up recovery - Deconvolution

A common approach we can find in the literature for the pile-up recovery is the method of the *deconvolution*. The concept of deconvolution is widely used in the techniques of signal and image processing. A number of researchers have used deconvolution techniques to reconstruct the initial detector impulse signal from the shaped CR-RC amplifier output pulse [63]. Nowadays, Digital Pulse Processing (DPP) permits to develop real-time algorithms for the detection of pile-up events. In [64] a novel method for the detection of pile-up events using the deconvolution it is used. The method is developed for scintillation detector such as Na(Tl). It consists in a real-time deconvolution filter of different orders (3-points, 4-points and 5-points deconvolution filter) in order to study the performances achievable. They demonstrated that with their approach they are able to reduce the number of pile-up events from 56% to 7%.

Another way of use the deconvolution is to use a fitting technique ([65], [66], [67]). Most of the developed methods adopt the pulse fitting technique with appropriate function describing the pulse shape, but the way of performing the fit can be different. In [67] the method is applied to HPGe detectors and the pulse separation is performed with a Timing Filter Amplifier (TFA) with short shaping time in order to detect the correct information of pulses pile-up. From the TFA we can extract important parameters for the fit, i.e. timing and the number of pulses even if the signal of the long shaping time amplifier is piled up. Fig. 1.28 shows a diagram of the approach developed in this work and the result obtained.

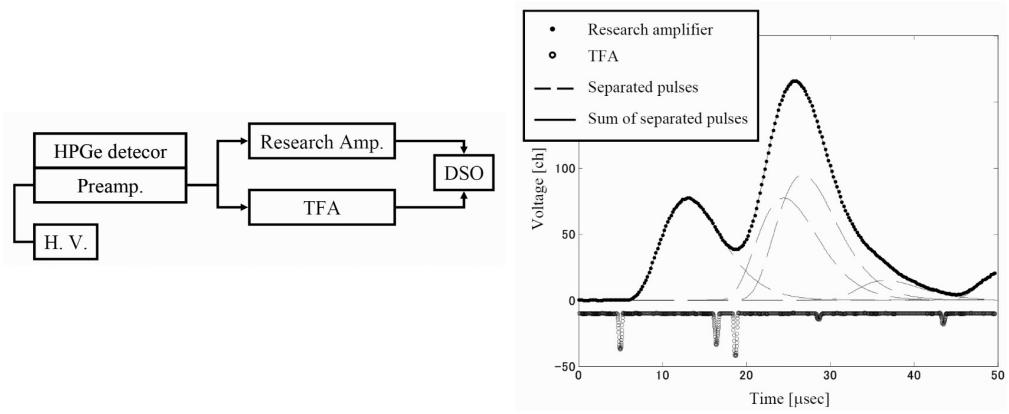

Figure 1.28: (Left) Data acquisition system with TFA. DSO is the digital storage oscilloscope.(Right) Separation of multiple pile-up event. [67]

The parameters related on pulse shape are derived by fitting a pair of waveforms of research amplifier and TFA with good SNR and no pile-up. The fit described in

the paper is then performed routinely to all the acquired events both in presence or not of pile-up. With the method presented in [67] it is possible to separate and recover the pulse pile-up and use these events for the PHS. The result is a method based on a fitting technique for the recover of pile-up events without losing on the count rate and with an improvement of the energy resolution.

Modern field programmable gate arrays (FPGAs) are capable of performing complex discrete signal processing algorithms. Haselman [68] describes a digital pulse pile-up correction algorithm that has been developed on FPGA for a positron emission tomography (PET) scanner. This correction technique uses a reference pulse to extract timing and energy information for pile-up events. Fig. 1.29 represent a diagram of the correction adopted in this work.

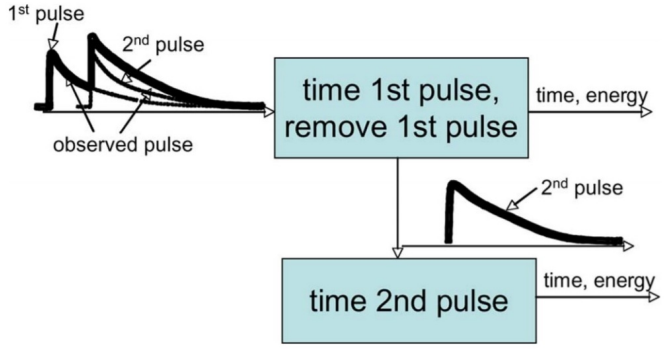

Figure 1.29: Block diagram of the overall pulse pile-up correction algorithm. [68]

In this work, they demonstrated that an all-digital pulse pile-up correction algorithm can recover pulses overlapped up to 80%. Simulations at 1 Mc/s show that this algorithm is able to capture and process 30% more pulses than with a pile-up rejection method. Moreover, compared to the other technique presented of pile-up recovery, this method can be easily implemented in an FPGA with a reasonable amount of resources and without the need of a short shaping time for the pile-up detection.

Pile-up recovery - Other methods

Other works using the approach of pile-up recovery based on the deconvolution technique are summarized in Tab. 1.3.

Author,Year	Application field	Method
[69] Belli et al. - 2008	$n - \gamma$	Separation through quadratic least squares fit
[70] Nakhostin et al. - 2010	Ge detectors	Off-line fitting
[71] Mahmoud et al. - 2012	Na(Tl) detectors	3 methods of deconvolution: 1) Direct search 2) Least square fitting 3) First derivative+max. peak

Table 1.3: State of the art of pile-up recovery approach using the deconvolution/fitting.

The technique of deconvolution is mainly used for γ-ray applications. In these applications the count rate achievable is limited compared to X-ray applications. In the works we analysed the maximum count rate used for the applications involved was of 1 Mc/s. In X-ray applications the rates involved can be higher. For this reason in this application field, other approaches are preferable.

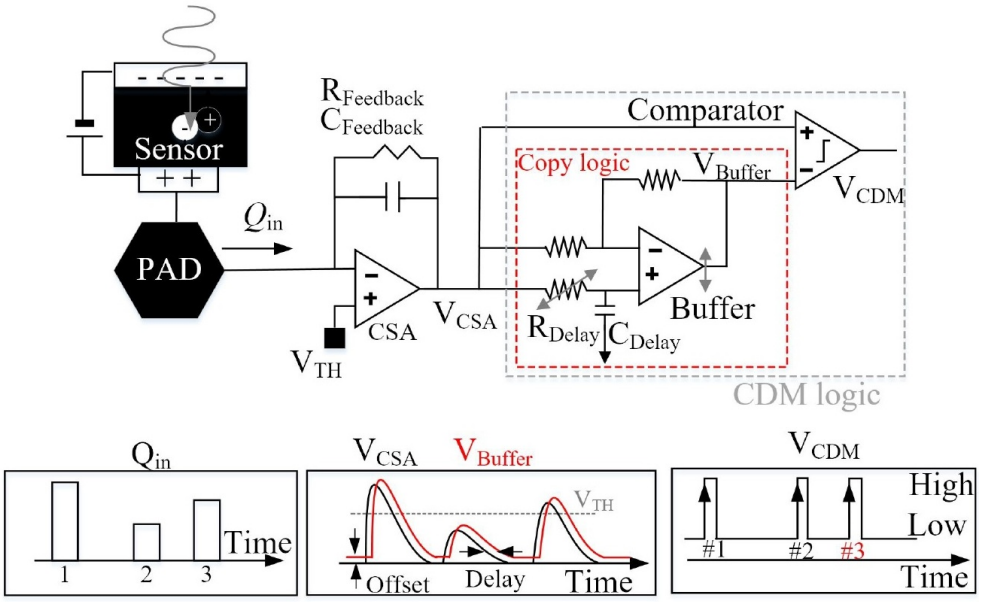

Figure 1.30: A circuit connection for the CDM PC pixel and outputs.

In [72] it is proposed an innovative method to minimize the losses due to the pile-up for high fluxes applications. A photon counting (PC) pixel is studied together with the Cross Detection Method (CDM) for the pile-up detection. Fig. 1.30 represents the circuit connection of the proposed CDM photon counting pixel with outputs. The scheme in the dashed box shows the circuit used to perform the CDM. The idea of the CDM is to add a delay and an offset to the output of the CSA (V_{CSA}) [73]. The resulting signal is called V_{BUFFER} and it is compared to V_{CSA}. Crossing

points are generated when one pulse exceed the other. The comparator produces the high signals outputs (V_{CDM}). In this way, the counter is able to register the incident events without any loss. This is the basic principle of the CDM. Fig.1.31 shows a simulated result of the method proposed.

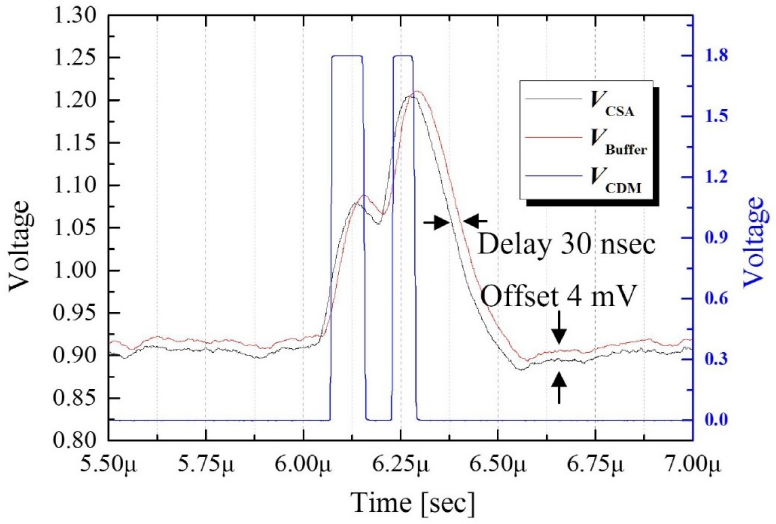

Figure 1.31: Simulation outputs of the proposed CDM PC pixel at pulse pile-up.

The value of the optimal delay is chosen experimentally changing the R_{delay} reported in Fig. 1.30. The value of the optimal offset is done studying the Fast Fourier Transform (FTT) of the output signal of the CSA [73].

Pile-up rejection

The approach of pile-up rejection has been widely studied for high flux X and γ-ray spectrometry applications. A number of methods, based on pulse shape discrimination have been proposed to identify pulses affected by pile-up. Some examples are: leading edge discrimination, monitoring the incoming signal and detecting pile-up events based on the rising edge of the pulse signal [74], methods identifying pile-up events by Time Over Threshold (TOT) [75], pulse peak detection [76] and matched filter [77].

In 2015 a group from the University of Palermo (Italy), used the approach of pile-up rejection to mitigate the distortion in radiation measurements [81]. In this work a double shaping circuit is used. The fast one is responsible of the pile-up rejection. The slow one is responsible of the Pulse Shape and Height Analysis (PSHA) on the pulses selected by the pile-up rejection. The technique performs a selection of time windows of the charge sensitive preamplifier (CSP) waveform

for the slow shaping. Each selected time window of the CSP waveform is called "Snapshot", while the width of this window is called "Snapshot Time" (ST). The selection of pile-up events is related to the reference time of each fast SDL pulse, i.e. the time when the falling edge of the SDL pulse crosses the threshold. If two detected fast SDL pulses are within ST/2 of each other, then there won't be any selected pulse. A pulse is accepted if it is not preceded and not followed by another pulse in the ST/2 time window periods. The energy resolution strongly depends on the ST values. As the shaping time of classic analog systems, long ST values give better energy resolution. Fig.1.32 represents the selection of the temporal window for the slow shaping circuit.

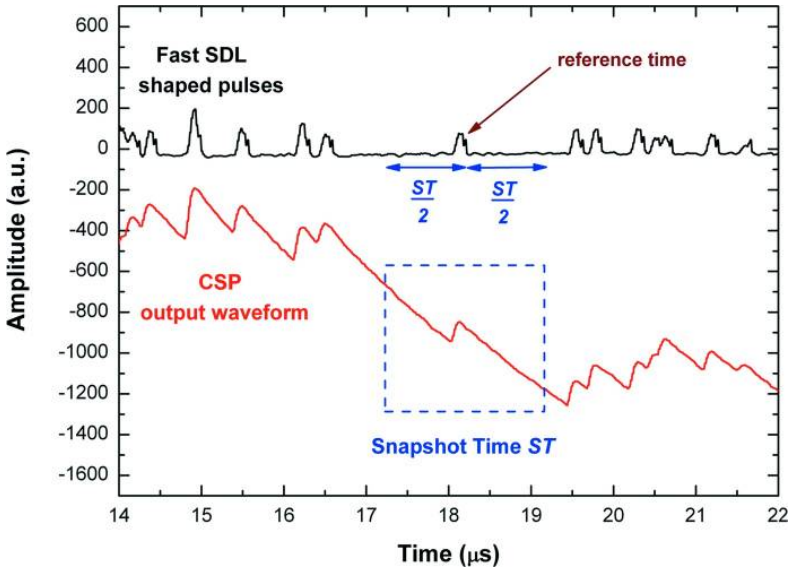

Figure 1.32: ST selection by the PUR for the slow shaping circuit. [81]

The pulses in Fig. 1.32 represent X-rays signals from an X-ray tube impinging on a CdTe detector with a count rate of 2,2 Mc/s. The final goal of this job was to study the behaviour of the dead-time of the system in three different configuration. Two types of dead-time are initially presented, type I and type II. They do not take into account the losses related to pile-up. For this reason a third model is here proposed, dead-time type III in which the effect of the pile-up is considered. The comparison of the three method is then presented and in particular for the third the technique of pile-up rejection is considered. The result is that with the pile-up rejection it is possible to obtain an higher throughput with a loss on the energy resolution.

Others important works using the pile-up rejection are summarized in Tab. 1.4.

Author,Year	Application field	Method
[78] Sharma et al. - 2015	X-ray spectroscopy	Rejection through the help of simulated X-ray spectra compared to raw spectra
[79] Kun et al. - 2015	PCD	FPGA PUR with 3 thresholds
[80] Gu et al. - 2016	PET scanner	Position Shift Rejection (PSR) using 3 amplitude thresholds

Table 1.4: State of the art of the pile-up rejection approach.

1.4.3 Ballistic deficit compensation methods

The other possible source of degradation of the energy resolution of the detector response is the ballistic deficit. Many approaches were developed in order to compensate this effect on the shaper output.

The shaping circuit with a short shaping time, that here we are going to call *fast shaper*, permits to detect events occurred from multiple interaction. In [21] this type of approach is used.

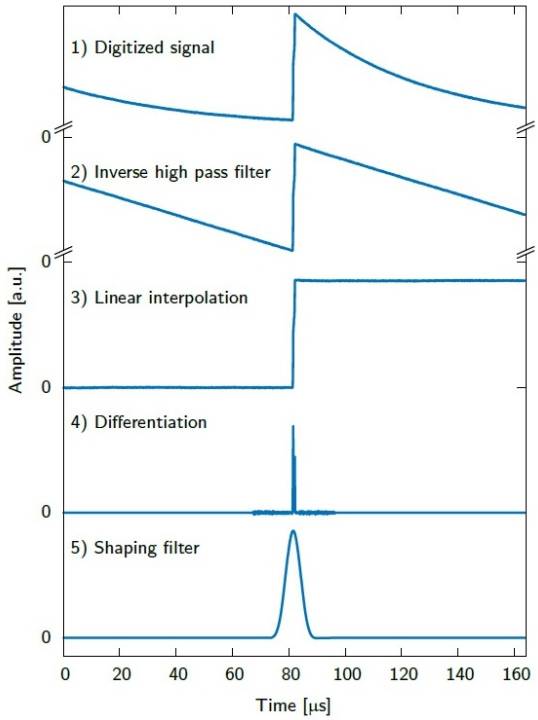

Figure 1.33: Principal steps for the pulse height reconstruction in [21].

The method is developed for HPGe detectors, used for very high resolution applications. In particular they use a technique called Multi-Site Event Cancellation

(MSEC), to preserve the energy resolution achievable. The different steps of the pulse height (energy) reconstruction are illustrated in Fig. 1.33. The first three steps are used for the pole-zero cancellation. They are followed by a differentiation and a shaping filter (pseudo-Gaussian with a shaping time of 6 μs). The Multiple Interaction step is introduced before the shaping filter, between the poit 4) and 5). The method is particularly suitable for events with energy deposition in multiple locations (from where the name) that presents a variation in the charge collection time. Fig. 1.34 represents the results obtained when the MSEC is enabled or not for different shaping times of the pseudo-Gaussian filter. The MSEC method improves the energy resolution obtained whit short shaping times.

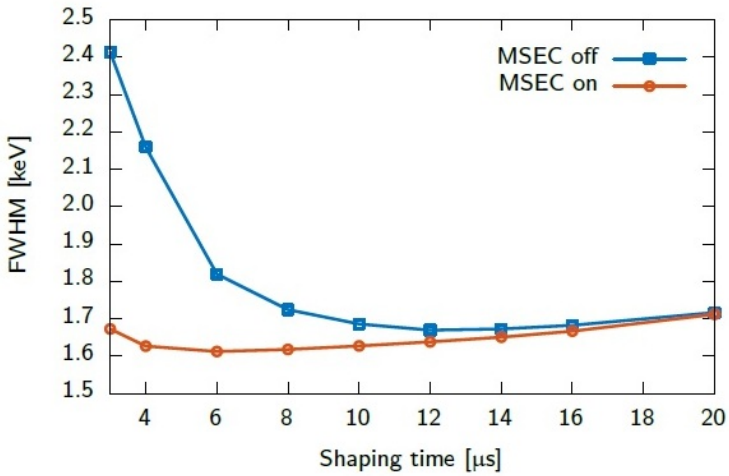

Figure 1.34: The energy resolution (FWHM) of the 1332,5 keV γ-ray line of ^{60}Co obtained with the pseudo-Gaussian filter for different shaping times. [21]

Double shaping circuit for ballistic deficit compensation

Other works use a double shaping circuit working in parallel. The short shaping time is responsible of detecting multiple events occurring in a short temporal window, the long one is responsible of collecting all the charges. Fig. 1.35 represents a diagram of a possible way to use the double shaping circuit.

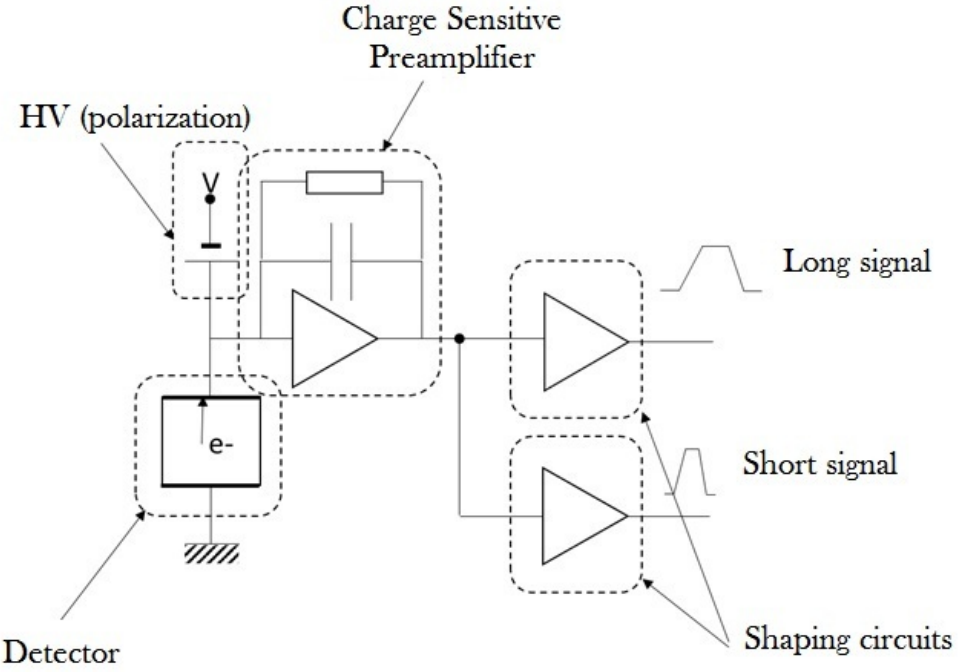

Figure 1.35: Example of electronic chain for signal processing with the two shaping circuits.

In [82] and [21] the ratio between the measured amplitudes from the output of the two shaping circuits is computed. The goal is to estimate a correction factor to apply to the short shaping circuit and compensate the ballistic deficit. In [21] the correction of ballistic deficit is performed for large coaxial Ge detectors. The method is based on the relationship between the amplitude deficit and the time delay Δt in the peaking time of the pulses:

$$\frac{\Delta V}{V_0} = \left(\frac{\Delta T}{T_0}\right)^2 \tag{1.7}$$

Where V_0 is the peak amplitude of the output signal for a step function input, ΔV is the ballistic deficit, T_0 is the peaking time of the output signal for a step function input and ΔT is the delay on the peaking time for an input with a short peaking time compared to the step function. The peak delay is measured and the correction factor, $V_0 \left(\Delta T/T_0\right)^2$, is then computed. Finally, this correction factor is added to the shaper output to produce the final correct signal. In the paper it is demonstrated that this method has to be improved because of the significant sensitivity to variation of the signals rise-time. For this reason, an improvement of this method is performed in the successive work [82]. The improvement in this work is to add a correction factor which describes the variation of the signal rise time. Fig. 1.36 represents the circuit developed for the correction of the ballistic deficit for unipolar and bipolar signals.

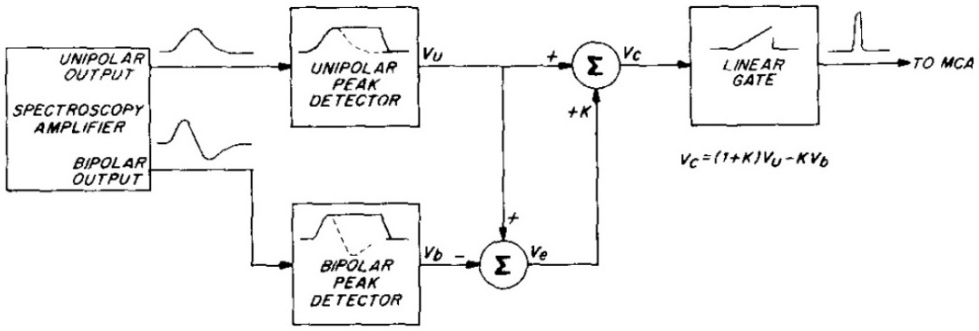

Figure 1.36: Example of electronic chain for signal processing with the two shaping circuits.

Normally the correction factor (K) is rise-time dependent and it is measured by subtracting the bipolar signal from the unipolar one. With the technique developed in this work the peak amplitudes of the bipolar and unipolar signal are detected and then subtracted. In this way an error, V_e, is produced. The addition of this error to the unipolar signal reduces the sensitivity to the input rise-time and thus the compensation is well performed. The distorted spectrum before the compensation is characterized by a Full Width at Half Maximum (FWHM) of 2,74 keV. after the correction the spectrum is characterized by a FWHM of 1,84 keV. The results presented here are evaluated using a small (20%) volume p-type closed-end coaxial detectors in conjunction with a signal processor having a 2 μs peaking time.

Other works using different approaches based on the use of a double shaper for the ballistic deficit compensation are summarized in Tab. 1.5. It is important to underline that all the works here presented are adapted for high-energy resolution spectroscopic detectors.

Author,Year	**Application field**	**Method**
[18] Goulding - 1988	Ge spectrometers	Double shaper
[20] Moszynski - 1991	Large Ge detectors	[82] and [18] adapted to 3 different sensors
[20] Moszynski - 1991 [83] Radeka - 1988	Spectroscopy Amplifier	Gate Integrator
[19] Goulding - 2002	Very large Ge detector	Double shaper

Table 1.5: State of the art of different ballistic deficit compensation methods.

1.5 Conclusions

In this Chapter we have presented the state of the art of X-ray imaging detectors. We presented three different detection modes, integration, counting and spectrometric mode, then we focused our attention on semiconductor spectrometric detectors such as CdTe and CdZnTe. In a second moment we presented in detail the state of the art of hybrid pixel detector readout ASICs for spectrometric X-ray imaging developed by many research groups.

The development of spectrometric detector for high-flux X-ray imaging applications evolved more and more in the last decades. A spectrometric pixel detector with high resolution capabilities was developed in CEA-LETI. The physics of the detector was then presented together with the effects, such as pile-up, charge sharing, weighting potential cross-talk and ballistic deficit, affecting the performances of the detector response. Finally, the state of the art of the processing for the mitigation of these effect is discussed.

Chapter 2

The Spectrometric Pixel Detector

In this Chapter we describe in detail the read-out electronic developed in LDET. The pulse processing algorithms were developed in order to perform high-resolution and high-flux spectrometry measurements under X-rays. The characterization of the spectrometric pixel detector developed during this thesis work will be presented. Different shaper configurations for the data processing were studied in order to find the best compromise in terms of energy resolution and dead-time of the system.

2.1 Experimental setup

Figure 2.1: Detector setup developed in CEA-LETI: shield aluminium box (left), analog read-out circuit (center) and digital circuit (right).

The detector laboratory (LDET) of CEA-LETI has developed a novel 16-channel fast read-out electronic circuit able to perform high-resolution spectrometry measurements at X-ray fluxes up to 10^7 X/mm^2/s [84]. For each channel, the signal is continuously digitized at 100 MHz by a 10 bit Analog to Digital Converter (ADC). An FPGA (Altera Cyclon II) controls the acquisition and reconstructs the energy spectra on 256 bins for each channel. The read-out electronic circuit is coupled to 4x4 CdTe pixel detector with ohmic contacts. The proposed 16-channels prototype

is developed for testing new Digital Pulse Processing (DPP) algorithms for pixel detectors. The 4x4 CdTe detector array was purchased from ACRORAD (Japan) with a pixel pitch of 800 μm. The detector thickness is 3 mm and ensures good stopping power for X-rays of up to 160 kV. The novel architecture developed by LDET takes advantage of the FPGA, which allows the implementation of advanced digital algorithms to process the signals, among them charge sharing, weighting potential cross-talk and pile-up correction. Fig. 2.2 shows a diagram of the readout electronic circuit.

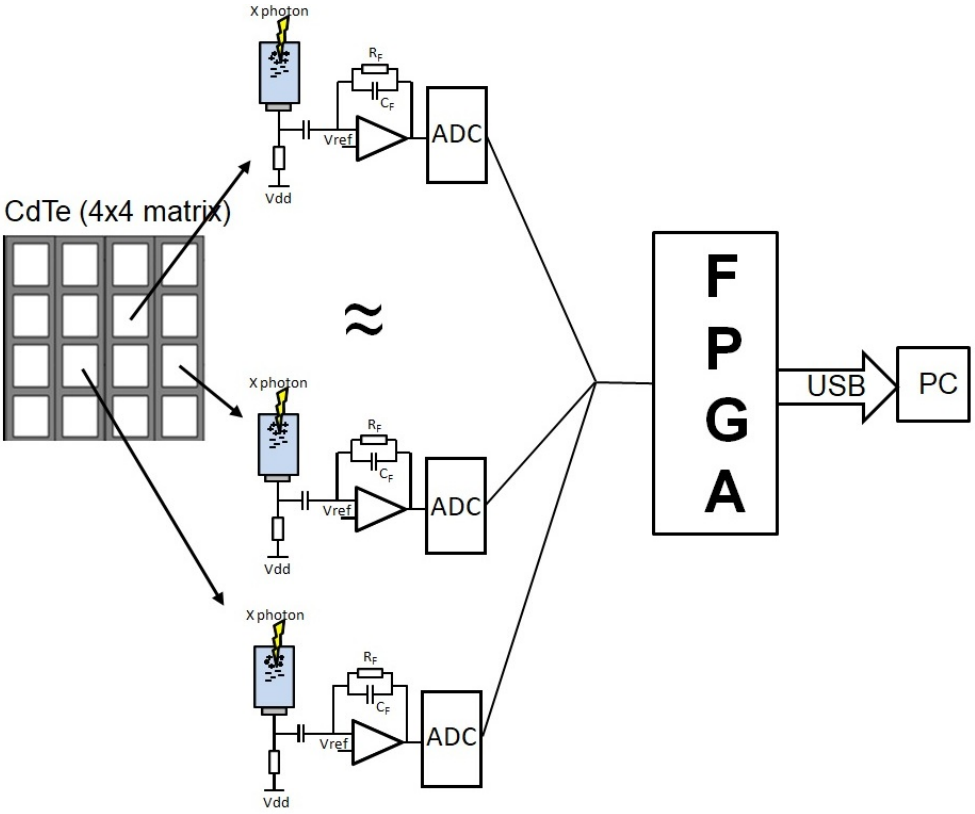

Figure 2.2: Readout electronic circuit architecture. [84]

Typical Pulse Height Spectra (PHS) obtained in real-time with this architecture are shown in Fig. 2.3. They represents the comparison between the 16 channels and they show that there is only a slight variation in the main peak position and in the energy resolution among pixels. As we already have presented in Chapter 1, the low pulse-height tail of the spectra is attributed to charge loss and charge sharing effects. The charge loss is due to many physical phenomena such as Compton scattering, K-shell fluorescence or thermal diffusion of the photo-generated charge carriers [10]. The pulse processing algorithms used to reduce these effect will be presented in the following Section.

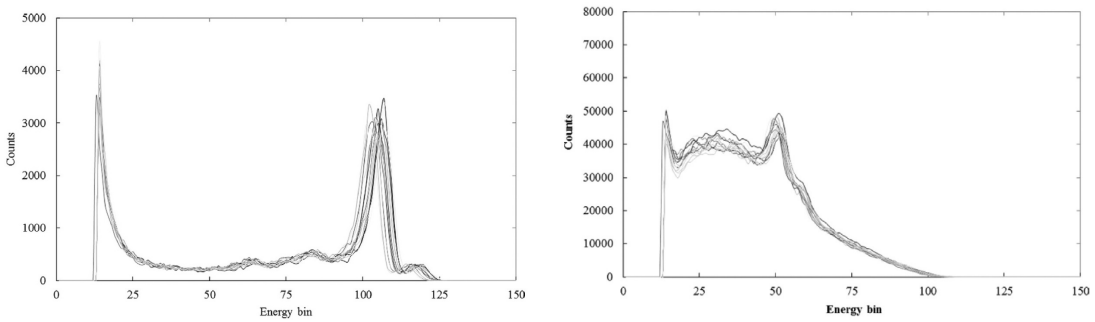

Figure 2.3: (Left)Pulse-height spectra from a ^{57}Co γ-source and (right) from a 120 kV X-ray source obtained with the CdTe 16-pixel with a count rate of 2 Mc/s. [10]

2.2 Pulse Processing algorithms

In this Section the pulse processing techniques developed by LDET for the reconstruction of the 16 pixel spectra on 256 energy channels are presented. Fig. 2.4 represents the architecture of the pulse processing implemented on the FPGA for one single pixel. The circuit is reproducible identically for the other pixels.

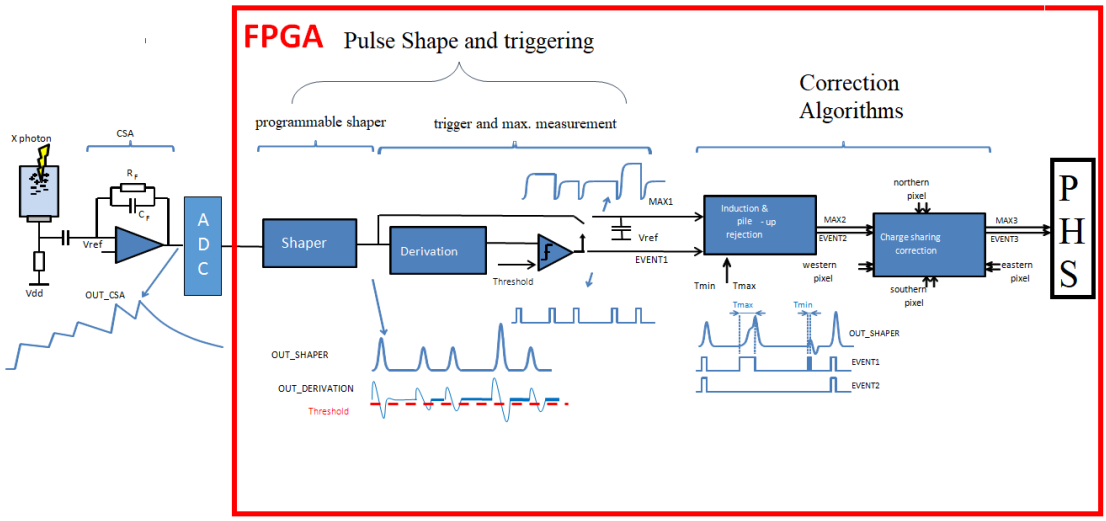

Figure 2.4: Full architecture block developed by LDET. Pixel principle, front-end electronics and signal processing.

The digital processing developed on the FPGA can be divided in three main sectors:

- The *Pulse Shape and triggering*: a programmable shaping circuit responsible of the shaping of pulses from the Charge Sensitive Amplifier (CSA), the triggering of the shaped pulses for their detection and the amplitude measurement, together with the baseline restoration.

- The *Correction Algorithms*: processing of undesirable events for the spectra

reconstruction, i.e. the charge sharing, the weighting potential cross-talk and the pile-up events.

- The *Pulse Height Spectra*: reconstruction of the energy spectra on 256 energy bin after the correction algorithms are performed.

In the following Sections, we are going to analyse in detail how to perform the shaper, the trigger algorithm and the correction algorithms.

2.2.1 Programmable shaper

The shaper is used to process the pulses from the CSA and to perform noise filtering. The signals delivered by the CSA have a long exponential decay time and successive pulses will have an high probability to overlap. The role of the shaper is to transform these signals into short pulses with amplitudes proportional to the induced charge.

In the literature many ways were developed for the pulse shaping (Gaussian, cusp-like, triangular). The major challenge of these digital pulse processing systems is represented by the difficulty of dealing with high rates drawbacks [8]. The recursive algorithm of the trapezoidal filter [85] and the classical Single Delay Line (SDL), which have the advantage of being easily implemented on FPGA, are presented here.

The Single Delay Line

In the algorithm of the *Single Delay Line*, the signal from the CSA is delayed of a quantity and attenuated by a fraction proportional to the decay time of the CSA pulse. The obtained pulse is then subtracted to the original pulse from the CSA. The algorithm is illustrated in Eq. 2.1:

$$V_{SDL}(t) = V_{CSA}(t) - V_{CSA}(t - T_D) \cdot e^{-(T_D/\tau_F^*)} \tag{2.1}$$

Where V_{SDL} is the voltage amplitude of the SDL output, T_D is the delay time and V_{CSA} is the output signal from the charge sensitive amplifier. The attenuation factor τ_F^* it acts as a pole-zero cancellation. Fig. 2.5 represents a SDL shaping where (a) $\tau_F^* = \tau_F$ and (b) $\tau_F^* \neq \tau_F$.

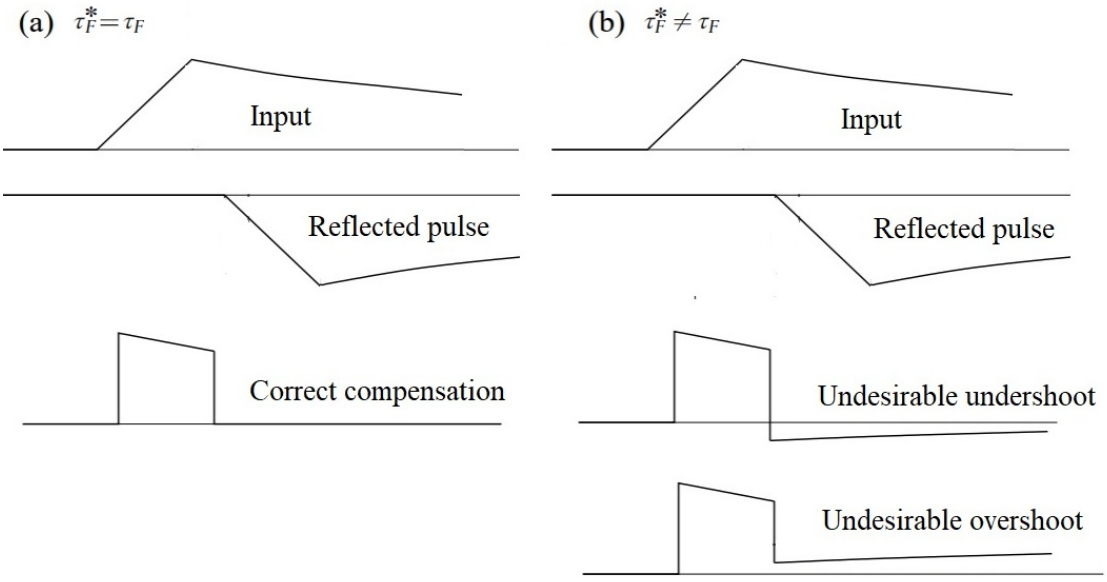

Figure 2.5: (a) $\tau_F^* = \tau_F$ and (b) $\tau_F^* \neq \tau_F$.

By setting the right value of τ_F^*, i.e. $\tau_F^* = \tau_F$ (where τ_F represent the time constant (RC) of the falling edge of the CSA), it is possible to compensate the undershoot ($\tau_F^* > \tau_F$) or overshoot ($\tau_F^* < \tau_F$) due to the slope of the falling edge of the CSA output. The consequence of an incorrect compensation is a false estimation of the pulse amplitude. The main parameter of the algorithm is the delay T_D. Fig. 2.6 represents the result of this algorithm with two different delays and a fixed peaking time, T_P, of the signal from the CSA. We call peaking time, the time between the beginning of the signal and its maximum.

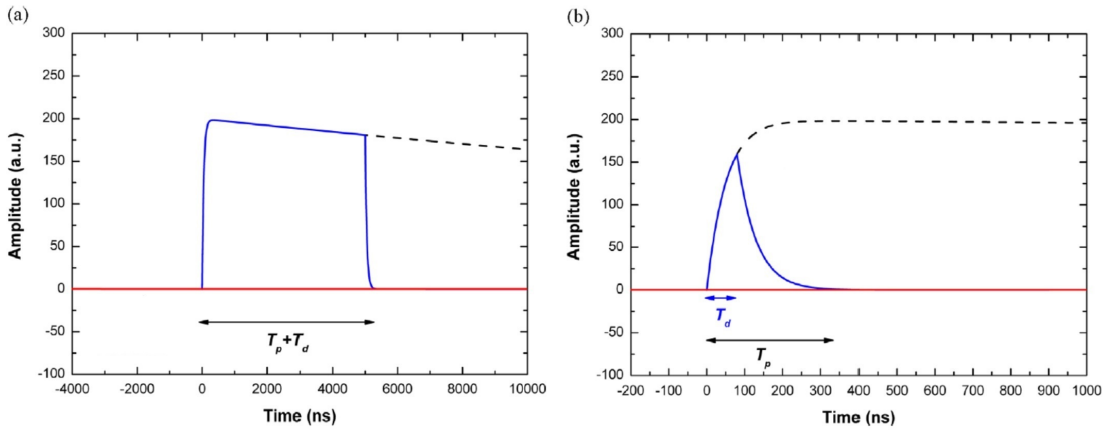

Figure 2.6: Single isolated CSA output pulse (dashed black line) and the SDL shaped pulse (solid blue line) with a delay time (a) $T_D > T_P$ and (b) $T_D < T_P$. [8]

The use of shaping times larger than the peaking time of the CSA signal ensure that the collected charge are correctly measured. If the shaping time is shorter compared to the peaking time, a fraction of the CSA signal will not be taken into

account. This is the phenomenon of ballistic deficit. Normally, the information obtained from the amplitude of the pulses is still proportional to the released energy of the interaction occurred, but the SNR will be affected.

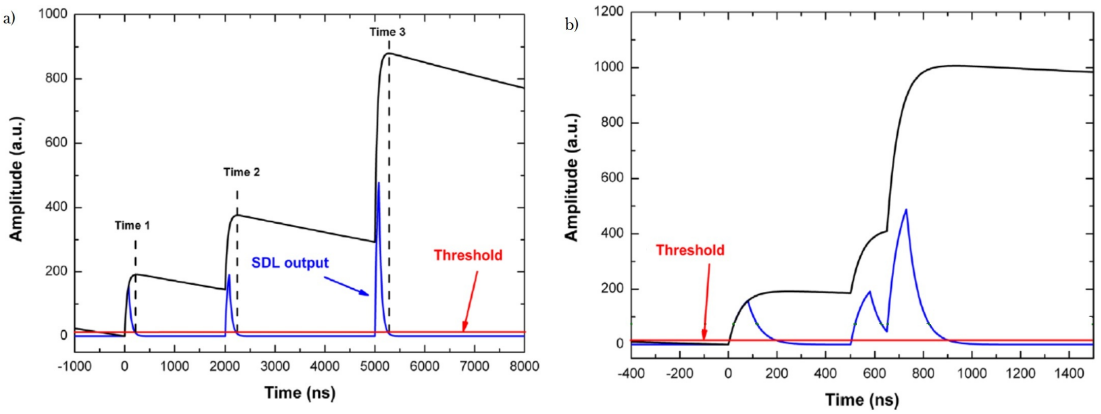

Figure 2.7: CSA output (black) with three pulses (arriving at three different times) and the SDL shaped waveform (blue) with T_D<T_P for a tail pile-up (a) and for a case of peak pile-up (b) [8].

Fig. 2.7 represents the output of the CSA and the corresponding output of the SDL with T_D<T_P when there is pile-up. The SDL shaping with T_D<T_P can be very helpful to reduce pile-up. The efficiency of the algorithm proposed is visible when the count rate increases and the phenomenon of pile-up becomes significant.

The Trapezoidal filter

Another approach of shaping circuit, able to convert the long exponential tail of signals coming from the CSA with a shorter symmetric pulse is the *Trapezoidal Filter*. The trapezoidal shaper is a FIR filter, easy to implement in FPGA and able to increase the SNR. The trapezoidal filter can be described as a filter able to transform the typical exponential decay signal generated by the CSA into a trapezoid that presents a flat top whose height is proportional to the amplitude of the input pulse. The trapezoidal filter is considered as the closest FIR filter to the optimal shaper, known as cusp filter. This latter is an Infinite Impulse Response filter (IIR) and for this reason difficult to implement both in analog and digital circuits. The recursive algorithm that converts a digital exponential pulse $v(n)$ into a symmetrical trapezoidal one $s(n)$ is given by:

$$d^K(n) = v(n) - v(n-K); \tag{2.2}$$

$$d^{K,L}(n) = d^K(n) - d^K(n-L); \tag{2.3}$$

$$p(n) = d^{K,L}(n) + p(n-1); \tag{2.4}$$

$$r(n) = M \cdot d^K(n) + p(n); \tag{2.5}$$

$$s(n) = r(n) + s(n-1). \tag{2.6}$$

Where $v(n)$, $p(n)$ and $s(n)$ are equal to zero for $n < 0$. Fig. 2.8 represents a 3 block diagram of the recursive algorithm presented.

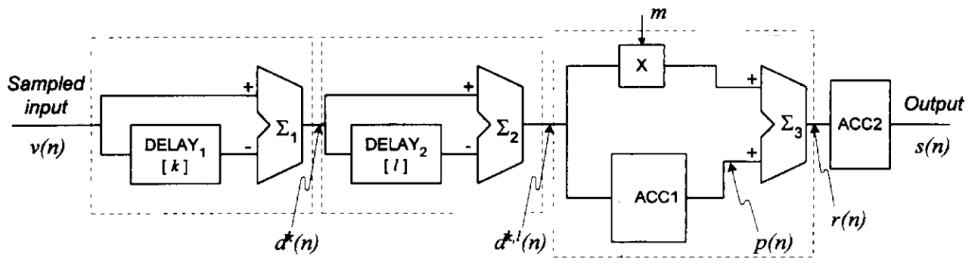

Figure 2.8: Block diagram of the digital trapezoidal shaper. [85]

The parameter M depends only on the decay time τ of the exponential pulse and on the sampling period T_{clk} of the digitizer. It acts as the pole-zero cancellation and it is equal to $M = 1/[e^{\frac{T_{clk}}{\tau}} - 1]$. The two delay lines are linear time invariant and they are characterized by two important parameters: K and L. They represents the number of samples for which the signal is delayed. Moreover, they are the main responsible of the trapezoidal output shape. In fact, the duration of the rising (falling) edge of the trapezoidal shape is given by the smaller value between K and L (min(K,L)), while the duration of the flat top is given by the absolute value of the difference among them: (|K-L|). The duration of the flat top should be larger than the peaking time of the CSA, in order to ensure the correct collection of the charges. If the flat top is shorter than the peaking time, we have ballistic deficit.

Trigger and amplitude measurement

The most common method for triggering the signal is to use an amplitude threshold. This latter is applied to the output of the shaper and the signal is triggered once it passes the amplitude threshold. This method has an important drawback. Fig. 2.9 represents two simulated pulse pile-up from the CSA with the relative shaped signals from the SDL circuit with a $T_D < T_P$. The amplitude threshold is represented too. When two successive pulses affected by pile-up are not enough spaced in time, the method of the threshold is not able to separate two pulses.

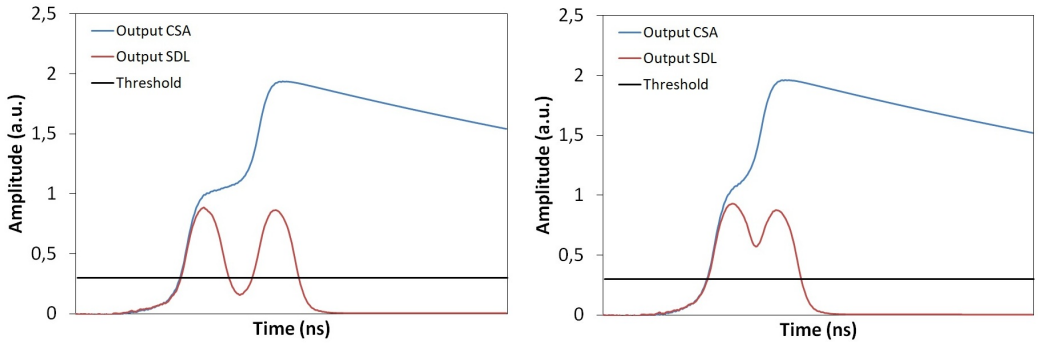

Figure 2.9: Two cases of maxima detection through the use of the threshold.

In the first case, the two pulses are separated enough in time and the shaped pulse is able to return to its baseline. In this case the threshold technique is able to detect both of them. In the second case, the signal from the SDL is not capable to return to its baseline before the beginning of the second one. The threshold technique fails to separate the two events. For this reason we have developed a new trigger method.

The method is based on the first derivative of the signals from the SDL. This operation can be easily implemented with only one delay unit, since the digital first derivative is defined as follow:

$$D(i) = SDL(i) - SDL(i-1) \tag{2.7}$$

Where i represents the sample forming the pulse. Fig. 2.10 shows the principle of the method of the first derivative used as a trigger technique.

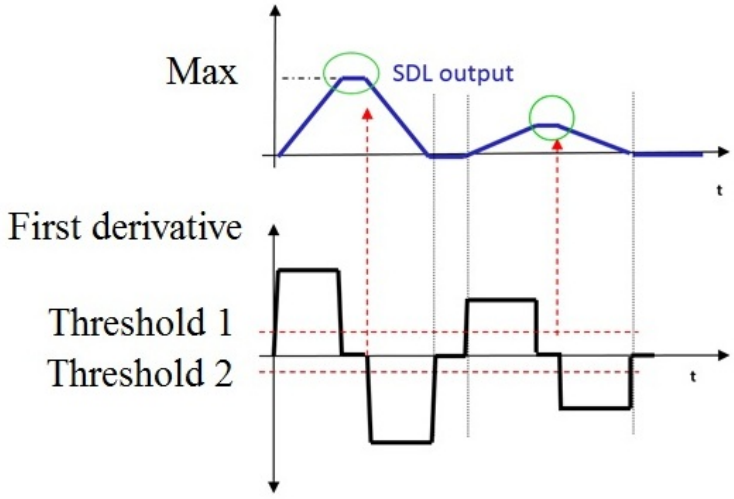

Figure 2.10: (Top) Theoretic output from the SDL for two different photon. (Bottom) The first derivative with its two thresholds for the detection of the maxima.

The first derivative of the SDL output is calculated continuously. A system of two thresholds, one positive and one negative, is used. The positive threshold is compared with the positive lobe of the first derivative. The negative threshold is used to recover the value of the maximum of the shaped pulses. The positive threshold is responsible of detecting the signal but also to activate a counter. In fact, with this technique it is also possible to determine the maximum of the shaped pulse. The two threshold works as a "start" and a "stop" of the process. When the first derivative is smaller compared to the positive threshold and bigger than the negative one, then the value of the amplitude of the shaped signal is registered.

The advantage of this trigger technique is its ability of detecting two successive pulse that can not be distinguished by the simple amplitude threshold. Fig. 2.11 represents this concept with two different case of pile-up.

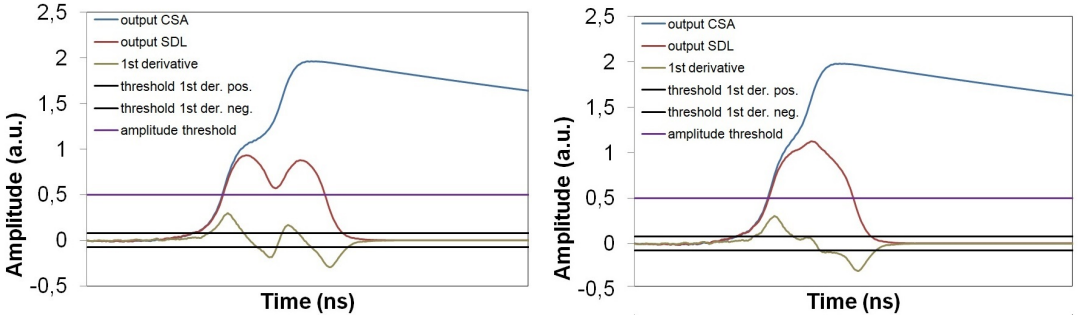

Figure 2.11: Two cases of event detection through the use of the first derivative when we can distinguish the two pulses (left) and we are not able to do it (right).

The first case is the same case shown in Fig. 2.9 to demonstrate the limit of the threshold technique. With the first derivative threshold technique the two amplitudes are well detected and measured. The second case represents a limit situation where the first derivative threshold technique fails to distinguish two successive pulses. When the time interval is smaller than the peaking time of the shaped pulses, the derivative signal remains above the positive threshold until the decay of the second pulse. In this situation the amplitude information recorded is incorrect.

Baseline Restoration

In order to measure with accuracy the pulse amplitude, a *Baseline Restoration* (BLR) is performed. The aim of the baseline restoration is to cancel the baseline shifts due to DC offsets, thus avoiding energy peak drifting during the signal acquisition. In our case the BLR is performed by evaluating the average of 16 samples preceding

the leading edge of the triggered pulses. This means that the baseline is measured every time there is no detected pulse. The concept is represented in Fig. 2.12.

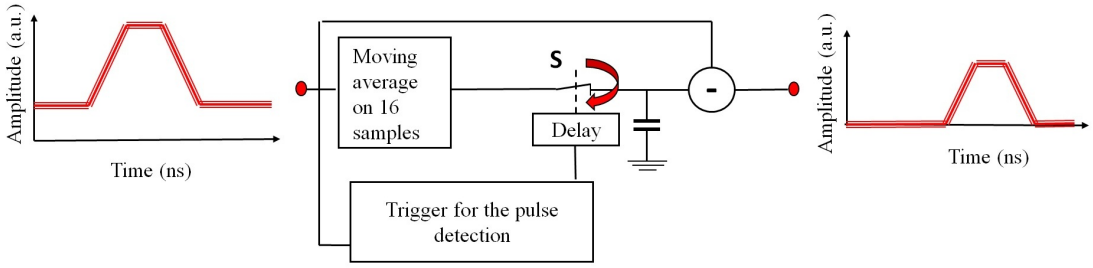

Figure 2.12: Pulse from the shaping circuit and the concept of the baseline restoration active or not.

The block of the moving average on 16 samples is active every time there is no trigger. The operation of subtracting the correct value of the baseline from the incoming pulse, is regulated by a switch S and a memory. When the circuit of the trigger does not detect a pulse, the moving average is calculated and the switch is closed in order to store the value of the baseline in a memory. As soon as the trigger circuit detect a pulse, the switch is opened and the value of the baseline stored in the memory is subtracted with the measured amplitude of the pulse. This will be the correct value of the signal amplitude.

2.2.2 Correction algorithms

This second block is responsible for the correction of undesirable effects which can affect the detector response. The technique of the first derivative is able to reduce the effect of pulse pile-up, but sometimes it is difficult when they occur at almost the same time. When the count rate increases, this phenomenon is more significant and when the number of pulse pile-up increases it is necessary to use other rejection techniques in order not to degrade the detector response. Others sources of error, responsible of the presence of low energy informations in the spectra are the weighting potential cross-talk and the charge sharing effect.

Pile-up rejection

The effect of pile-up on the pulse height spectra is a loss of counts and a significant number of false counts on higher energies. For the detection of these events we use the temporal duration of the first derivative positive lobe of the SDL output. The first derivative of the shaped signals is characterized by a positive and a negative lobe. The pulse maximum is reached when the derivative signal crosses the zero

level. The duration of the positive lobe of the first derivative of a signal represents its rise-time. It was observed that the rise time of the pulses affected pile-up is abnormally long. In order to check the temporal duration of the rise-time of the pulse a new parameter, T_{max}, is introduced. Two thresholds are considered for the following technique, a positive and a negative one, as already seen in Fig. 2.10. When the first derivative of the SDL crosses the positive threshold, a counter is started according to the clock cycle. If the temporal duration of the counter, which increase with the clock cycle, is longer than T_{max} (equal to 80 ns), then the event is rejected because recognized as pile-up. The counter stops when the fist derivative cross the negative threshold. In case of single event, in this situation the value of the amplitude is registered. Fig. 2.13 summarizes the concept of the pile-up rejection.

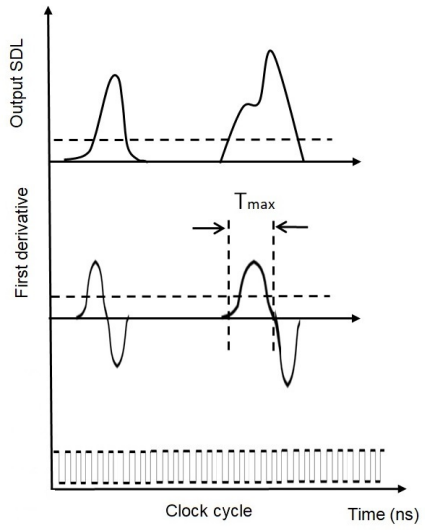

Figure 2.13: Simulated output of the SDL with one pulse affected by pile-up.

In this example, before the rejection algorithm is applied, 2 events are detected. After the rejection algorithm only 1 of them are suitable to be registered in the energy spectrum.

Weighting potential cross-talk rejection

The effect of weighting potential cross-talk on the pulse height spectra is a number of false counts on very low energies. The rejection of pile-up events and weighting potential cross-talk is done with the same process. Contrary to pulse pile-up we observed that pulses affected by weighting potential cross-talk have a very short rise-time. Pulses induced by weighting potential cross-talk are recognized with the comparison of the duration of the positive lobe of the first derivative with a new

parameter, T_{min}, set at 20 ns. If recognized as weighting potential cross talk, the event is rejected because it would be registered in the low energy tail of the energy spectrum. Fig. 2.14 summarizes the concept of the weighting potential cross-talk rejection.

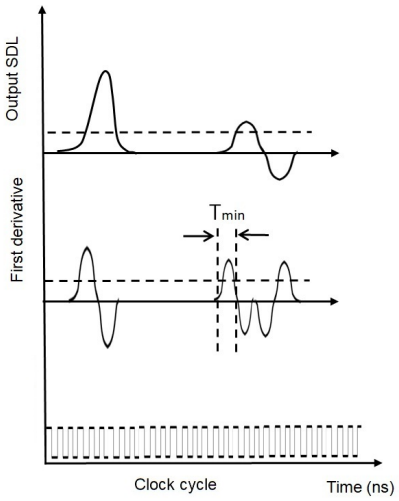

Figure 2.14: Simulated output of the SDL with one pulse affected by weighting potential cross talk

Before the rejection algorithm is applied, 2 events are detected. After the rejection algorithm only the first pulse is registered in the energy spectrum.

Charge sharing correction

The other processing algorithm we want to implement is the one responsible for the correction of the charge sharing effect. A simple charge sharing correction can be performed by summing the charges measured on neighbouring pixels, each time a pulse is detected on one pixel. The correction algorithm for charge sharing events considers groups of cluster of 5 pixel, one in the center, one in the north, one in the south and two at east and west in relation to the central one. A time coincident window (TCW) of 20 ns is set. The correction of charge sharing event is performed after the weighting potential cross-talk detection using the first derivative. In fact, if the process implemented for the rejection of these events does not recognized a weighting potential cross-talk and the counter stops before the limit imposed for the pile-up rejection, then a comparison among the clustered pixel is performed. If a pulse on one of the four neighbouring pixels is detected with the same process in the fixed TCW, then the computed amplitude are summed on the pixel with the higher pulse. Fig. 2.15 shows the principle of the charge sharing correction. Two pulses are detected within the coincidence window on the central pixel and on

the west neighbour. The amplitudes of the two pulses is summed and the result is attributed to the pixel with the larger pulse amplitude.

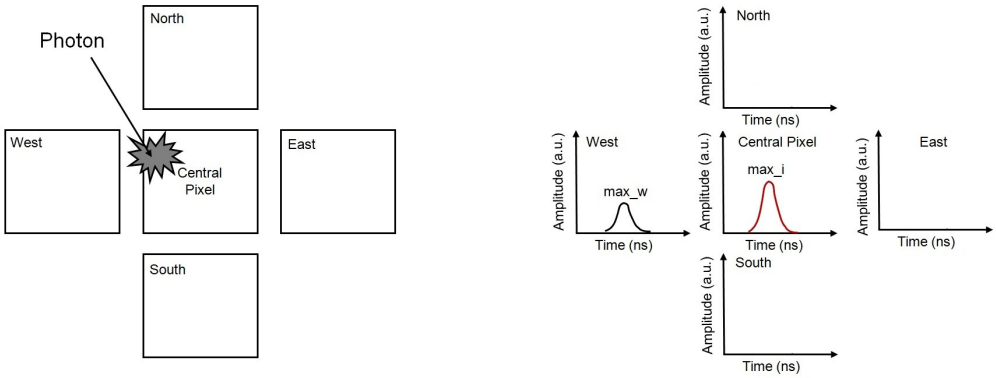

Figure 2.15: Diagram for the detection of the charge sharing events and its consequent correction.

An important fact to take into account is that the weighting potential cross-talk signals can be seen as sharing event among two pixels. When this happens a pulse from a pixel can be summed to the signal of the neighbouring pixel which is not a charge sharing event but a weighting potential cross-talk one. For this reason, the weighting potential cross-talk technique is applied before the charge sharing correction.

2.3 Characterization of the pixel spectrometric detector

In this Section we present the characterization of the spectrometric pixel detector. The parameters of the pulse processing developed will be adjusted in order to study the achievable performances of the detector. The characterization was performed at both low and high count rates under γ and X-rays, respectively. Low fluxes measurements were performed with the γ source of ^{57}Co. High fluxes measurements were performed with a Yxlon MGC401 and 4,5 kW X-ray source operated between 120 kV and 160 kV.

2.3.1 Transient Signals

The performances of the 16-pixel matrix detector are based on the achievable energy resolution and dead-time of the entire system. The digitized signals processed on the FPGA comes from the CSA and they are digitized by the ADC. Fig. 2.16

represents the transient signal at the output of the CSA. The pulse was acquired with a γ-source of ^{57}Co.

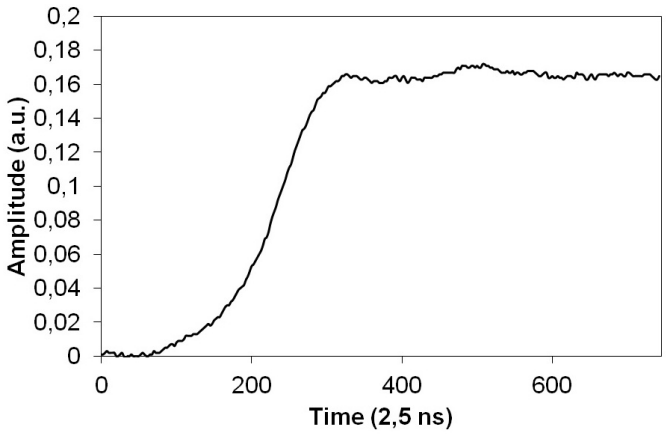

Figure 2.16: Output signals of the CSA when an γ particle interacts in the detector.

The signal is characterized by a rise time of 41 ns and by a long decay time. In order to convert the long exponential tail of the CSA output the two programmable shaper can be applied to these signals. Fig. 2.17 represents the output of the two presented shaper applied to the output of the CSA.

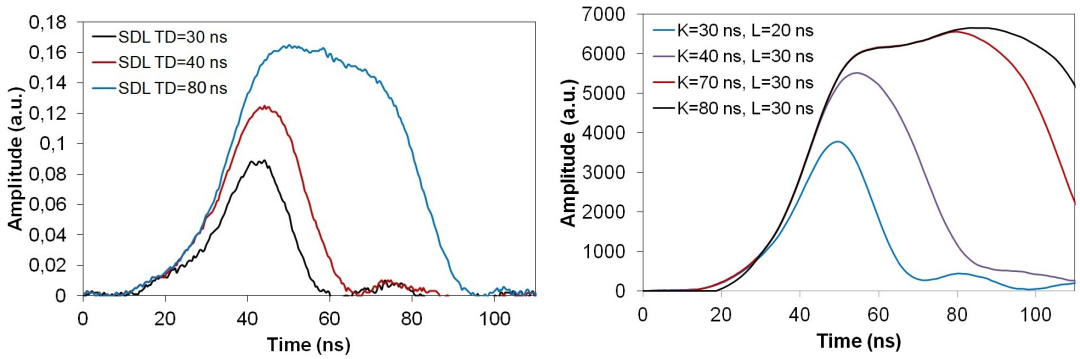

Figure 2.17: (Left) Output signals of the SDL at three different values of T_D.(Right) Output signals of the trapezoidal filter at four different couple of values of K and L.

It is possible to notice that when the shaping time is shorter than the rise-time of the CSA output we do not collect all the charges and thus we have ballistic deficit. The result is a smaller pulse amplitude compared to the pulses when we have a complete charge collection.

In order to evaluate the performances achievable in term of energy resolution and dead-time, in what follows we are going to discuss the behaviour of the system in different configurations.

2.3.2 Energy resolution

The energy resolution is the photo-peak energy dispersion divided by the energy of the photo-peak. It is defined as:

$$R_{energy} = \frac{FWHM(E)}{E} \tag{2.8}$$

In which FWHM is the full width at half maximum of the peak corresponding to the total deposition of the radiation energy in the detector and E is the energy of the interacting radiation. A γ-source of ^{57}Co, with a total count rate of ∼100 c/s, was used to characterize the spectrometric performances of the CdTe detector coupled with the 16-channel electronic setup. The bias voltage set was set to 1000 V, in order to ensure a good charge collection efficiency. The FWHM and the position of the photoelectric peaks are estimated with a Gaussian fit. The energy resolution achievable was measured with three different shaper configurations.

Energy resolution without pre-filtering and SDL

In this configuration the signals from the CSA are directly processed by the SDL algorithm. We applied different values of shaping time in order to investigate the influence on the energy resolution. Fig. 2.18 represents the pulse height spectra obtained.

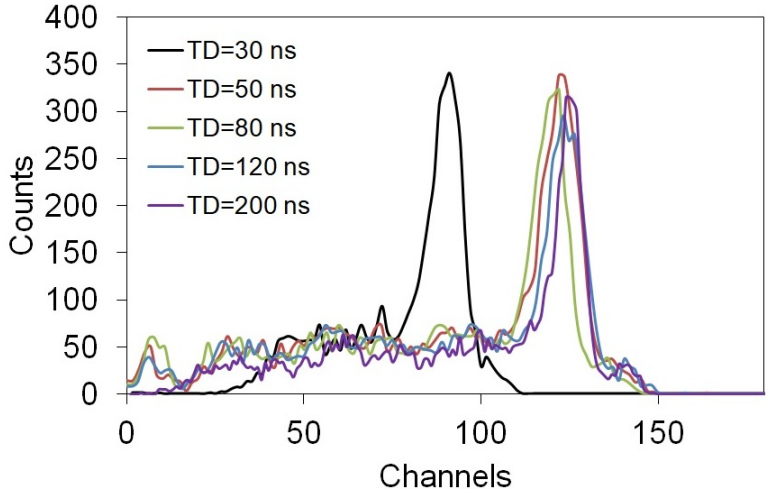

Figure 2.18: Pulse height spectra obtained with a SDL characterized by different values of T_D.

The energy resolution measured with different shaping times is summarized in Tab. 2.1. The value of the FWHM, the R(%) and the position of the photoelectric peaks are reported for the different T_D.

T_D (ns)	30	50	80	120	200
Peak position (at 122 keV)	86	122	121	122	122
FWHM (keV)	14,1	12,8	11,6	10,9	10,7
R (%)	11,6	10,5	9,5	8,9	8,8

Table 2.1: Values of the FWHM, the R(%) and peak position of the main photoelectric peak of the γ-source of ^{57}Co.

The results obtained with this first test show that the energy resolution improves when bigger delay lines are applied. The degradation of the energy resolution when a short delay line is used (T_D=30 ns) is due to an increase of the FWHM of the photoelectric peak and a decrease in amplitude due to the ballistic deficit. In fact, it is possible to notice that the position of the photoelectric peak when T_D=30 ns is smaller compared to the other peak positions.

Energy resolution with pre-filtering and SDL

To improve the energy resolution it is possible to implement a filter immediately after the CSA in order to increase the SNR, at the expense of a slower rise-time. An easy implementable filter on FPGA is the *Moving Average Filter*. The moving average filter is a special case of a regular FIR filter. Both filters have finite impulse responses but the moving average filter uses a sequence of 1 as coefficients, while the FIR filter coefficients are designed based on the filter specifications. The choice of the length of the temporal window of the moving average filter states the bandwidth of the filter. The moving average of streaming data is computed with a finite sliding window (N):

$$MA = \frac{x(n) + x(n-1) + \cdot\ \cdot\ \cdot\ \cdot + x(n-N)}{N} \tag{2.9}$$

The value of N is variable and we decided to analyse the performances reached with two different filter, one with a cut-off frequency of 50 MHz (N=2) and one of 20 MHz (N=5). Fig. 2.19 represents the effect that the pre-filter has on the signal form the CSA. We can measure the rise-time obtained with the two pre-filter proposed. We find a rise-time of 56 ns with a 50 MHz filter and 93 ns with a 20 MHz filter.

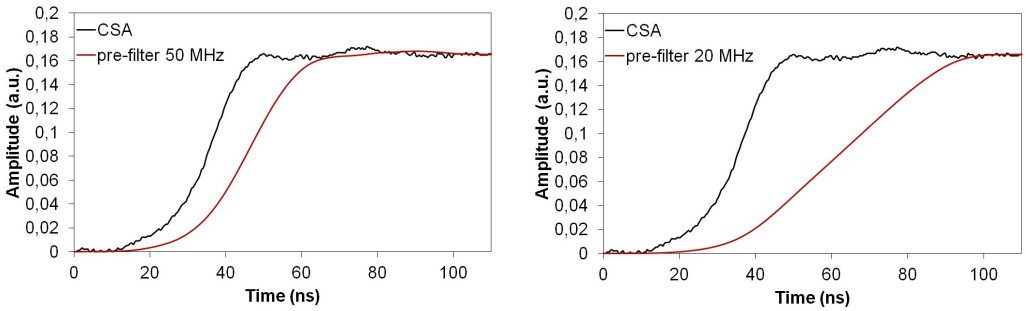

Figure 2.19: Effect of the pre-filter at 50 MHz (left) and 20 MHz (right) on the signal from the CSA.

The filter with a cut-off frequency at 50 MHz was tested first. The signals are then processed by the classical SDL with different shaping times. Fig. 2.20 represents the pulse height spectra obtained.

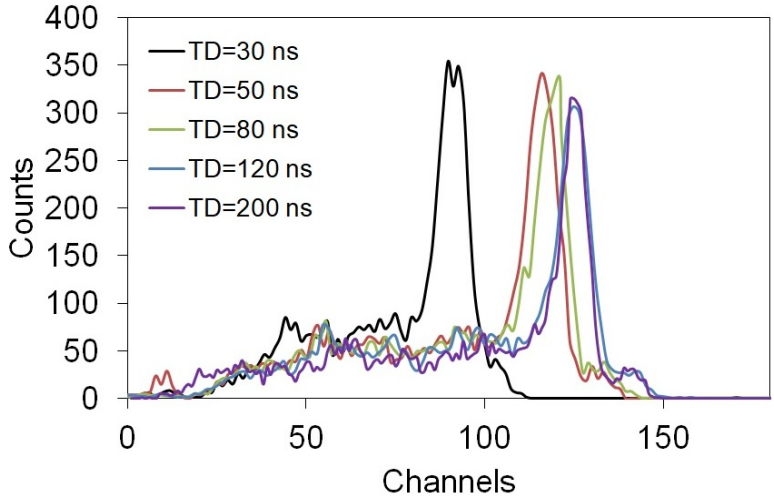

Figure 2.20: Pulse height spectra obtained with a SDL characterized by different values of T_D for the 50 MHz filter.

The value of the FWHM, the R(%) and the position of the photoelectric peaks at different values of T_D are summarized in Tab. 2.2.

T_D (ns)	30	50	80	120	200
Peak position (at 122 keV)	84	116	121	122	122
FWHM (keV)	14,2	11,6	10,3	9,8	9,7
R (%)	11,7	9,5	8,4	8	7,9

Table 2.2: Values of the FWHM, the R(%) and peak position of the main photoelectric peak of the γ-source of ^{57}Co for the 50 MHz filter.

The effect of the implemented filter is visible on the slight improvement on the

energy resolution. However, the energy resolution is slightly worsened at T_D=30 ns because the effect of the filter is to increase the rise-time with a consequent increase of the ballistic deficit.

The same measurements were carried out with a moving average filter with a cut-off frequency of 20 MHz. Fig. 2.20 represents the pulse height spectra obtained with different shaping times.

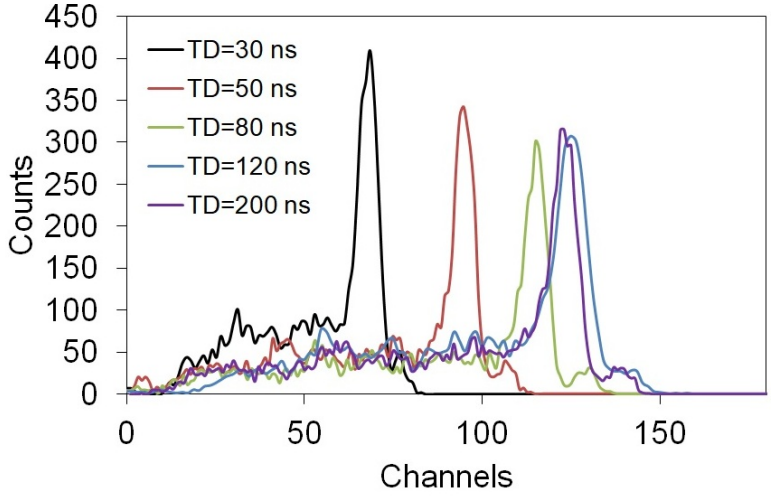

Figure 2.21: Pulse height spectra obtained with a SDL characterized by different values of T_D for the 20 MHz filter.

The energy resolution obtained with different shaping times is summarized in Tab. 2.3. The value of the FWHM and the position of the photoelectric peak are reported at different values of T_D.

T_D (ns)	30	50	80	120	200
Peak position (at 122 keV)	59	96	115	122	121
FWHM (keV)	12,5	8,4	7,9	7,4	7,3
R (%)	10,2	6,8	6,4	6	5,9

Table 2.3: Values of the FWHM and peak position of the main photoelectric peak of the γ-source of ^{57}Co for the 20 MHz filter.

With the use of this filter the improvement on the energy resolution is significant. It is possible to notice the increase of the ballistic deficit with the shift of the photoelectric peak of the pulse height spectra performed with T_D=30/50/80 ns. The saturation of the peak position is reached for T_D=120 ns. This means that the rise time of the signals treated by the SDL is bigger than 80 ns and shorter than 120 ns, i.e. 93 ns.

Energy resolution with trapezoidal filter

Another possible way of processing the signal directly from the CSA is to implement a shaper working as a filter. In the previous Section we presented the trapezoidal filter, a recursive algorithm able to convert the long exponential tale of the signals from the CSA in shorter symmetric pulses. We saw that this algorithm is characterized by two parameters, K and L (Eq. 2.2). These values are similar to the T_D of the classical SDL. We test this algorithm with two different couple of K and L. Fig. 2.22 represents the pulse height spectra obtained.

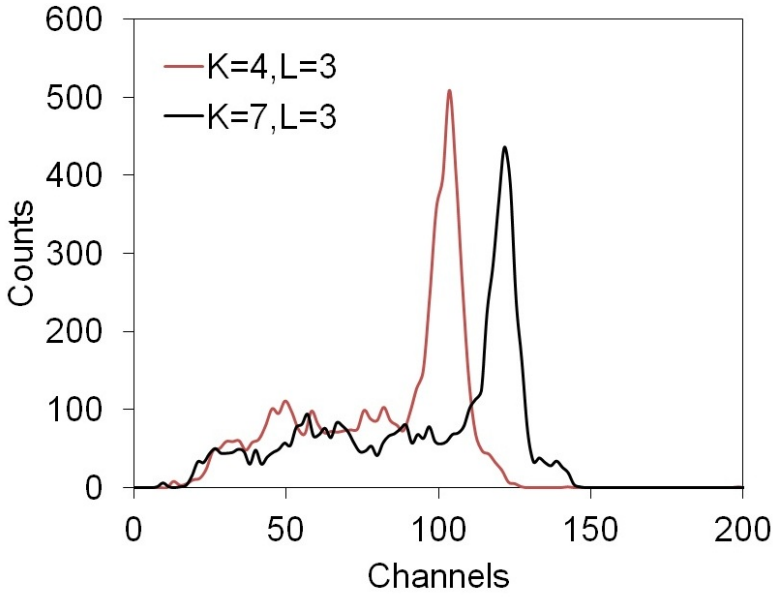

Figure 2.22: Pulse height spectra obtained with a trapezoidal filter characterized by two different couple of value of K and L.

The different position of the photoelectric peak means that K=4 and L=3 is a condition in which we have ballistic deficit. The FWHM of the peaks are equal to 6,8% (8,4 keV) if K=4, L=3 and 6,3% (7,8 keV) is K=7, L=3. The use of the trapezoidal filter immediately after the CSA provides a value of the energy resolution comparable with the SDL and with a 20 MHz pre-filtering.

2.3.3 Dead-time

As it has been done for the energy resolution, the dead-time of the system was measured for the three shaper configurations. The dead-time measures the capability of the electronic to separate two successive pulses, and to calculate the amplitudes and store them in the energy histogram. The value of dead-time depends on the shaping time used for the particular shaping algorithm. An X-ray source was used

for these measurements. The X-ray tube voltage was set to 150 kV and the current tube varied from 0,1 mA to 8 mA. A 0,8 mm filter of Tungsten was superposed to the beam. In this way it is possible to visualize the energy resolution. Fig. 2.23 represents a typical pulse height spectrum obtained with the SDL characterized by T_D=50 ns at different count rates.

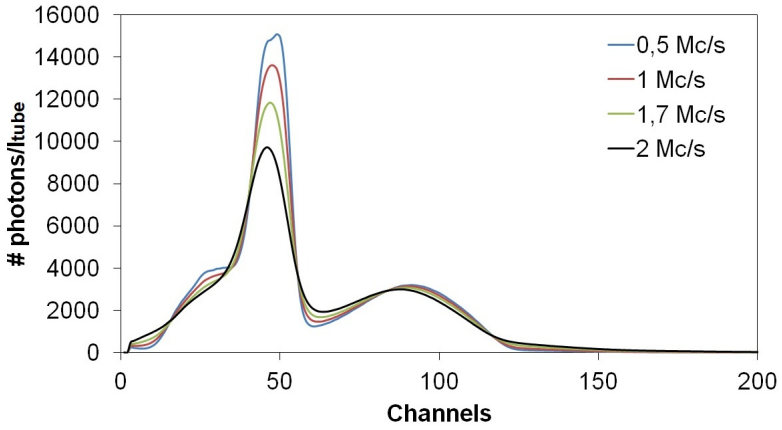

Figure 2.23: Pulse height spectra from 150 kV X-ray source obtained with the CdTe at different count rates with T_D=50 ns.

Dead-time without pre-filtering and SDL

The first test was performed in the configuration without any data filtering. The output from the CSA is digitized and directly processed by the SDL on the FPGA. The output count rate was measured at different currents and shaping times T_D. Fig. 2.24 represents the output count rate of the detector as a function of the tube current and T_D.

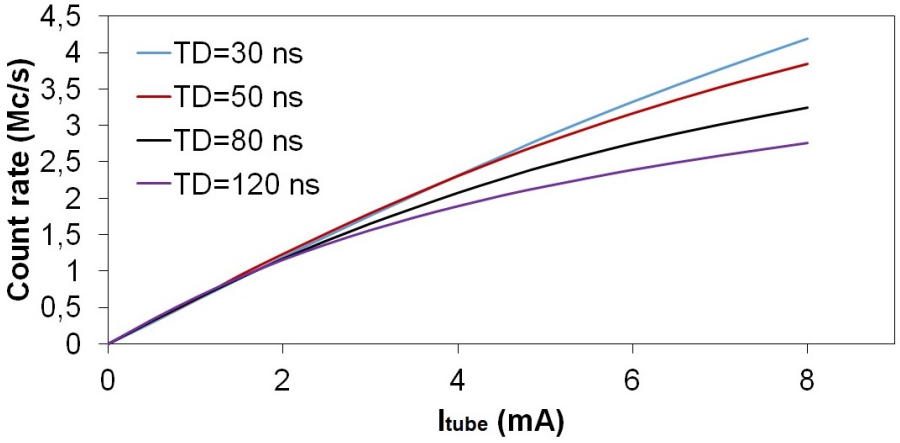

Figure 2.24: Output count rate versus applied current, measured with 120 kV X-rays.

Curves are relatively linear for count rates up to 1,5 Mc/s. At high fluxes, the count rate deviates from a linear behaviour because of pile-up. The output count rate was measured at different shaping times and with different tube currents. The experimental data were then fitted with the classical non-paralyzable model [17]:

$$m = \frac{n}{1 + n \cdot \tau} \tag{2.10}$$

Where m is the measured count rate, n is the input count rate, proportional to the tube current and τ is the system dead-time. The value of the dead-time for each delay line applied is reported in Tab. 2.4.

T_D (ns)	30	50	80	120
Dead-time (ns)	35	58	106	142

Table 2.4: Values of the measured dead-time.

This result is achieved thanks to our trigger algorithm based on the derivative of the SDL signals, able to separate two successive pulses as longer as a negative value of the first derivative is detected. Thus the dead-time is slightly higher than the peaking time [10].

Dead-time with pre-filtering and SDL

The second configuration considered is with a pre-filter stage with a moving average filter characterized by a cut-off frequency of 20 MHz. The output count rate was measured at different currents and shaping times of the shaping circuit. Fig. 2.25 represents the output count rate of the detector as a function of the tube current and the shaping time.

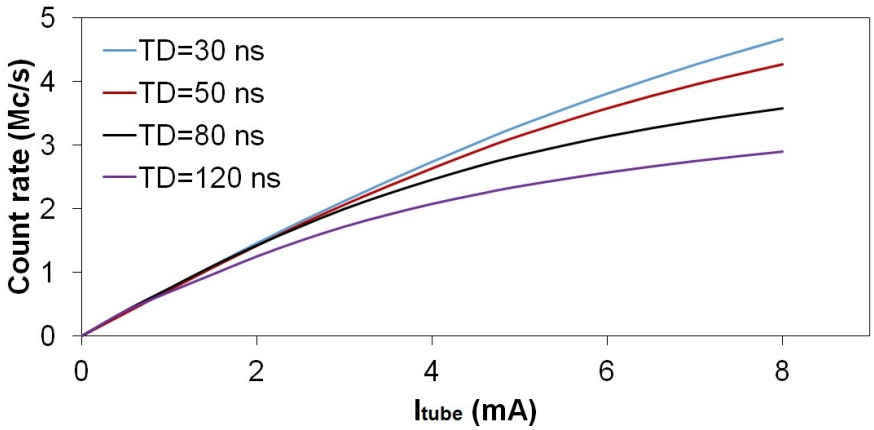

Figure 2.25: Output count rate versus applied current, measured with 120 kV X-rays.

The value of the dead-time for each delay line applied is reported in Tab. 2.5. These results show that with the pre-filter stage the dead-time of the detector for a given value of T_D slightly increases.

T_D (ns)	30	50	80	120
Dead-time (ns)	45	63	110	152

Table 2.5: Values of the measured dead-time obtained with a pre-filter of 20 MHz.

Dead-time with trapezoidal filter

Dead-time measurements were also performed with the trapezoidal filter. Signals from the CSA are directly processed by the recursive algorithm. This time the shaping time is characterized by the two parameters K and L. As we performed for the energy resolution with the γ source, the two couple of values chosen are K=7, L=3 and K=4,L=3. The first couple correspond to a long shaping time and the second to a short one. Fig. 2.26 represents the output count rate of the detector as a function of the tube current and the value of (K,L).

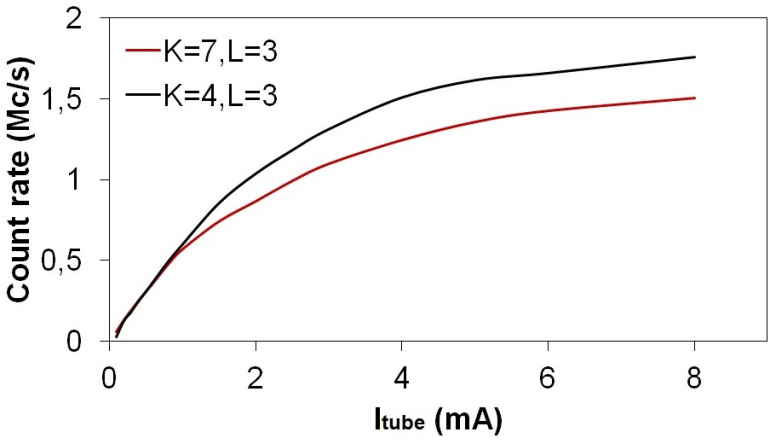

Figure 2.26: Output count rate versus applied current, measured with 120 kV X-rays.

The important result we immediately notice from the curves is that the linearity of the output count rate with the current tube is satisfied only for values up to 0,5 Mc/s. Tab. 2.6 summarized the value of the measured dead-time for the two different configurations of the trapezoidal filter.

K,L (ns)	(40,30)	(70,30)
Dead-time (ns)	97	185

Table 2.6: Values of the measured dead-time obtained with the trapezoidal filter.

Form the results obtained when the trapezoidal filter is used is a significant increase of the dead-time despite the good energy resolution measured. For this reason the trapezoidal filter it is not recommend for high-fluxes application where the count rate is bigger than 1 Mc/s.

2.4 Conclusion and discussions

In this Chapter we presented the experimental setup and the detector used in this work. We described in detail the readout electronic and the digital pulse processing algorithms. Finally we characterized the detector in terms of the energy resolution and dead-time. The characterization was performed with three different configurations of shaper. At first we analysed the readout electronic with a SDL, processing the signals directly after the CSA. In the second configuration we have implemented a moving average per-filter stage on FPGA at the output of the CSA. Finally we have compared the performances with a trapezoidal filter. In this last case signals from the CSA are directly processed by the shaping filter. The compromise of SNR, good energy resolution and short dead-time is not satisfied by this last choice. We demonstrated that the trapezoidal filter has interesting performances in term of energy resolution, comparable to the SDL preceded by the pre-filtering stage, but with an important degradation of the system dead-time.

	T_D / K,L (ns)	R (%)	Dead-time (ns)
Without pre-filter	30	11,6	35
	50	10,5	58
	80	9,5	106
	120	8,9	142
	200	8,8	n.m.
With pre-filter (20 MHz)	30	10,2	45
	50	6,8	63
	80	6,4	110
	120	6	152
	200	5,9	n.m.
Trapezoidal filter	40,30	6,8	97
	70,30	6,3	185

Table 2.7: Summary of the results obtained.

Tab. 3.4 gives a short summary of the obtained results with three of the presented shaper configurations. We decided to report the three most significant configurations

of the four presented, because the one with the pre-filter stage performed with a moving average at 50 MHz does not contribute significantly compared to the version of the data processing without a pre-filter stage. The comparison among the three different configurations underlines important aspects. First we have seen that the use of the SDL for signals directly after the CSA compared to the trapezoidal filter permits to obtain shorter values of the dead-time but with an important degradation of the energy resolution. If a pre-filter stage is implemented, the improvement on the energy resolution is significant and the use of the SDL in terms of energy resolution is comparable to the trapezoidal filter. This latter is characterized by a dead-time that is significantly high compared to the achieved in other configurations. On the contrary, the SDL shaper with a 20 MHz filter improves the energy resolution, with only a small increase of the dead time.

Chapter 3

Instability of the detector response

The aim of this Chapter is to explain the mechanism of the instability of the detector response over time. The presence of defects in the semiconductor leads to trapping phenomena which can create a fixed space charge in the detector over time with a consequent modification of the profile of the electrical field. We have shown that the use of certain configurations in which we obtain a good compromise of energy resolution and dead-time, lead us to work in ballistic deficit regime. In this chapter we will show how variations in the electric field profile cause instability of the detector response due to the change in the amplitude of the ballistic deficit.

3.1 Observation of the instability

In several applications such as luggage control, non-destructive test (NDT), medical imaging and computed tomography (CT) it is necessary to use configurations in which we accept to work in ballistic deficit domain in order to obtain good performances in terms of energy resolution and dead-time for very high fluxes. The shaping time used for high flux spectrometry is shorter than the necessary time for the charge collection. We observed that in this configuration the detector response is not stable over time and during the first 2 hours of operation.

The phenomenon of the instability of the detector response is observed on the pulse height spectra obtained with a γ-source of ^{57}Co performed with a SDL shaper characterized by a T_D=50 ns. In order to observe the phenomenon two different tests were performed. A first measurement was performed during the first 2 hours after biasing the detector. The spectra were acquired every 2 minutes. After this first test the detectot was left biased for another 30 minutes and then a new acquisition sequence was carried out during the next two hours. Fig. 3.1 represents

the obtained pulse height spectra.

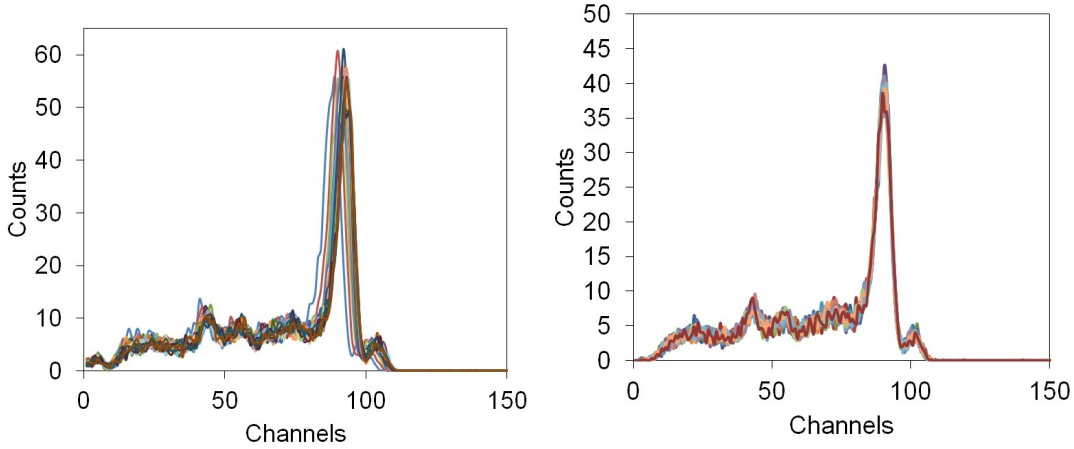

Figure 3.1: Spectra obtained with a CdTe detector (left) during the first two hour after biasing the detector and (right) when the detector was in its stable conditions.

Form the PHS obtained it is possible to notice that during the first two hours of operation the photoelectric peak shifts slowly to the right, showing that the conversion gain of the detector slightly increases. Two hours after biasing the detector the stability of the response is reached. This aspect is confirmed with the second acquisition performed when the detector was in its stable conditions. It is possible to evaluate the position of the spectra over time with a Gaussian fit performed on the main photoelectric peak at 122 keV. Fig. 3.2 represents the peak position over time normalized on the measured centroid of the last PHS of the acquisition.

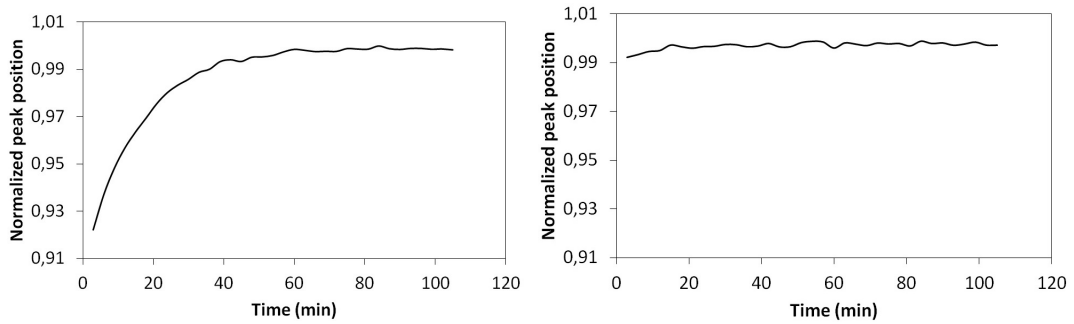

Figure 3.2: Normalized peak position over time of the PHS obtained with a shaping time of 50 ns during the unstable conditions of the detector (left) and for the stable one (right).

From the results obtained it is possible to notice that the phenomenon of the instability of the detector response is limited to a period of around 1 hour after biasing the detector. We can state that 2 hours after biasing the detector, the detector response is perfectly stable.

3.2 Origin of the instability

In order to explain the origin of these variations and shifts of the spectra, an analysis of the output signals from the CSA was performed. Fig. 3.3 represents the transient signal at the output of the CSA, measured with 5,156 Mev α particles from a ^{239}Pu radioactive source at different times of operation, immediately after switching on the bias voltage and during the 2 hours of operation. We also represented the variation of the rise-time deduced from these pulses.

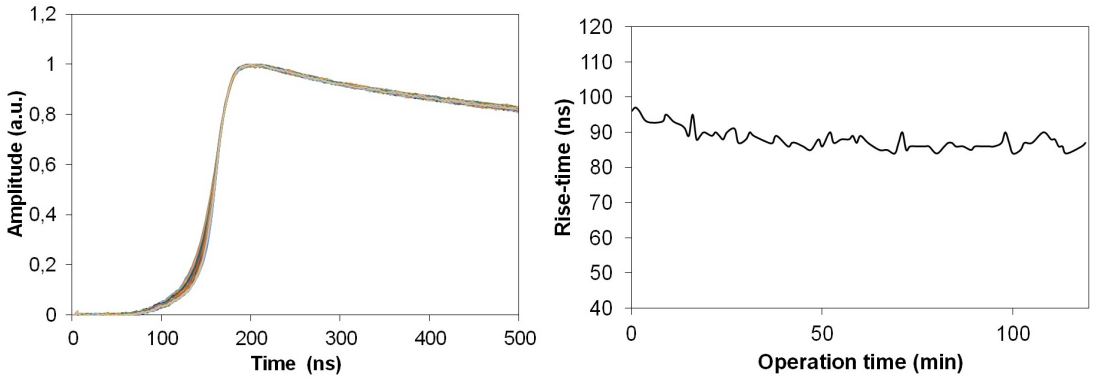

Figure 3.3: Output signals of the CSA when an α particle interacts in the detector (left) and the rise times of the signals during the whole operation time (right).

When we observe the transient signals at the output of the CSA, we notice that the amplitude of the signals at the output of the CSA is stable but the transient shape varies in time with a variable rise-time during the first two hours of operation. The rise-time, measured as the duration of the pulse from the 10% until its 90%, decreases regularly during the first hour of the detector operation, starting from 96 ns and reaching a value of 87 ns after approximately 60 minutes.

3.2.1 Ballistic deficit over time

The average rise-time of the signal at the input of the SDL is approximately 90 ns, but its exact value varies during all the operation time. Fig. 3.4 represents the output of the SDL characterized by a delay smaller and bigger than the rise time of the signals from the CSA immediately after biasing the detector and after 2 hours of operation.

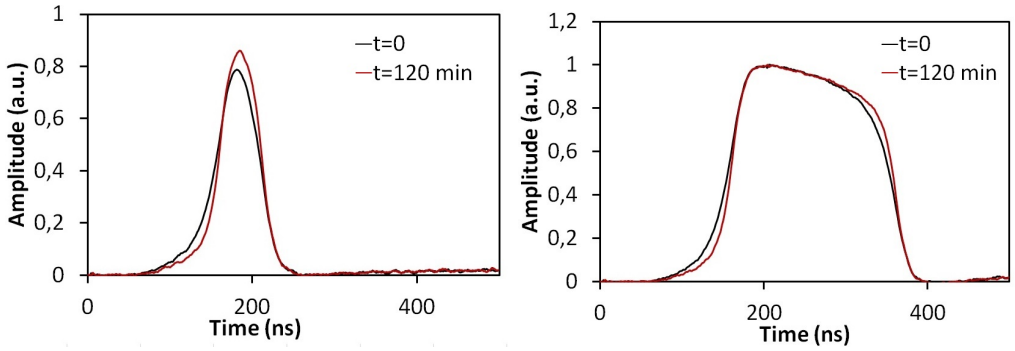

Figure 3.4: Output of the SDL with a delay of 50 ns (left) and 150 ns (right) for an induced signal by an α particle immediately after biasing the detector (black) and after 120 minutes (red).

From the output signal of the SDL with a delay of 50 ns we observe that the ballistic deficit is sensitive to the CSA signals rise-time variations. The result is a small drift of the signal amplitude from the shaping circuit. In order to avoid this effect, it is possible to use a SDL with a delay longer (150 ns) than the rise time of the CSA signals. In this case the ballistic deficit is negligible and we measure the correct total charge released in the detector, providing a stable behaviour over time. On the other hand, we demonstrated that the use of a long shaping time causes an important degradation on the dead-time and thus impossible to use in high-fluxes application where the phenomenon of pile-up is important.

3.2.2 Simulation of the instability

The variations of the transient signal at the output of the CSA indicates that the electrical field profile varies over time. The variations of the electrical field profile over time are due to the modification of the space charge in the detector material.

We have developed a model for the estimation of the transient signal as a function of the space charge in the detector. The Gauss-Maxwell equation gives a relation between the electrical field and the space charge:

$$div(\overrightarrow{E}) = \frac{\rho(x)}{\epsilon} \tag{3.1}$$

In addition to this, we calculated the position of the electron cloud from the transport equation, neglecting the effect of the spread due to the diffusion and the Coulomb repulsion:

$$\frac{dx(t)}{dt} = \mu \cdot E(x) \tag{3.2}$$

Eq. 3.1 and 3.2 allow us to compute the position *x(t)* of the electron cloud as a function of time *t*. The induced signal on the pixel electrode is calculated though the Ramo theorem:

$$q_{ind}(t) = q_0 \cdot V_P(x(t)) \tag{3.3}$$

Where V_P is the weighting potential of the pixel electrode and *x(t)* is the solution of the Eq. 3.2. From these equations we can calculate the induced charge as a function of the charge density distribution, $\rho(x)$. Fig. 3.5 (left) shows the charge induced for three different values of the space charge densities. In order to compare these simulated signals with the experimental ones acquired with the α particles, we performed a convolution between the induced current and the impulse response of the CSA. This latter is measured by injecting a very short pulse current (of some ns) on the CSA input. Fig. 3.5 (right) shows the simulated signal for a uniform positive space charge distribution. In this case, the profile of the electrical field varies linearly with the detector depth [86]. We observed that the transit time increase from 90 ns for a zero charge density to 100 ns for a value of 0,01 C/m^3.

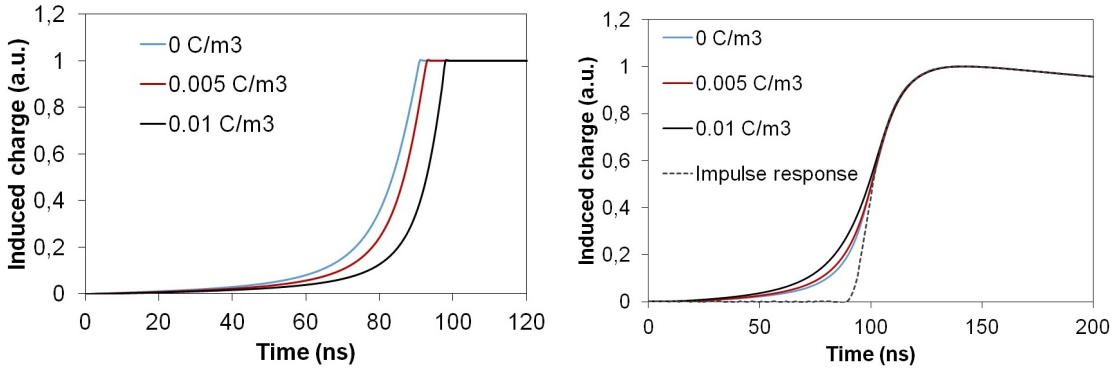

Figure 3.5: Induce charge on the pixel electrode (left) and simulated transient signals from the CSA for 3 different ρ (right). The dotted line represents the impulse response of the CSA.

Assuming a uniform space charge, we compare the pulses generated by our model to the pulses measured with α particles, in order to compute the charge density which fits the observed transient signals. Fig. 3.6 represents the performed fit on the transient signals. By fitting the simulated pulse to the measurements, we deduce the space charge density as a function of time.

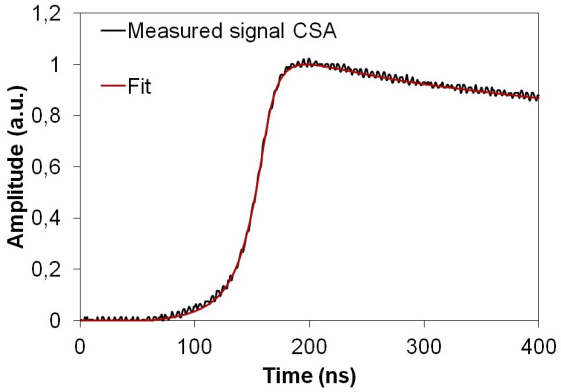

Figure 3.6: Example of the performed fit on the measured pulse with α particles for the computation of the charge density.

Fig. 3.7 represents the fixed space charge as a function of time deduced with our model from the measurements done with the α particles.

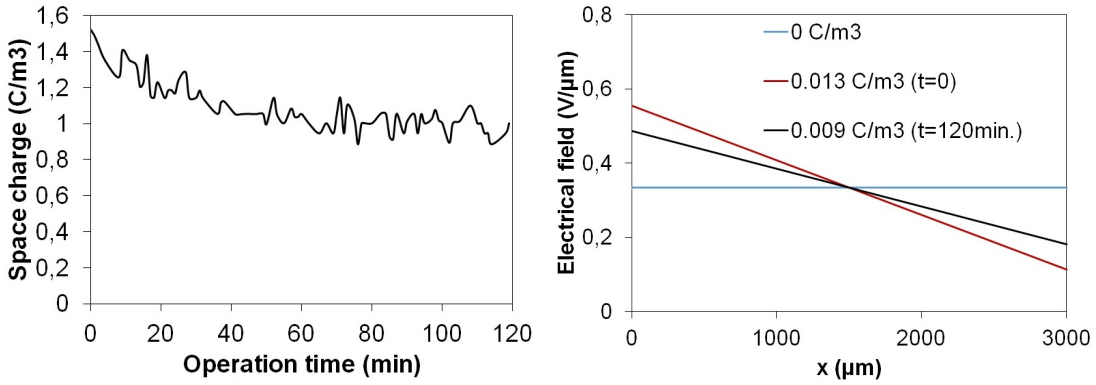

Figure 3.7: (Left) Fixed charge density during the operation time of the detector from α particles. (Right) Profile of the electrical field corresponding to the estimated space charge at t=0 minutes and t=120 minutes of operation.

The charge density is of the order of 0,013 C/m^3 immediately after switching on the bias voltage of the detector. After approximately 1 hour of operation, this value decrease and becomes stable around the value of 0,009 C/m^3. As a result, the slope of the electrical field profile, significant at the beginning, decrease slowly, leading to faster transient signals.

Tab. 3.1 represents a summary of the results obtained from the simulation of the instability and clearly underlines how the ballistic deficit is related to the space charge density variation over time.

T (min)	ρ (C/m^3)	τ_{rise} (ns)	Ballistic deficit
0	0,013	96	0,22
120	0,009	87	0,15

Table 3.1: Summary of the obtained results of the simulation.

3.3 Parametric study

The stability of the detector response depends on different detector settings. In this Section we will investigate the detector response over time for different shaping times used for three different shaper configurations. At first, we will investigated the response of the detector when the signals from the CSA are directly processed by the SDL. Then when these signals are processed by the SDL after a pre-filter stage with a cut-off frequency of 20 MHz. Finally when the signals are processed by a trapezoidal filter. The response is investigated at different shaping times. The measurements were performed with a γ-source of ^{57}Co during 2 hours of operation with a total count rate of 100 c/s.

3.3.1 SDL without pre-filtering

This first test was done with a real-time processing of the CSA signals directly with the classical SDL on the FPGA. Fig. 3.8 represents the position of the main photoelectric peaks (122 keV) during the operation time for different delay lines. The estimation of the peak position was performed with a Gaussian fit.

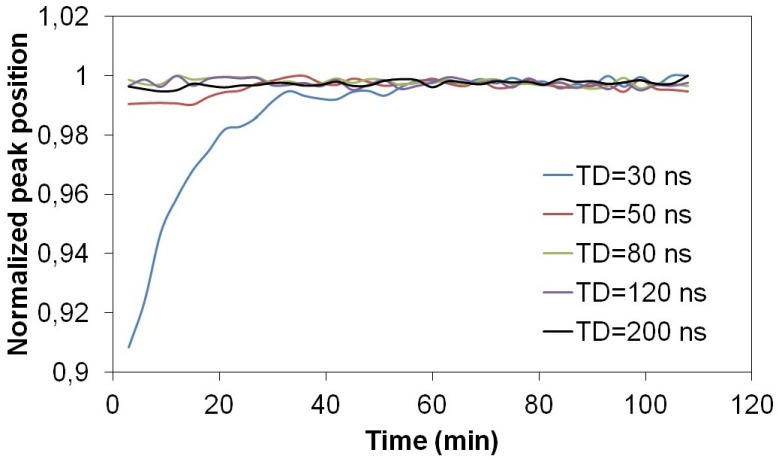

Figure 3.8: Normalized peak position over time at different shaping time during the operation time of the detector.

The result obtained shows that there is a drift of the photoelectric peaks when the

shaping time is equal to 30 ns. A slight shift of the peak position is also observed with a shaping time of 50 ns during the first 20 minutes. In the other cases we find a stable response over time. The estimated variation of the ballistic deficit when T_D=30 ns is of 9% after biasing the detector and 1% for T_D=50 ns. We observe that the stability of the response is reached after 50 minutes of operation. In other cases we do not have ballistic deficit because the SDL is able to collect all the charges, since the shaping time is bigger than the rise-time of the signals from the CSA. In this case the stability is reached immediately after biasing the detector.

3.3.2 SDL with pre-filtering

This second test was done with a real-time processing of the CSA signal filtered by a 20 MHz moving average filter and then shaped by the SDL. The entire process in performed in the FPGA.

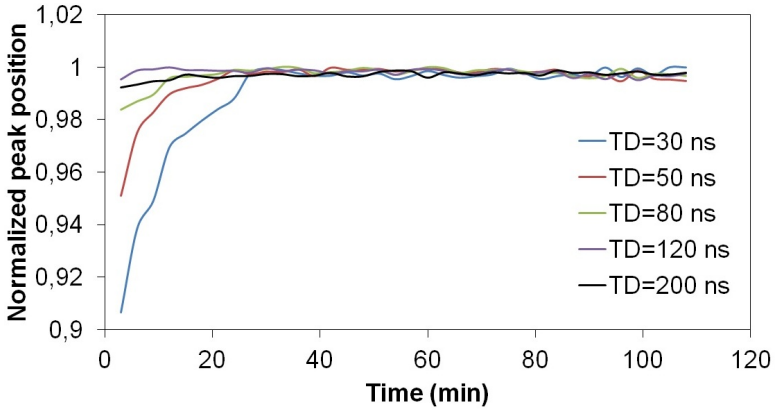

Figure 3.9: Normalized peak position over time at different shaping times during the operation time of the detector.

Fig. 3.9 represents the position of the main photoelectric peaks (122 keV) during the operation time for different shaping times. The result obtained shows that now we have the drift of the photoelectric peaks even for longer shaping times, i.e. 30 ns, 50 ns and 80 ns. For 30 ns the variation of the ballistic deficit is of the order of 10%, while for 50 ns 5% and finally for 80 ns we find a variation of 2%. With these results we can notice that the variation of the ballistic deficit over time is more sensitive with short shaping times and less for longer one. Moreover, there is also a slight difference in time for reaching the stability. With T_D=30 ns the detector is stable 40 minutes after biasing the voltage. For T_D=50 ns the detector is stable in 35 minutes after biasing the voltage and for T_D=120 ns the stability is reached some minutes after biasing the detector. The transient signals measured in Chapter 2 show that the 20 MHz filter increases the ballistic deficit. In fact,

without any pre-filter we obtain a stable response of the detector over time only for the delays longer than the peaking time (41 ns). When we use a 20 MHz filter, we notice an increase of the value of the rise time (around 90 ns). The only value of T_D for which we can collect all the charges and thus we do not have ballistic deficit is 120 ns. For all the other values we do have a ballistic deficit and thus an unstable detector response over time.

3.3.3 Trapezoidal filter

This last test was done with a real-time processing on the FPGA where the trapezoidal filter processed directly the signals from the CSA. In this case two couple of parameter K and L were used, i.e. K=7, L=3 and K=4, L=3. Fig. 3.10 represents the position of the main photoelectric peaks (122 keV) during the operation time.

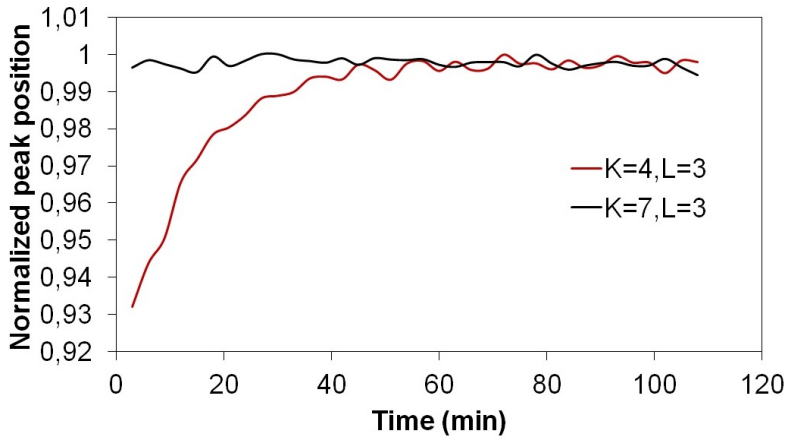

Figure 3.10: Normalized peak position over time at different shaping times during the operation time of the detector.

The result obtained shows that we have a drift of the photoelectric peaks for the shorter shaping time, i.e. K=4 and L=3. We observed a drift of the photoelectric peak of the 7% after biasing the detector. The stable condition is reached 50 minutes after biasing it. In the other case (K=7 and L=3) the shaper measures all the charges and we do not have ballistic deficit.

3.4 Influence of polarization voltage and detector geometry

In this Section we are going to discuss on some possible approaches to adopt in order to reduce or eliminate the effect of the polarization inside the detector.

3.4.1 Polarization voltage

The model of the instability we presented above can be used to predict the detector behaviour at different geometries. The Time Of Flight (TOF) measurement done with the α particles and the model we developed, show that the drift of the conversion gain is due to the transitory signal variation caused by the modifications of the electrical field profile. If we use a shaping time T_D of the SDL that is longer than the rise time of the signals from the CSA, we noticed that the amplitude of the collected signal is no more sensitive to these variations. The main drawback of using such a shaping time is a significant degradation of the detector dead-time and thus a degradation of the performances of the response when the count rate is elevate. When the application requires a use of the detector under high-flux, a possible solution is to reduce the transient time of the signals from the CSA. In order to perform this, it is necessary to increase the polarisation voltage of the detector. In our case the thickness of the detector is of 3 mm, and to obtain a transit time of 50 ns it is necessary to apply a polarization voltage of 2000 V. We have observed that the maximum polarization voltage we can apply to the detector is of the order of 1200 V. Above this value the electronic noise becomes significant.

3.4.2 Geometry of the pixel

Another possible solution is to reduce the thickness of the detector. This implies a decrease of the absorption of high energy photons. Another drawback of the detector thickness decreasing is that the small pixel effect will be modified. The weighting field, as we studied in the previous Chapter, is proportionally less concentrated near the pixel and the detector response is more sensitive to the depth of the interaction when it is irradiated on the side of the common cathode.

The size of the pixel has an important impact on the stability of the detector response. In fact, it does not modify the transit time of the signals but it is responsible of a ballistic deficit decreasing. If we ignore the bandwidth of the CSA, the signal from the SDL is:

$$V_{SDL} = V_{CSA}(t) - V_{CSA}(t - T_D) \tag{3.4}$$

Once we have the weighting potential convex shape, the maximum is achieved when the electron cloud reaches the pixel electrode for a time $t = t_{transit}$. The ballistic deficit is given by the value of weighting field in the position where the electron cloud is 50 ns before it reaches the collecting pixel. For a 3 mm detector

polarized at 1000 V, this correspond more or less to the middle of the pixel. For this particular position, Fig. 3.11 shows that the weighting field is weaker when the pixel size is smaller. This effect is the result of a slighter ballistic deficit and thus a less strong sensitivity to the electrical field profile changes.

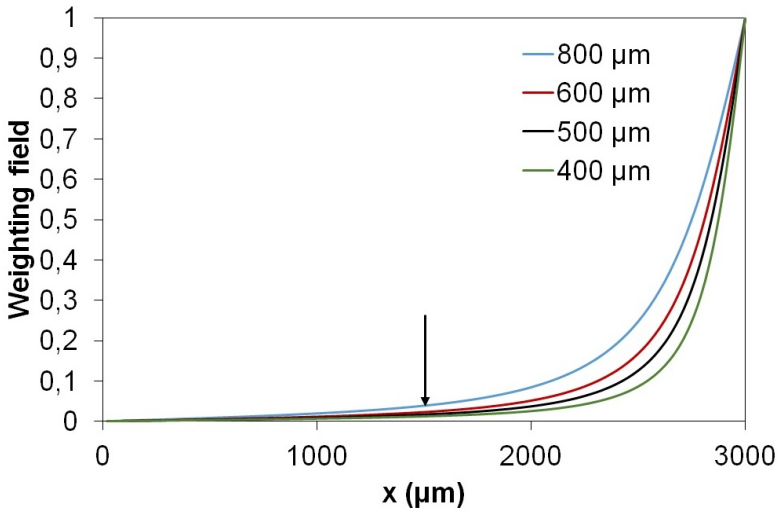

Figure 3.11: Weighting field profile for different pixel sizes. The arrow shows the position of the electron cloud ∼50 ns before its complete collection.

The model presented in the previous Section can predict the conversion gain variations for different pixel geometries, assuming that the space charge varies in the same way. We can compute the induced signals for different charge density and then deduce the transient signals from the CSA and finally from the SDL circuit. Fig. 3.12 shows the result of this simulation for different thickness (from 1,5 to 3 mm) and different pixel pitch (from 400 to 800 μm) of the detector.

From this results we can notice that the variation of the charge density has more impact on the amplitude of the signals from the SDL when the detector is thicker. Once we pass from 3 mm to 2 mm the effect is significantly reduced, i.e. the amplitude variation decreases from 5% to 1%. For 1,5 mm the effect of the space charge density variation is negligible. Reducing the pixel pitch has also the effect of decreasing the amplitude of the conversion gain drift, but it does not eliminate it completely.

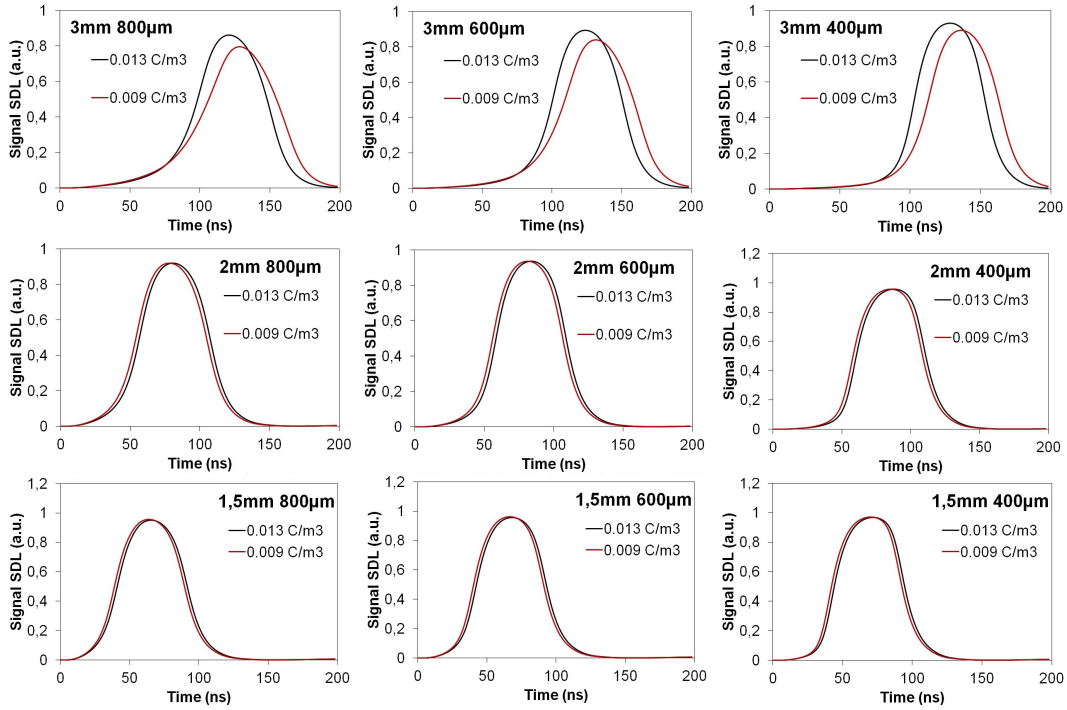

Figure 3.12: Output signals from the SDL for uniform charge densities (0,013 and 0,009 C/m^3) simulated for different geometries.

Tab . 3.2 summarizes the results obtained with the simulations.

	3 mm	2 mm	1,5 mm
800	7,5%	0,6%	0,2%
600	5,9%	0,5%	0,0%
500	5,1%	0,5%	0,0%
400	4,1%	0,4%	0,0%

Table 3.2: Conversion gain variation when the charge density varies from 0,013 C/m^3 to 0,009 C/m^3.

It is important to notice that these effect were obtained with the assumption that the space charge distribution always varies in the same way, regardless of the geometry of the detector and the measurement conditions (voltage, temperature). It is possible that different detectors with different polarization voltage at different temperatures, present different behaviours.

3.5 Summary

Section 3.3 shows that the detector geometry and settings have an impact on the stability of the response. Tab. 3.3 summarizes the different parameters that can

be used to improve the stability and the consequent impact they have on the spectrometric performances.

Optimization parameters	**Impact on spectrometric performances**
Increase the polarization voltage	Increase of the dark current
Decrease of the thickness	Less sensitivity to high energies
Decrease the pitch pixel	Increase of charge sharing
Increase of T_D of the SDL	Increase of the dead time
Increase the bandwidth of the readout circuit	Increse of the noise
Wait for the detector to be stable	Strong operational constraint

Table 3.3: Variable parameters having an impact on the detector stability versus effects on the detector performances.

Tab. 3.3 can help us to chose the optimal configuration of the detector in order to obtain stable responses. For example, for security applications we know that the X-ray flux is ∼3-5·10^6 X·$mm^{-2} \cdot s^{-1}$. For a pixel of 800 μm and a thickness of 3 mm, we have seen that the transit time is ∼100 ns. With a SDL characterized by a T_D=50 ns, we already know that the detector will be unstable. Three different approaches can be applied:

- Decrease the thickness of the detector from 3 mm to 1,5 mm in order to have a transit time of the order of 50 ns, with the drawback of an important decrease of sensitivity to high energy photons.
- Work with a longer shaping time (e.g. 100 ns), with the drawback of a count loss due to the pile-up
- Work with a longer shaping time (e.g. 100 ns) and with a pixel pitch smaller, with the drawback of an increasing of the charge sharing effect.

It is clear that we can adjust the three parameters simultaneously in order to obtain a good compromise.

3.6 Conclusion and discussions

In this Chapter we have analysed in detail the phenomenon of the unstable response of the detector over time. We have demonstrated that the variations of the rise-time of the signals from the CSA are mainly due to the modification of the space charge distribution inside the detector material. This causes variations in the electrical

field profile over time.

Considering the results obtained in Chapter 2 together with the results obtained here, it is possible to summarize the performance of the spectrometric pixel detector in use (Tab. 3.4).

	T_D / K,L (ns)	R (%)	Dead-time (ns)	Stability
Without pre-filter	30	11,6	35	No
	50	10,5	58	Yes
	80	9,5	106	Yes
	120	8,9	142	Yes
	200	8,8	n.m	Yes
With pre-filter (20 MHz)	30	10,2	45	No
	50	6,8	63	No
	80	6,4	110	No
	120	6	152	Yes
	200	5,9	n.m	Yes
Trapezoidal filter	40,30	6,8	97	No
	70,30	6,3	185	Yes

Table 3.4: Summary of the results obtained.

There were studied three different shaping configurations. We demonstrated that in the first configuration considered, without a pre-filter stage, the measured dead-time is smaller compared to the other approaches proposed. Moreover, starting from a value of T_D=50 ns the detector response over time is stable during its operation period. On the other hand we observed that this approach is not optimized in terms of energy resolution. For this reason it is important to filter the signal from the CSA in order not to degrade the performances of the detector. The implemented filter is a moving average filter with a cut-off frequency at 20 MHz. The use of the filter implies an increase of the value of the rise time and thus of the ballistic deficit. With this configuration we observed that the stability of the detector response is reached only for shaping times longer than the collection time of the charges and the dead-time is slightly degraded. The important result with the use of this configuration is the improvement in terms of energy resolution for shaping times longer than 50 ns. For shorter shaping times (T_D=30 ns) the energy resolution with and without pre-filter after the CSA are almost the same. This means that this value of T_D is not optimal in terms of energy resolution. The last approach we wanted to test, required the use of a trapezoidal filter for the signal processing

of pulses from the CSA. The results we observed for this configuration are similar to the ones obtained in the configuration with a pre-filter of 20 MHz. The energy resolution measured is comparable to the energy resolution obtained for T_D=50 ns and T_D=120 ns. Moreover, the stability of the detector response is obtained only when the flat top of the trapezoidal shape is longer (K=70 ns and L=30 ns) than the collection of the charges. The important difference is that with the trapezoidal filter we degrade significantly the dead-time of the system with both the couple of values used of K and L. This last solution does not represent a good compromise for high flux applications where the phenomenon of pile-up is very important. In conclusion, this parametric study shows that it is difficult to find a shaper configuration that ensures both good spectrometric performance with high count rates and stable behaviour. The 50 ns SDL with a 20 MHz filter is a good compromise for high counting applications (above 1 Mc / s), but does not guarantee stable operation before one hour of operation.

We have also shown that the geometry of the detector (thickness, pixel pitch) has an influence on the stability of the detector. However, the current detector, when used in an optimal configuration for spectrometric measurements at high count rate, presents an unstable response in the first hours of operation. For this reason we developed a correction method which will be presented in the next Chapter.

Chapter 4

A real-time ballistic deficit correction method

The aim of this Chapter is to present the principle of the method developed during this thesis work in order to compensate the phenomenon of the ballistic deficit and thus achieve a stable response of the detector over time. In Chapter 3 we have demonstrated that the unstable detector response is due to the ballistic deficit variations over time, caused by the modification of the electrical field profile inside the detector material. When a shaping time long enough is used, the detector response is stable immediately after biasing the detector, because there is no ballistic deficit. However, such long shaping times imply a degradation of the dead-time (Chapter 2) with a significant loss on the output count rate under high-fluxes. In order to operate the detector at high count rate with a fast shaping circuit, we developed a real-time method for the correction of the ballistic deficit with the goal of compensating its variation over time and thus achieving a stable response of the detector during its operation time without losing on its performances. At the end of this Chapter an overview of the implementation of the method on FPGA will be given too.

4.1 Double Shaper for the Ballistic Deficit Compensation

The general idea of the proposed method is to estimate the ballistic deficit through the use of a double shaping circuit in order to compensate the ballistic deficit with a correction coefficient. The short shaping circuit measures the energy spectra at high fluxes with a reduced dead-time. The long shaping circuit measures the total collected charge in order to estimate the ballistic deficit of the fast shaping circuit.

By measuring the amplitude of the pulses of the two shaping circuits, we estimate a correction factor η defined by:

$$\eta = \frac{A_{short}}{A_{long}} = (1 - BD) \qquad with \qquad 0 < \eta < 1 \tag{4.1}$$

Where BD is the ballistic deficit, A_{short} and A_{long} represent the amplitudes of the fast and slow shaping circuits, respectively. By dividing the measured amplitude of the fast shaping circuit by η, we are able to compensate the loss due to the ballistic deficit. Eq. 4.2 represents this principle:

$$A_{corrected} = \frac{A_{short}}{\eta} \tag{4.2}$$

In summary, we operate a gain correction of the pulses obtained with the unstable fast shaping circuit. The spectrum obtained from these corrected pulse amplitudes will be in a position equivalent to that obtained with the slow shaper and thus stable over time. Fig. 4.1 represents the PHS obtained for a γ-source of ^{57}Co with whit a short shaping time characterized by T_D=50 ns and a long one with T_D=150 ns.

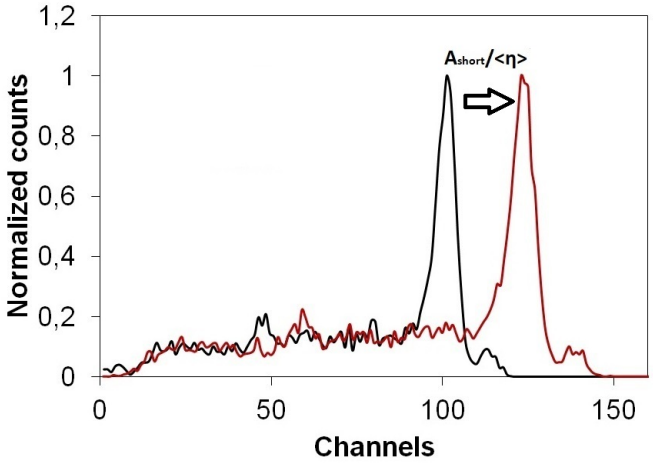

Figure 4.1: Pulse height spectra of the γ-source of ^{57}Co whit a short shaping time characterized by T_D=50 ns (black) and a long one with T_D=150 ns (red).

We can compare the correction factor $< \eta >$ to the ratio between the peak positions at 122 keV of the spectra obtained with T_D=50 ns and T_D=150 ns. With the two delay lines used we obtain a value of $peak_{50ns}/peak_{150ns} = 0,85$.

The efficacy of the compensation is limited by some important aspects affecting the correct measurement of the correction factor η. At first, the SNR of the pulses is not high enough for the measurement of η from a single event. The second

aspect is that the signals from the CSA can be affected by three phenomena which can introduce errors in the measurement of η: pile-up, weighting potential cross-talk and charge sharing. Fig. 4.2 shows how the phenomena of pile-up and charge sharing can affect the measurement of the correction factor η.

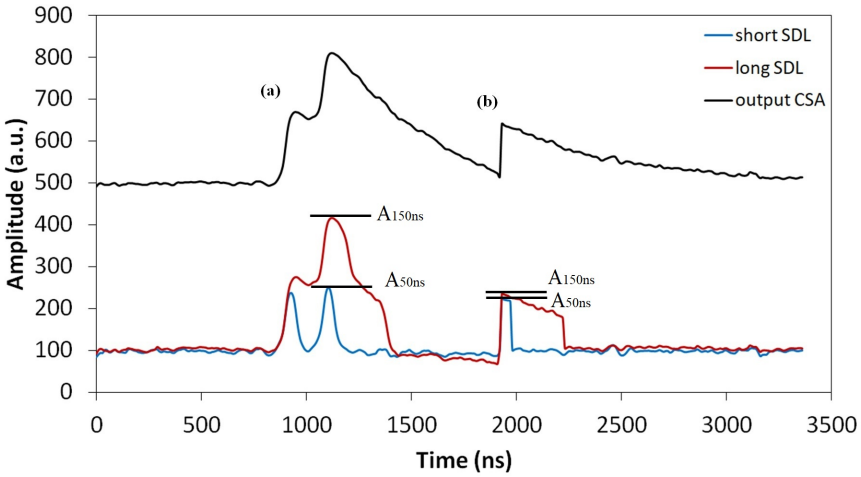

Figure 4.2: Detected amplitudes of the double SDL for the measurement of η in the presence of the phenomenon of pile-up (a) and a charge sharing (b). Here a value of T_{Dshort}=50 ns and a value of T_{Dlong}=150 ns were chosen.

The solution proposed consists in a first step to reject the events causing an error in the estimation of η through particular *Selection Rules* and calculate the ratio between A_{short} and A_{long} for the selected pulses. After this operation it is necessary to average on a big number of selected pulses the value of the measured η in order to overcome on the noise on the correction factor measurement. Fig. 4.3 represent the diagram illustrating the concept of the proposed method.

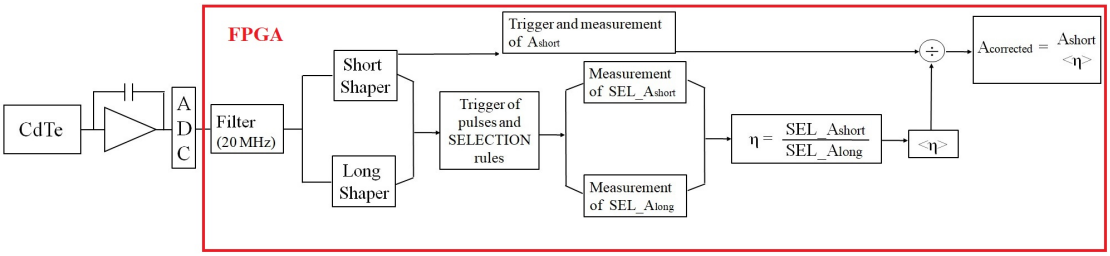

Figure 4.3: Diagram of the entire processing for the correction method proposed.

The rejection of a part of the detected pulses and the averaging operation does not call into question the effectiveness of the correction because the variations of the ballistic deficit is slow process. The time required to correctly estimate the correction factor, given the large number of pulses processed per second, will be fast enough.

4.2 Characterization of the ballistic deficit compensation method

A preliminary characterization of the correction factor calculated for all the pulses from the CSA is done. The first important step of the proposed method is the choice of the shaping times characterizing the double shaper.

4.2.1 Choice of T_D for the shaping circuits

The choice of T_D for the two SDL is the first important step in the proposed method for the measurement of η. The choice of T_D for the short delay line is done in order to detect the pulses event at high count rate, when the phenomenon of the pile-up becomes significant. In this work, we will use a SDL of 50 ns, because we have shown that it constitutes a good compromise between energy resolution and dead-time for high count rate measurements in the 10^6 c/s range.

The value of T_D for the long delay line is the one responsible of the estimation of the ballistic deficit. For this reason it is necessary to collect all the charges within the peaking time of the CSA. A possible way to evaluate the good shaping time for the complete charge collection is to study the position of the main photoelectric peak of the γ-source of ^{57}Co (Fig. 4.4). The estimation of the peak position is performed with a Gauss fit.

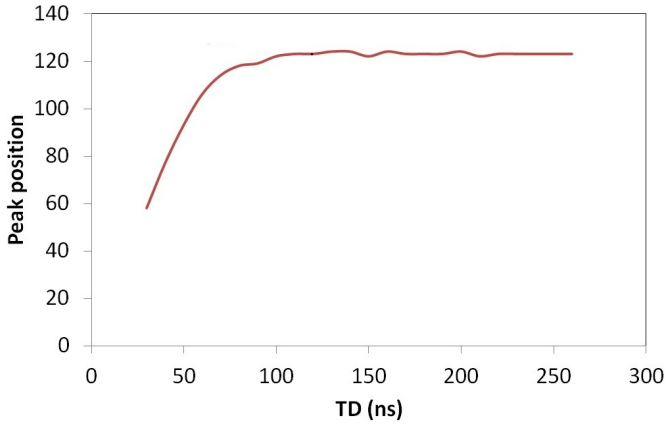

Figure 4.4: Photoelectric peak position of the ^{57}Co at different shaping times.

When we are in presence of the ballistic deficit the measured amplitudes of the pulses from the SDL is smaller compared to the case of a complete charge collection. For this reason we find a variation of the position of the photoelectric peak when different delay lines are applied. It is possible to notice that the limit from which

we do not have ballistic deficit any more is $T_D \sim 100$ ns. According to this result, we set T_D=150 ns for the long SDL.

4.2.2 Measurement of the ballistic deficit

Once the two T_D are chosen the correction factor is calculated as $< \eta >=< \frac{A_{50ns}}{A_{150ns}} >$. The characterization of the correction factor is studied with an X-ray beam at different count rates. The tube was set to a constant voltage of 120 kV and a variable current was applied. The X-ray beam was filtered with a 2,7 mm thick copper filter. Tab. 4.1 shows the characteristics of the beam used for this first test.

Voltage Tube (kV)	Current (mA)	Count rate (Mc/s)
120	1	0,8
120	2	1,7
120	4	2

Table 4.1: X-ray beam characteristic for the characterization of η measurement.

The FPGA is used to record the pulses made of 2560 samples for the 16 channels of the matrix. The process performed on the registered pulses consists in applying the two shaping circuits, triggering and measuring the amplitudes of each pulse from the two SDL. Then we record the distribution of the computed value η of each pulse. The analysis was done for the 3 count rates.

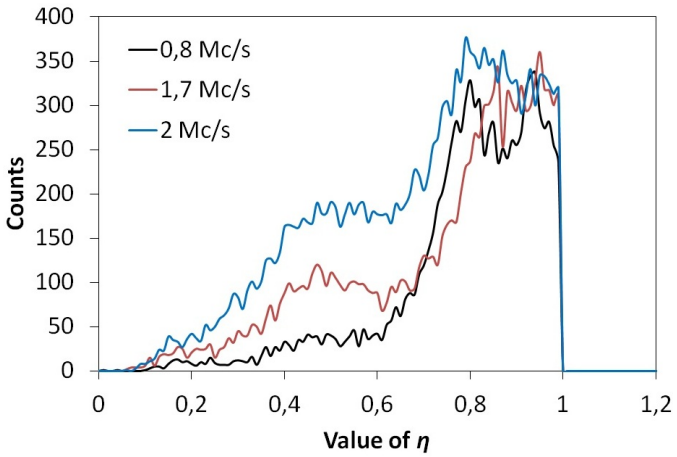

Figure 4.5: Distribution of the η values for the 3 different tube currents considered.

Fig. 4.5 shows the results obtained for 1 single pixel. Similar results are obtained on every pixel of the matrix. From the distributions obtained it is possible to notice that the spread of the values of η is significant, showing that the correction factor

cannot be estimated from one single event. Morever, with the increase of the count rate we notice an increase of the lower values of the distribution with a consequent increase of this spread. Therefore, if we compute the average of the distribution we obtain $< \eta >$=0,798 at 0,8 Mc/s, $< \eta >$=0,741 at 1,7 Mc/s and $< \eta >$=0,697 at 2 Mc/s. The value of the correction factor depends significantly on the flux with a variation of the 11% between low and high flux. The main cause of this effect is the phenomenon of the pile-up, with the consequent under-evaluation of the correction factor.

4.2.3 Compensation of the ballistic deficit

It is now possible to evaluate the efficiency of the compensation method.

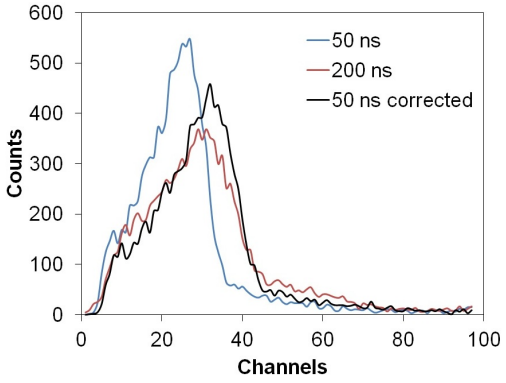

(a) 0,8 Mc/s.

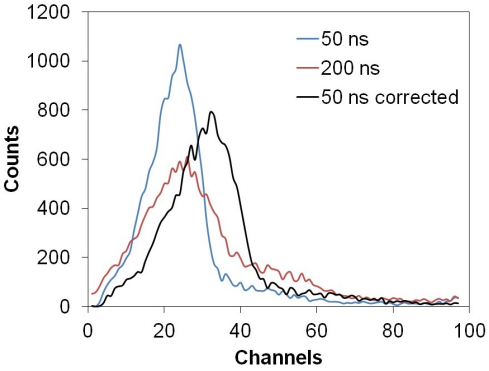

(b) 1,7 Mc/s.

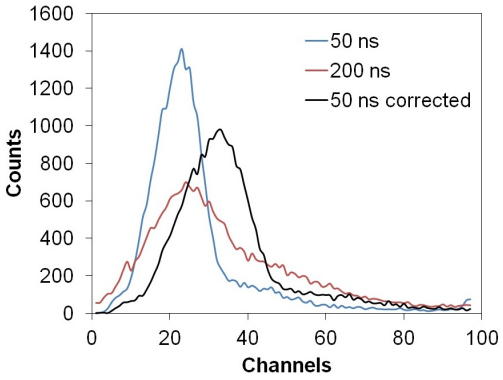

(c) 2 Mc/s.

Figure 4.6: Pulse height spectra obtained at different count rates with SDL with T_D=150 ns (red) and with with T_D=50 ns before (blue) and after the correction (black).

Fig. 4.6 represents the results obtained at different count rates with the short and the long SDL and the corrected spectrum obtained with the correction factors estimated above. These results further underline the effect of the incorrect

estimation of the compensation factor. We can see that the PHS are not correctly compensated because of the phenomena of pile-up or charge sharing which can affect the measurement of η and thus the compensation of the ballistic deficit. When the count rate increases, the pile-up becomes important and the compensated spectra shift to the right. These results show that it is important to reject these undesirable events.

4.3 Selection Rules

The selection and thus the rejection of pulses which can affect the measurement of the correction factor is an important step for the compensation of the ballistic deficit. In this Section we are going to present the selection rules used for the rejection of these undesirable effects from the measurement of the correction factor.

4.3.1 Pile-up rejection

The main source of error in the computation of the correction factor η is the phenomenon of pile-up. The phenomenon of pile-up is important because of the use of the long SDL for the measurement of the ratio in Eq. 4.1. When a pulse is affected by pile-up the apparent rise time is abnormally high because the long shaping circuit is not able to distinguish two pulses occurring in a short temporal window.

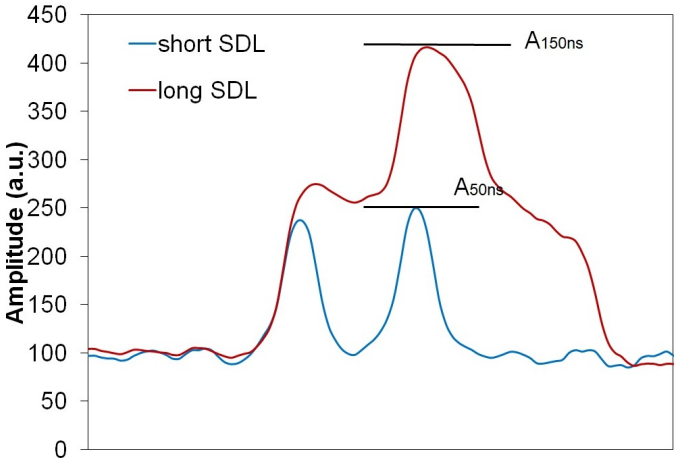

Figure 4.7: Detected amplitudes for the double SDL for the measurement of η in presence of pile-up.

Fig. 4.7 clearly shows that in presence of pile-up events (a), the detected amplitude from the long shaping circuit, A_{150ns}, does not correspond to the real value of the energy deposited in the detector. The effect of the pile-up for a long shaping time

is an over-evaluation of this information because the signal is not able to return to its baseline before the beginning of the second pulse. The consequence of this effect is an under-estimation of the real value of the correction factor. When the flux increases the number of pile-up events becomes significant. The main consequence on the measurement of the correction factor is a dependence of η on the flux. For this reason a preliminary rejection of these events is needed in order to recover the correct value of η.

Time Over Threshold technique

Among the state of the art presented in the previous Chapter for the different methods of pile-up rejection, we want to apply a method that is suitable for an FPGA real-time implementation. The Time Over Threshold technique consist in few digital elements such as a comparator and a counter. The pulses from the two shapers are compared to an amplitude threshold. Once the pulse crosses the threshold, a temporal window is opened and increased with the clock count. When the signal falls below the threshold, the temporal window is closed and its length compared to a fixed value, here called TOT_{SDL}. In order to obtain the optimal value that ensures a good rejection efficiency, we fixed the TOT_{SDL} as the temporal duration of an isolated pulse. Fig. 4.8 shows the pulses at the output of the two SDL circuits induced by α particles from a 5,156 MeV ^{239}Pu radioactive source. The red signal indicates the temporal window for both the SDL.

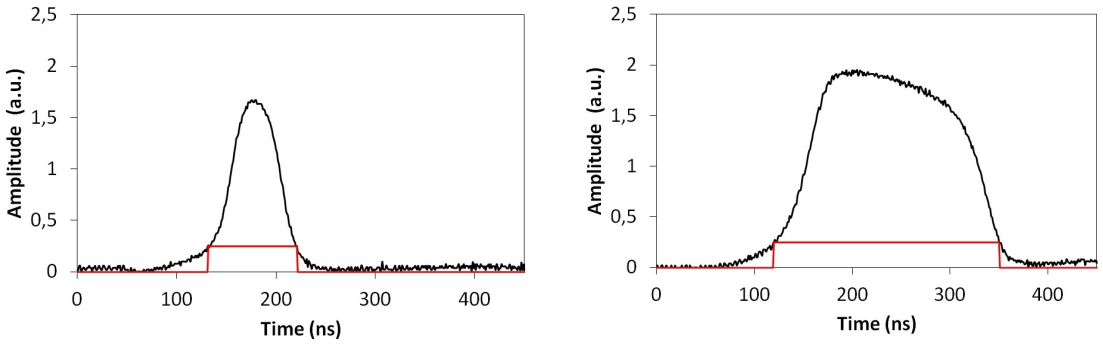

Figure 4.8: Measurement of a the temporal width for the TOT technique of the pulses from the fast shaping circuit (left) and for the slow one (right).

As it is possible to notice from the isolated pulses, the SDL algorithm imposes the output to have the width equal to T_D until its peaking time plus a $\Delta t = 1$ clock cycle (10 ns in our case), in order to let the signal returning to its baseline. Thus, the TOT_{SDL} of the shapers are set at 60 ns and 210 ns for the fast the slow SDL, respectively.

In the following example the long shaping circuit is not able to separate two pulse pile-up and the energy information recorded is then false. Fig. 4.9 shows the situation in which the TOT technique rejects the pile-up from the measurement of η.

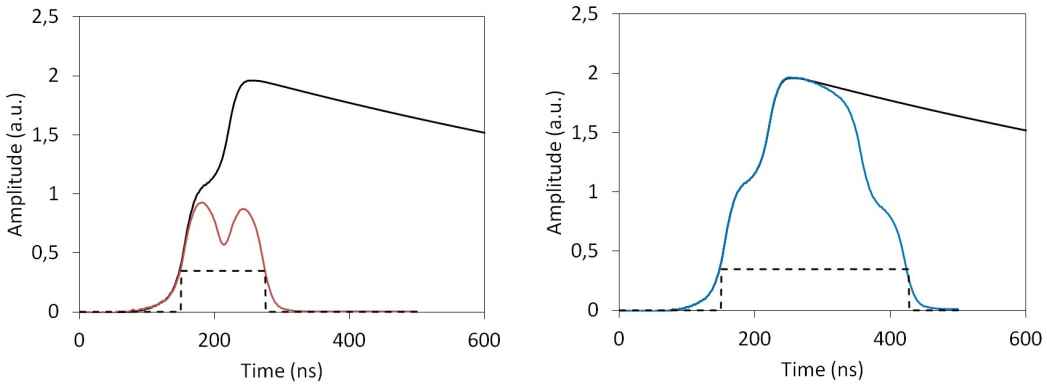

Figure 4.9: Pile-up rejection when the short shaping circuit (left,red) and the long one (right,blue) are not able to detect the pile-up from the CSA (black).

It is possible to see that both the temporal windows for the fast and slow shaping circuit are longer than the fixed value set with the single pulses. In this example, the TOT_{SDL} is 120 ns and 270 ns for the fast and slow shaper, respectively. The pulse will therefore be rejected from the calculation of the correction coefficient. In general, with this rule we reject all the pulses in which TOT_{SDL}>210 ns for the long SDL, i.e. the one causes more problems for the pile-up detection.

Measurement of η after pile-up rejection

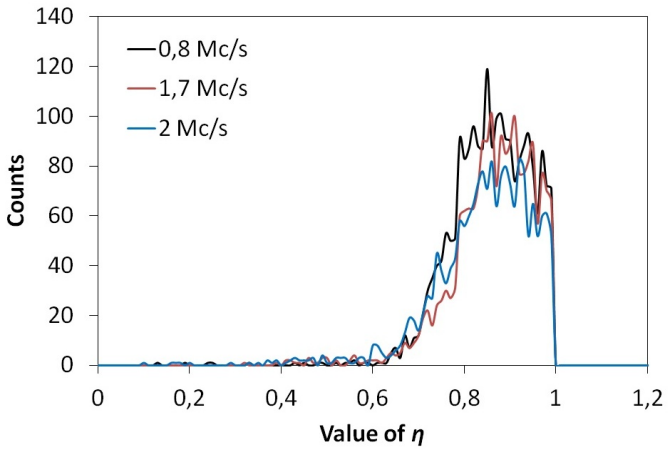

Figure 4.10: Distribution of the η values for the 3 different currents considered after the application of the pile-up rejection.

Once the rejection of pile-up events is performed, the data of the previous acquisition with the X-ray tube set to 120 kV and different currents (Tab. 4.1) were processed again. Fig. 4.10 shows the distribution of η values at different count rates after the rejection of pile-up events with the method presented above. From these distributions it is possible to notice that the spread of the values of η is significantly reduced. Moreover, with the pile-up rejection we are able to measure a distribution of the value of η that is independent on the count rate. To achieve this result an increasing fraction of the detected X-rays are rejected from the calculation of $< \eta >$. Tab. 4.2 gives an estimation of the fraction of rejected events for the 3 tube currents.

Voltage Tube (kV)	Current (mA)	Count rate (Mc/s)	Pile-up rejected (%)	$< \eta >$
120	1	0,8	11	0,863
120	2	1,7	28	0,854
120	4	2	42	0,841

Table 4.2: Number of rejected pile-up events at different count rates together with the value of $< \eta >$.

Tab. 4.2 underlines again the importance of the pile-up rejection. The fraction of rejected pile-up events when the count rate is rather high (2 Mc/s) is almost the half of the detected pulses. While for lower count rates ($\sim$1 Mc/s) the fraction of rejected pulse is almost 4 times smaller. However, it is important to emphasize that these events are not removed from the final pulse heigh spectrum. Our objective is to correct the instability caused by the ballistic deficit, but without affecting the measured photon statistic.

These results show a significant decrease of the variation of the computed value of $< \eta >$ to less than 2,2% compared to 11% without pile-up rejection.

4.3.2 Charge sharing and weighting potential cross talk rejection

We have observed that the phenomena of charge sharing is characterized by a fast rise-time compared to other pulses. This effect is a consequence of the shape of the weighting field presented in Chapter 1. Fig. 4.11 shows the shape of the weighting potential at different pixel positions.

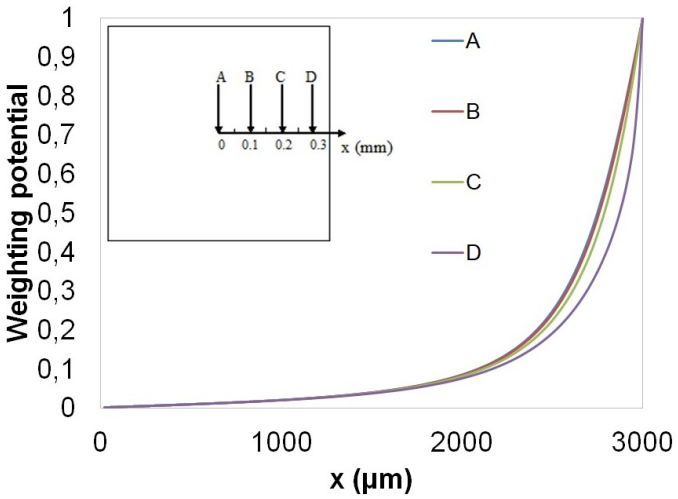

Figure 4.11: Weighting potential as a function of the position in the pixel.

The profile of the weighting potential presents a steeper slope at the boarder of the pixel and thus the induced pulses are faster. In order to better understand the effect, Fig. 4.12 represents recorded pulses from two SDL at different shaping time when the phenomenon of charge sharing occurs.

Figure 4.12: Detected amplitudes for the double SDL for the measurement of η in presence of charge sharing.

If a signal has a rise time faster then the shorter shaping time we do not have ballistic deficit because the delay line is able to collect all the charges without any loss of information. In this case the two amplitudes for the measurement of η are equal. The effect is an over-estimation of the correction factor.

As well as charge sharing, pulses induced by weighting potential cross-talk are characterized by a fast rise-time too. Fig. 4.13 illustrates recorded pulses on adjacent pixels in presence of weighting potential cross-talk.

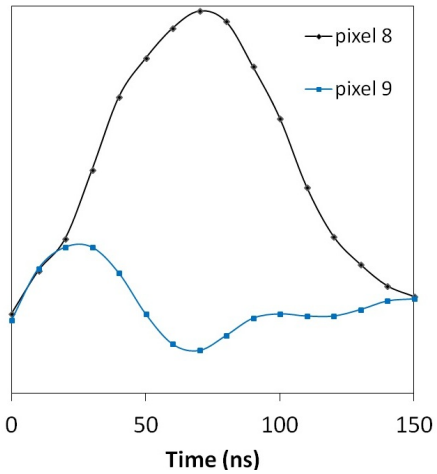

Figure 4.13: Detected weighting potential cross-talk on adjacent pixels [9].

The weighting potential cross-talk induce a transient signal with a net charge equal to zero on the neighbouring pixel. The transient signal is characterized by a positive lobe with a faster rise time compared to the detected pulse on the adjacent pixel. Fig. 4.14 shows the shape of the weighting potential among neighbouring pixel illustrating the cause of the phenomenon.

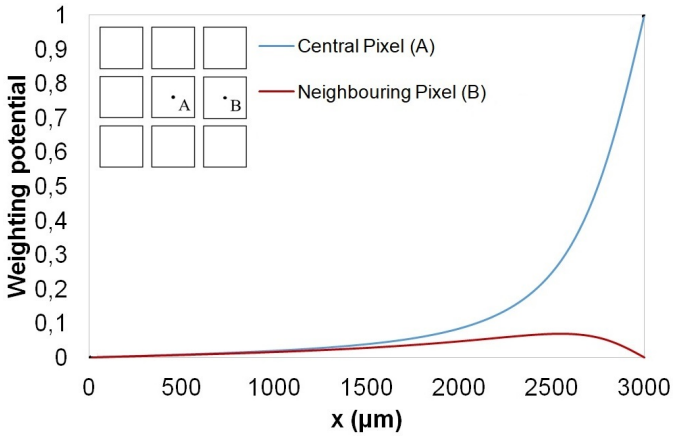

Figure 4.14: Weighting potential on two adjacent pixels.

In order to recognize these events and thus the signals characterized by a rise-time faster than the short shaping time two possible ways of processing these signals are presented: *Time Coincident Window* technique and *Rise-time Discrimination* technique.

Time Coincident Window technique

The Time Coincident Window technique is a classical technique used to detect signals occurring simultaneously on neighbour pixels, to correct the effect of the

charge sharing on the pulse height spectra. In our case, the TCW technique consists in the detection and thus in the rejection of pulses from the calculation of $< \eta >$, when they are detected in a fixed temporal window, called here *TW*. The value of TW was set to 10 ns in order to detect pulses arriving in Δt $<$ 10 ns. When a pulse is triggered, we are going to check if in the TW of 10 ns other pulses on its 4 neighbour pixels are detected too. In this case we reject pulses arriving on neighbour pixels within 10 ns before or after the pulse is detected in the central pixel. The concept can be easily extended to weighting potential cross-talk too. We will see that with this technique we are able to detect charge sharing and weighting potential cross-talk events, but also true coincidences occurring when two or more X-ray photons are detected by two adjacent pixels within the time coincidence window. These latter increase with the count rate.

Measurement of η with the TCW technique

Fig. 4.15 represents the distribution of the values of η when, together with the pile-up rejection, the rejection of the events in the fixed TW is performed. The experimental conditions used are the same as those used in the previous Section (see Tab. 4.1).

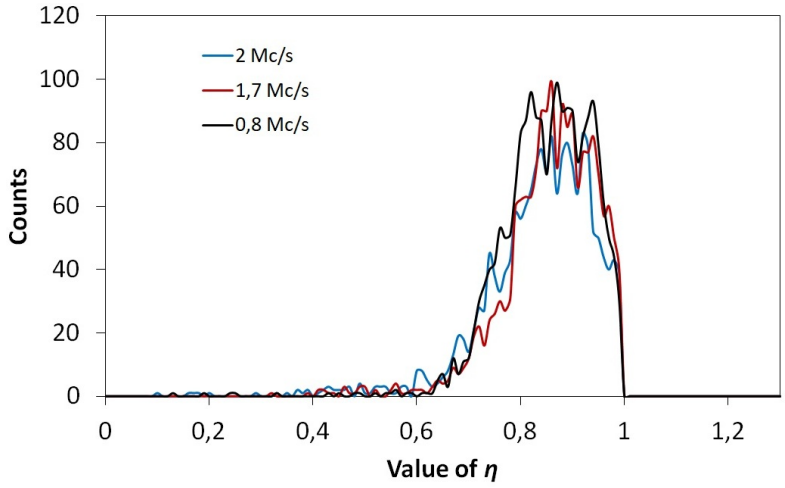

Figure 4.15: Distribution of the value of η for the 3 different currents considered after the application of the TCW technique.

In order to evaluate the number of charge sharing and coincident events rejected, Tab. 4.3 summarises the fraction corresponding to these events.
The fraction of charge sharing and weighting potential cross-talk events is not flux dependent. With this technique we consider these phenomena, but also the true coincidences. The dependence on the flux its caused by these latter events. The true coincidences, on the contrary for charge sharing or weighting potential cross-talk,

Voltage Tube (kV)	Current (mA)	Count rate (Mc/s)	TCW events rejected (%)	$< \eta >$
120	1	0,8	9	0,863
120	2	1,7	11	0,853
120	4	2	15	0,845

Table 4.3: Number of rejected events from the TCW technique at different count rates together with the value of $< \eta >$.

are not mandatorily characterized by a rise-time that is faster than the shorter shaping time, i.e. T_D=50 ns. For this reason with the TCW technique we may exclude for the measurement of η pulses that give a correct estimation of the factor $< \eta >$. For this reason, a second method for the rejection of pulses characterized by a fast rise time is here proposed.

Rise-time discrimination technique

This second method proposed is based on the rise time of the signals from the two shaping circuits. The method measures the temporal duration of the fist derivative positive lobe of the SDL signals and compares it with a fixed temporal value called T_{rise}.

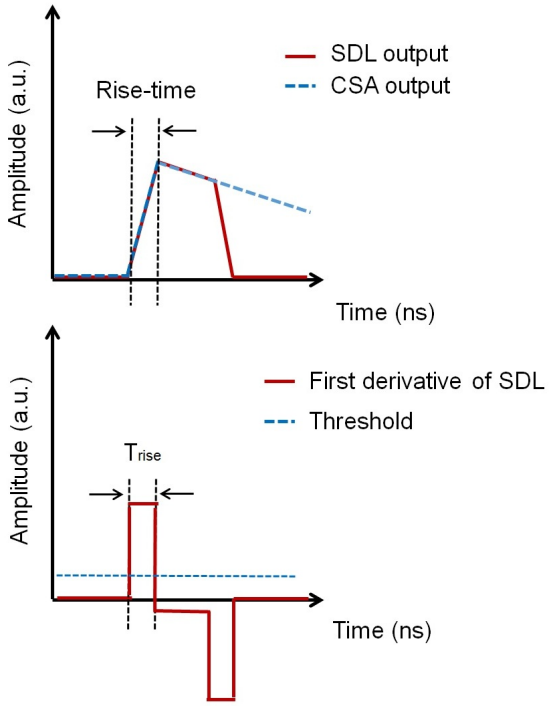

Figure 4.16: Simulation of the first derivative technique for the rise time estimation.

The value of T_{rise} was set at 30 ns. If the temporal duration of the positive lobe of

the first derivative of the signals from the shaping circuit is shorter than this value, then the rejection of the pulse is performed. Fig. 4.16 represents the principle of the rise-time discrimination technique for the rejection of fast rise time pulses induced by charge sharing or weighting potential cross-talk events.

Measurement of η with the rise-time discrimination technique

As we did for the pile-up rejection and for the TCW technique, we are going to measure the values of η after the rejection of events characterized by a fast rise-time. The experimental conditions used are the same as those used in the previous Section (see Tab. 4.1). Fig. 4.17 shows the resulting distribution of the value of η when the rise-time discrimination technique is applied.

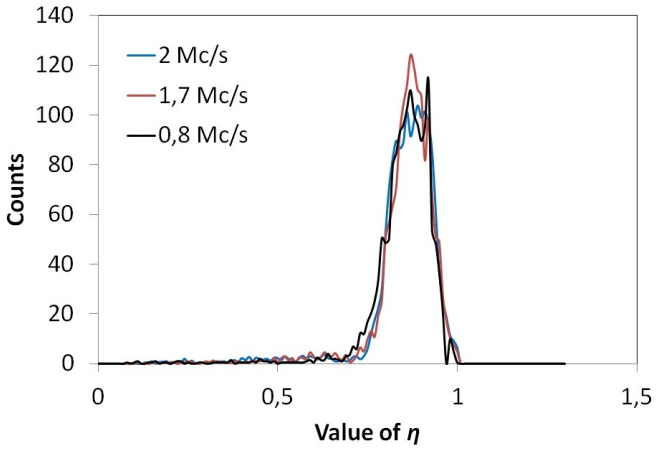

Figure 4.17: Distribution of the value of η for the 3 different currents considered after the application of the rise-time rejection technique.

Tab. 4.4 summarizes the results obtained with the rise-time discrimination method and the fraction of rejected events at different count rates.

Voltage Tube (kV)	Current (mA)	Count rate (Mc/s)	Fast rise-time rejection (%)	$< \eta >$
120	1	0,8	11	0,861
120	2	1,7	12	0,851
120	4	2	10	0,847

Table 4.4: Number of rejected events with a rise-time faster than 30 ns at different count rates together with the value of $< \eta >$.

The results obtained show a slight improvement on the measured variation of the value of $< \eta >$, i.e. 1,4%. These results demonstrate that with the use of the rise-time discrimination we are able to detect and thus reject the real cause of the

over-estimation of $< \eta >$. With the TCW technique we do not totally consider the fraction of events characterized by a rise-time faster than the short shaping time because of the presence of the true coincidences. The rise-time discrimination technique was developed for this purpose.

4.3.3 Compensation of the ballistic deficit with selection rules

We demonstrated that with the use of the selection rules we can measure a correct $< \eta >$ independent on the count rate. Once the value of $< \eta >$ is measured it is possible to perform the compensation of the ballistic deficit effect. The pulse height spectra from the SDL with a shaping time of 50 ns and 150 ns are performed and the correction of the spectra is obtained for the short shaping circuit. Fig. 4.18 represents the results obtained at different count rates (see Tab. 4.1) when the selection rules are applied for the pulse height spectra obtained with the short shaping circuit before and after the correction.

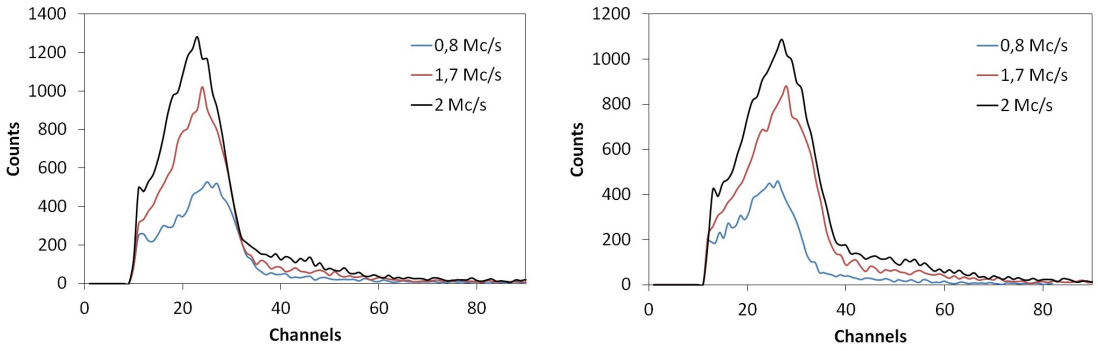

(a) SDL with T_D=50 ns before the correction. (b) SDL with T_D=50 ns after the correction.

Figure 4.18: Pulse height spectra obtained at different count rates with SDL with T_D=50 ns before (left) and after (right) the correction of the ballistic deficit with the use of the selection rules.

The improvement of the compensation method is visible here. It is possible to notice the shift on the right of the spectra before the correction algorithm. Once we perform the correction the shift of the spectra is deleted.

The use of the selection rules for the rejection of the undesirable phenomena affecting the measurement of $< \eta >$ ensures a correct compensation of the phenomenon both at low and high count rate.

4.4 FPGA implementation

In this Section, some important key points of the implementation on FPGA of the real-time algorithm is presented and discussed. The diagram in Fig. 4.19 represents the diagram with the main operations performed by the FPGA for the proposed method.

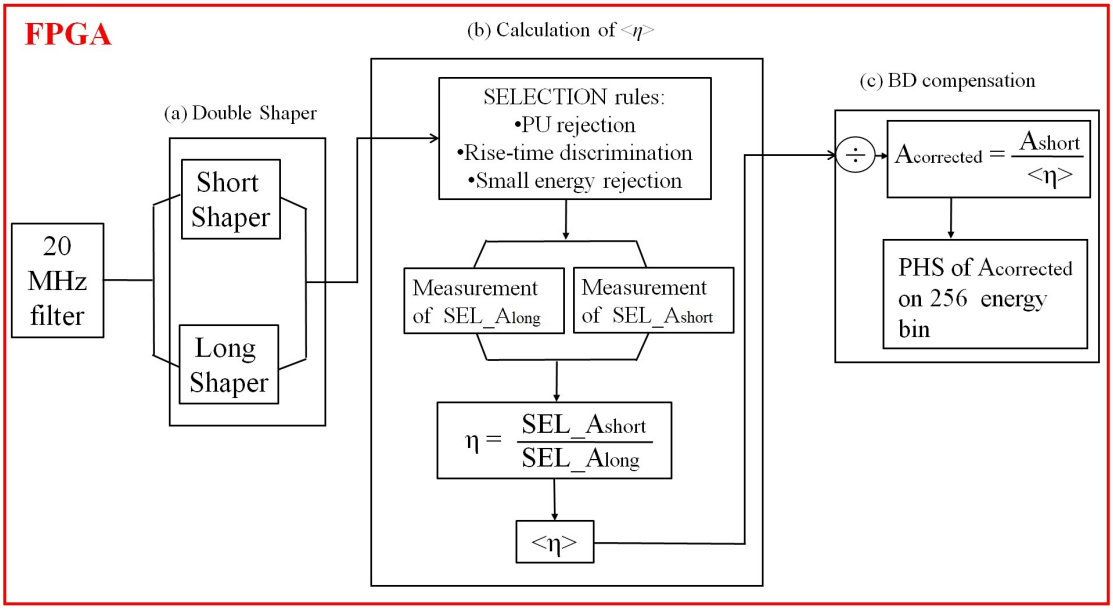

Figure 4.19: Diagram of the implementation of the real-time digital compensation algorithm.

The digitized signal from the ADC is sent to the FPGA which will carry out the processing operations represented in the 3 different blocks, summarized as follow:

- A fist block (a) for the two SDL shapers with shaping time of 50 ns and 150 ns.
- A second block (b) for the calculation of $< \eta >$ composed by three main operations. The selection rules with the rejection of pile-up and discrimination of rise-time, the calculation of the ratio for each selected pulse and then the average for the value of the correction factor.
- A third block (c) for the ballistic deficit compensation. Among them the correction of the amplitudes A_{50ns} with the averaged correction factor and the construction of the corrected PHS on 256 bin.

Several operations carried out during different stages of the method need to be adapted for the FPGA implementation.

4.4.1 Numbers representation and divisions

The first choice to make for an FPGA implementation is the representation of the numbers we deal with. The value of the correction factor (η ~0,85) can be represented with a floating point arithmetic and in this case the number of resources required on the FPGA for the binary number is big (32 bit or more). We decided to use a fixed point arithmetic for the representation of η on 10 bit. This solution is preferable because in this way we are going to deal only with integer numbers and it is easier to work with a fixed point arithmetic representation rather than with a floating point one.

The algorithm is characterized by two operations performing the ratios of two quantities. The first one is the ratio between the amplitudes of the pulses from the double shaping circuit, i.e. $\frac{A_{50ns}}{A_{150ns}}$. The second ratio is the one between the amplitudes from the fast shaper and the averaged correction factor, i.e. $\frac{A_{50ns}}{<\eta>}$. The operation of the division is difficult to manage in VHDL since it requires a large number of delay units which slow down the operations and increase the number of resources needed. For this reason we decided to invert the first ratio, in the following way:

$$\eta' = \frac{A_{150ns}}{A_{50ns}} \tag{4.3}$$

The new correction factor η' is inverted but the concept is still the same. In fact, if from the first version we found a value of η ~0,85, with this inversion we get η' ~1,17. We still work in fixed point representation of numbers on 10 bit. In this way the operation for the correction of the ballistic deficit of the fast shaping circuit is performed with a multiplication instead of a division:

$$A_{corrected} = A_{50ns} \cdot <\eta'> \tag{4.4}$$

It is now clear that the limits of the value of η' are different. In fact, we have:

$$0 < \eta < 1 \qquad but \quad \eta' = \frac{1}{\eta} \qquad then \qquad \eta' > 1 \tag{4.5}$$

With the inversion of the ratio we theoretically need only the lower limit for the correction factor η'. In the reality we also need an upper limit because we use only 10 bit for its representation. In our experience, with the current setting of the two SDL circuits we have η>0,5 so that we can fix an upper limit of 2 for η'. Considering the dynamic of the ADC, we decided to multiply the value of η' by 512. The digital format of the correction factor is then called η'_D and thus:

$$512 < \eta'_D < 1023 \tag{4.6}$$

In order to evaluate the real computed value of η'_D in the real-time processing, the distribution of these value can be registered on 256 bin, i.e. a number on 8 bit. It is now necessary to understand the conversion adopted for η'_D in order to get the original value of η. The value of η'_D is represented on 10 bit and if we want to register it on 256 bin it is necessary to divide it by 4. In particular, the value of η'_D it is represented by $4 \cdot channel$ in 10 bit. After this consideration, it is possible to find the real value of η starting from the value in channels, applying Eq. 4.6 and 4.5. We obtain:

$$\eta' = \frac{1}{\eta} \qquad thus \qquad \eta' = \frac{channel \cdot 4}{512} = \frac{\eta'_D}{512} \tag{4.7}$$

With this conversion it is possible to find the real value of $< \eta >$ starting from its value on 8 bit in the 256 channels.

4.4.2 Small amplitude pulses

A problem observed during the implementation of the method in FPGA is the incorrect compensation of the ballistic deficit when small amplitude pulses are considered. A preliminary test of the compensation algorithm was performed with the detector in its stable condition, i.e. biased some hours before the tests. The two γ-sources of ^{57}Co (122 keV) and ^{241}Am (59,5 keV) were used simultaneously in order to obtain a count rate of 250 c/s. The measurement of the correction factor is performed in real-time as well as the PHS on 256 energy channels.

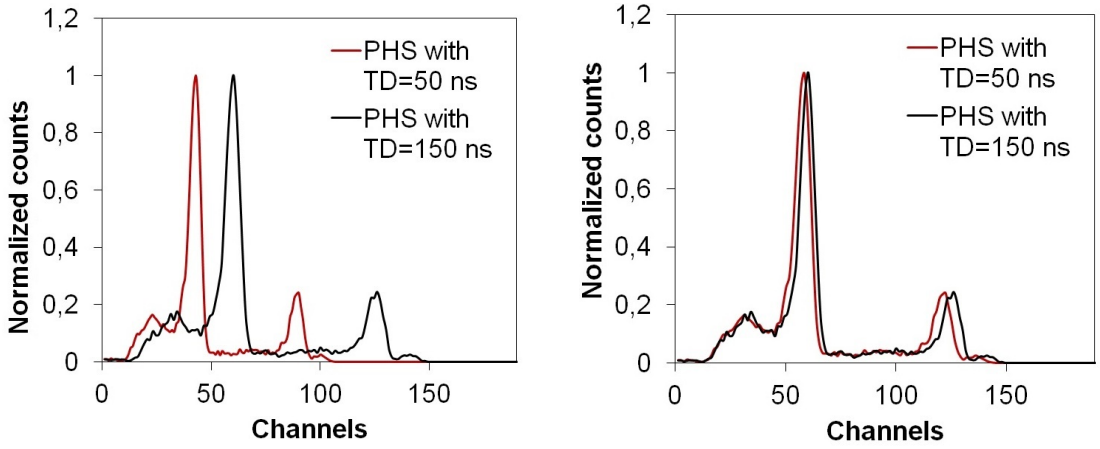

Figure 4.20: Pulse height spectra of the ^{57}Co and ^{241}Am γ-sources superposed before (left) and after (right) the correction algorithm.

Fig. 4.20 represents the PHS obtained with two SDL characterized by T_D=50 ns and T_D=150 ns before and after the correction algorithm. From this test it is possible to notice that the compensation of the spectrum obtained with T_D=50 ns is incorrect. In order to better investigate on this effect, the algorithm was tested for the two sources separately with a count rate of 100 c/s for the ^{57}Co and 150 c/s for the ^{241}Am. Fig. 4.21 represents the PHS obtained with two SDL characterized by T_D=50 ns and T_D=150 ns before and after the correction algorithm for the two separated sources. From these spectra it is possible to notice that the compensation of the ballistic deficit is well performed for the of the ^{57}Co but not for the ^{241}Am, that means that the correction factor is not well measured in this second case.

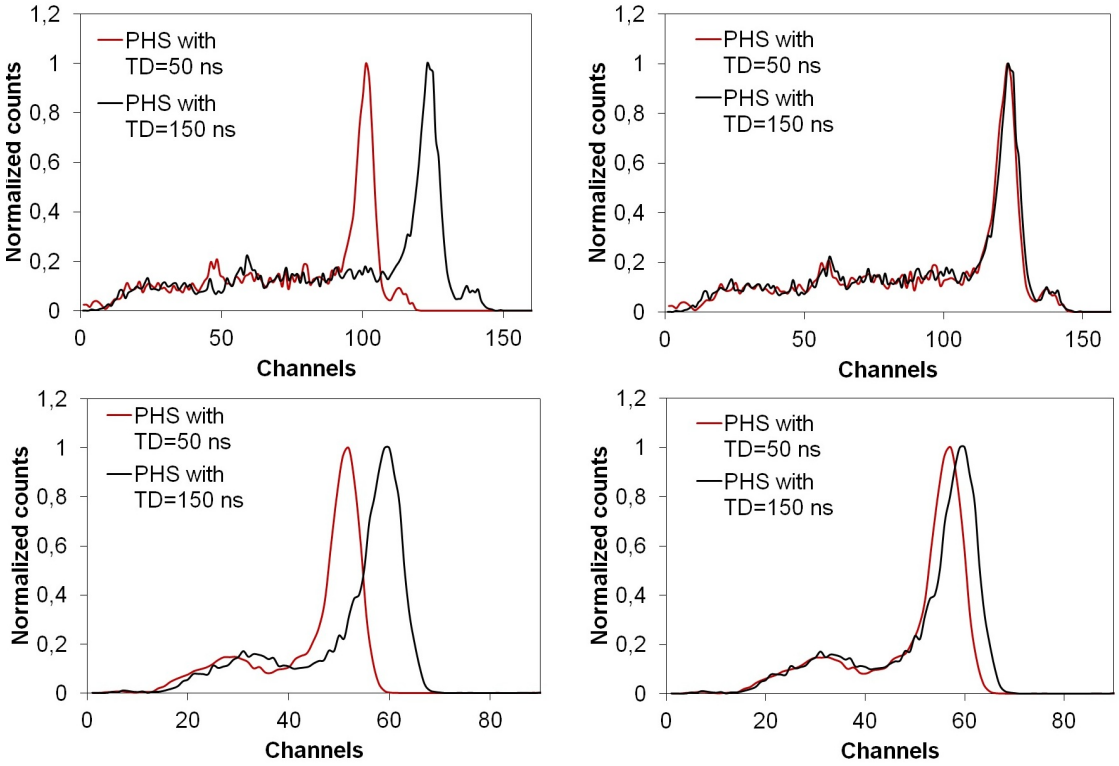

Figure 4.21: Pulse height spectra of the ^{57}Co source (top) and ^{241}Am source (bottom) before (left) and after (right) the compensation algorithm.

The encountered problem is due to the implementation on the FPGA for the process of the smaller energy photons. This aspect can be related to:

- the electronic noise;
- offset on the measurement of the amplitudes of the pulses from the double shaper;
- insufficient digitalization accuracy in the measurement of η'_D for small energies.

At the moment, we by-passed the problem by excluding the low energy pulses from the calculation of the correction factor $< \eta >$ by adding an amplitude threshold on the signals from the double shaping circuit. The measurements performed with the two γ-sources separately suggest to eliminate the pulses with an energy E<60 keV.

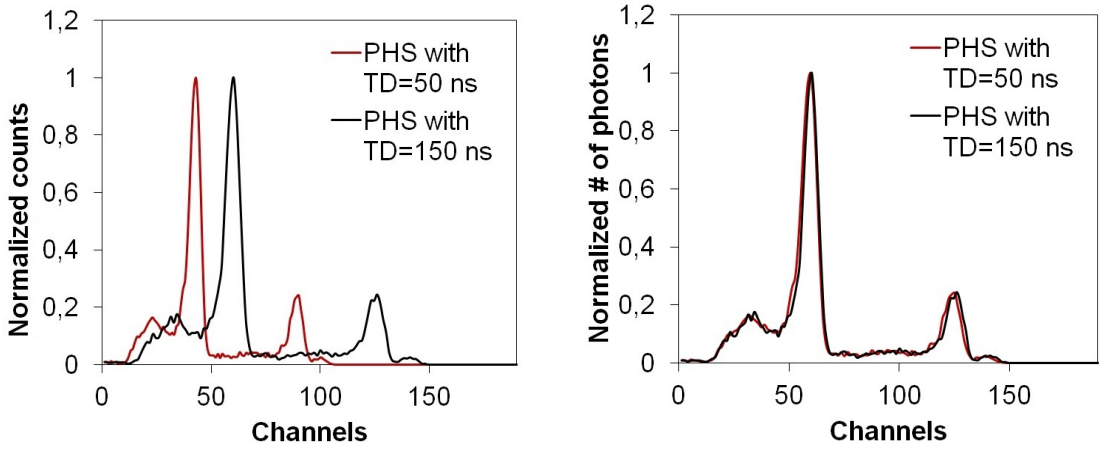

Figure 4.22: Pulse height spectra of the ^{57}Co and ^{241}Am γ-sources superposed before (left) and after (right) the correction algorithm with the selection on higher energy photons.

Fig. 4.22 represents the PHS obtained before and after the compensation algorithm for the two γ-sources simultaneously with the rejection of low energy amplitudes from the measurement of η'_D. The results show that now the obtained PHS from the SDL with T_D=50 ns is well compensated.

The rejection of energies smaller than 60 keV permits to correctly perform the compensation of the ballistic deficit. Despite the encouraging result, further examination are currently being done in order to better understand the real cause of the problem.

4.4.3 Exponential moving average

Another problem due to the implementation of the method in FPGA is the final average for the estimation of the correct compensation factor. A suitable way of an FPGA implementation for the operation of the average is the *Moving Average*. The choice of the suitable value of pulses for the average is an important step during the implementation on the FPGA. The study for the choice of the number of pulses was performed on a distribution of calculated values of η (Fig. 4.23).
We want to find a number of pulses, N, to reduce the noise on the measurement of $< \eta >$ and suitable for an FPGA implementation. For this latter reason we decided

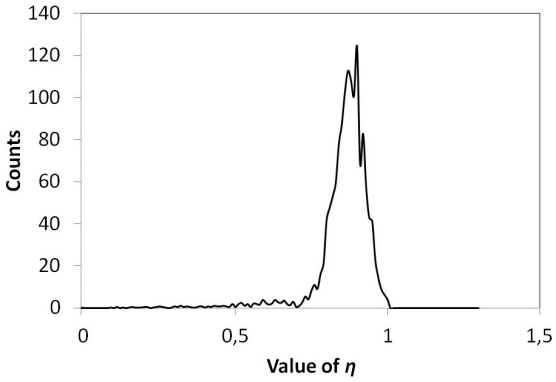

Figure 4.23: Distribution of the value of η at 1 Mc/s.

to study the case of N as a power of 2, because in FPGA it is simply a binary shift. Fig. 4.24 represent the normalized distribution of the value of η when different N are considered.

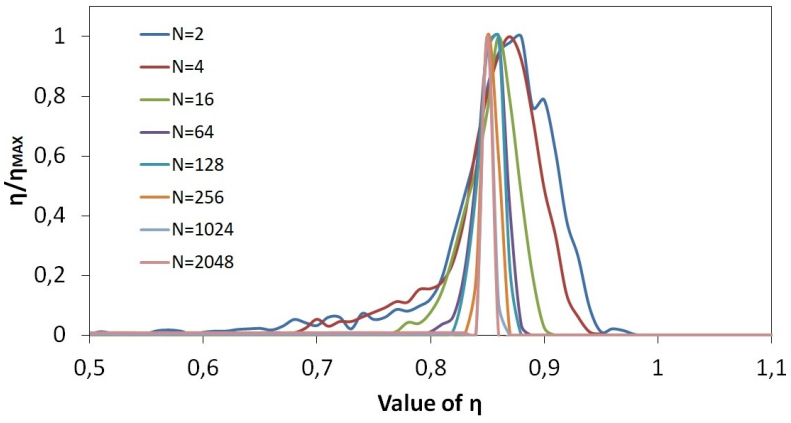

Figure 4.24: Normalized distribution of the value of η when different value of N are applied for the moving average.

The distributions obtained show that the spread is smaller when a big number of N is used for the average. In order to better evaluate the effect of the different N used for the average, the centroid and the standard deviation of the distribution is reported in Tab. 4.5.

N	2	4	16	64	128	256	1024	2048
$< \eta >$	0,872	0,866	0,857	0,853	0,852	0,852	0,852	0,851
σ	0,206	0,187	0,148	0,135	0,129	0,102	0,087	0,087

Table 4.5: Values of $< \eta >$ after the use of different values of N in the moving average.

It is clear that with the use of a bigger N the spread of the distribution is reduced

from a value of 24% when N=2 to 10% when N=2048. With N⩾64 the $< \eta >$ is in very good agreement with the value of η we expected (0,85) for the double shaping circuit used in the characterization of the proposed method. The moving average filter in FPGA is represented by a number of buffers according to the value of N or by a temporary memory in which the data have to be stored. In case of a big N, such as 1024 or 2048, the precision on the measurement of η is very good but the number of resources required to the FPGA is big. If the number of N is small, such as 16 or 64, the number or resources is reasonable but the precision on the measurement of η is degraded.

For this reason, we implemented an alternative solution, i.e. the *Exponential Moving Average*. The algorithm for EMA is here presented:

$$EMA(n) = EMA(n-1) + \alpha \cdot [input(n) - EMA(n-1)] \tag{4.8}$$

Where $\alpha = \frac{1}{2^M}$, 2^M is the number of values used for the moving average and *input(n)* represents the nth value of the computed η'_D. Fig. 4.25 shows the behaviour of the Exponential Moving Average algorithm proposed with different values of M applied. For this study a count rate of 1 Mc/s was used.

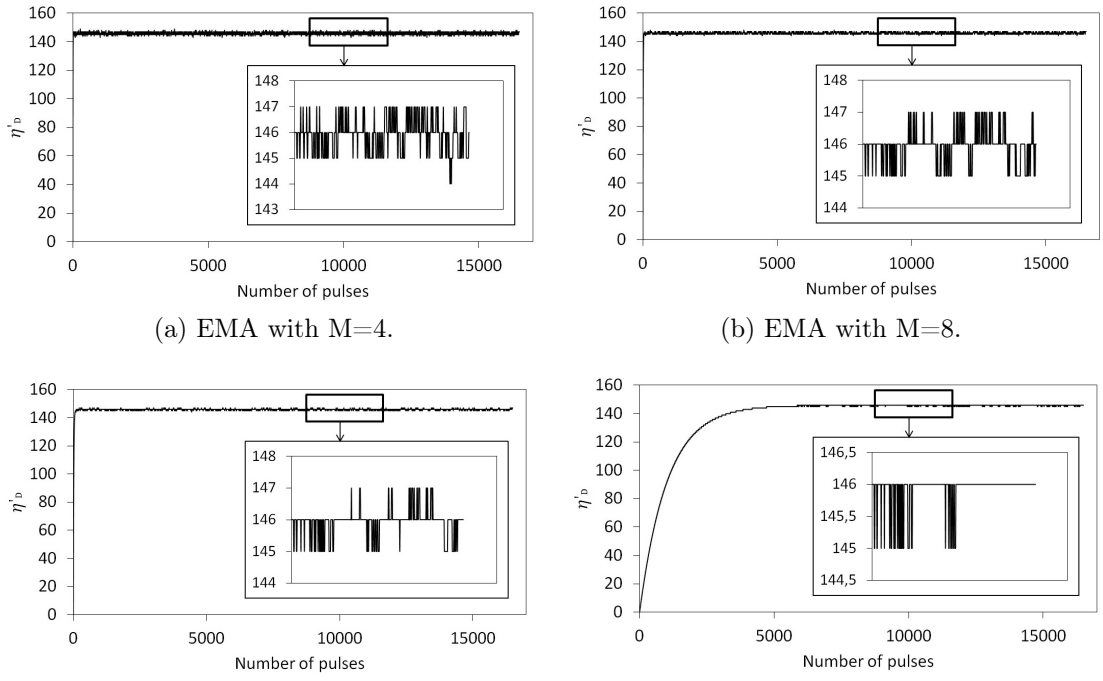

(a) EMA with M=4.

(b) EMA with M=8.

(c) EMA with M=10.

(d) EMA with M=12.

Figure 4.25: Results of the EMA algorithm with different values of M applied. The zoom underlines the oscillation between the channels.

This algorithm is easy to implement and requires fewer resources than the simple moving average. In fact, we only need one adder, a delay unit and M shifts of the value in square brackets. The power-2 shift is directly connected to the number of pulses we want to use to perform the exponential moving average. In order to investigate on the effectiveness of the algorithm proposed, a study on the behaviour of the EMA with different values of M was carried out. With a large number of pulses considered for the average (M=12) it is possible to see that the algorithm requires a certain time to converge, but once we are in the flat top of the response we find an oscillation between only two channels for the value of the correction factor, i.e. 1% of the variation on $< \eta >$. Tab. 4.6 summarizes the results obtained from the characterization of the EMA algorithm.

2^M	Time to converge at 1 Mc/s (s)	$< \eta >$ variation	σ
16	<0,001	0,85-0,89	0,41
256	<0,001	0,85-0,87	0,33
1024	0,001	0,85-0,87	0,25
4096	0,01	0,85-0,86	0,12

Table 4.6: Behaviour of the EMA algorithm with different values of M.

The results confirm that a big value of M an thus 2^M assure an accurate value of the correction factor. It means that the variations on $< \eta >$ are represented by a value smaller than 1%. On the other hand, with a big value of M the algorithm requires some time to converge. If the value of M=12 and thus 2^M=4096 the algorithm requires 0,02 seconds to converge. This mean that with a count rate of 1 Mc/s we lose 10000 pulses from the measurement of $< \eta >$. Thus we need more time in order to perform the correction. If we use a value of M=10 and thus 2^M=1024 for a count rate of 1 Mc/s we lose only 1000 pulses, i.e. around the 1% of 1 second acquisition. This seems a good compromise between precision of the measurement of the correction factor and resources need for the implementation on the FPGA.

4.5 Conclusions and discussions

The method presented in this Chapter has the objective of compensate the phenomenon of the ballistic deficit with a real-time process implemented in FPGA. Two shaping circuits are used for the measurement of a correction factor $< \eta >$ which gives an estimation of the ballistic deficit. This correction factor is used to compensate for the effect of the ballistic deficit of the fast shaping circuit. In this

way, we should be able to compensate for the instabilities observed in Chapter 3, without degrading the performances of the detector in terms of energy resolution and dead-time. We demonstrated the importance of the selection rules for the rejection of undesirable phenomena such as pile-up, charge sharing and weighting potential cross-talk, affecting the correct measurement of η. Among them the pile-up is the phenomenon which has a bigger impact on the estimation of the correction factor. The introduction of the TOT technique for the rejection of these events we are able to perform a correct measurement of this value even at a count rates up to 2 Mc/s reducing the variation of $< \eta >$ from 11% to 2%.

Chapter 5

Stability performance of the spectrometric detector with the ballistic deficit compensation method

In Chapter 4 a novel approach for the compensation of the phenomenon of the ballistic deficit was presented. Its key points were underlined through experimental measurements and the effectiveness of the proposed algorithm was demonstrated. In this Chapter we are going to present and discuss the results obtained with the algorithm for the compensation of the ballistic deficit in real-time in order to obtain a stable response of the detector over time. The efficacy of the method during all the operation time of the detector was tested under low and high fluxes.

5.1 System description

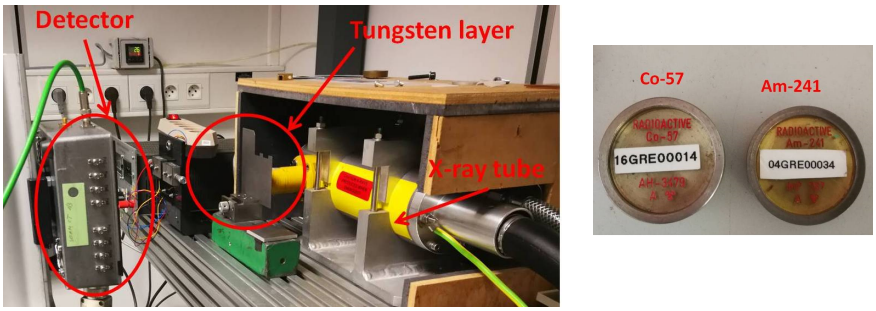

Figure 5.1: (Left) Test bench used for the experiments. (Right) γ-sources of ^{57}Co and ^{241}Am.

Fig. 5.1 represent the test bench used during the validation tests. The detector was tested with two γ sources (Fig. 5.1 on the right) or with an X-ray source, depending on the count rate needed. For γ-ray measurements the sources were placed above the detector window, almost 2 cm far from the CdTe sensor. For the X-ray measurements the detector is placed 20 cm from the source. A thin layer of Tungsten material (W) was used too.

The evaluation of the real-time compensation method is presented here for one pixel. The algorithm can be easily extended to the entire 4x4 matrix. Fig. 5.2 represents the diagram of the entire process developed on the FPGA.

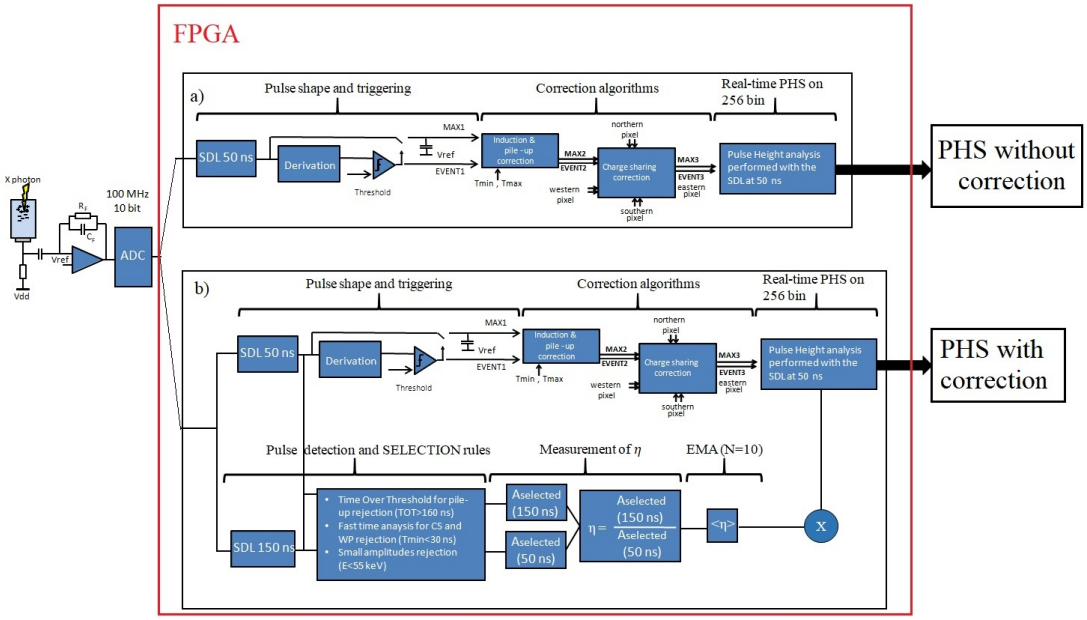

Figure 5.2: Diagram of the process developed on the FPGA for the stability improvement of the detector response.

In order to correctly compare the response of the detector before and after the correction algorithm, we have configured the FPGA to provide the spectra on 256 energy bin with and without compensation. In Fig. 5.2 we notice that the entire process on the FPGA for one pixel is divided in two parallel processes. In a) the standard DPP of the signals from the CSA as described in Chapter 2 is represented. The resulting 256 bin PHS obtained with a fast shaper are affected by the unstable response of the detector. The ballistic deficit correction is performed in parallel by the second block (b).

The acquisition sequence for the evaluation of the efficacy of the proposed method, consists in acquiring a sequence of spectra with the two processes a) and b) (Fig.

5.2) during the operation time of the detector. Each spectrum is acquired every 2 minutes for a total duration of 2 hours after biasing the detector. In order to reproduce the same unstable conditions, among each acquisition, the detector was left unbiased for at least 2 hours. Fig. 5.3 represents a diagram of the followed procedure for the spectra acquisition.

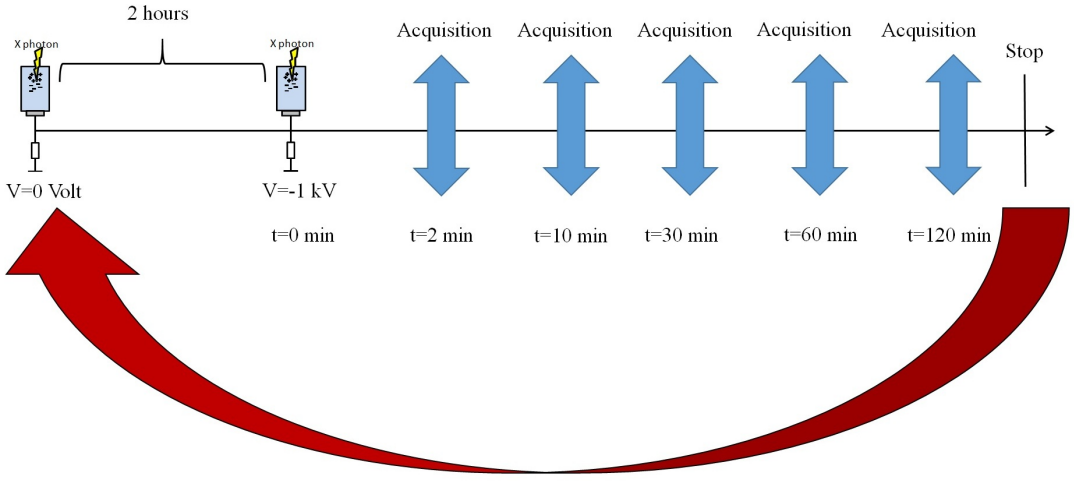

Figure 5.3: Diagram of the spectra acquisition procedure.

The performances of the method were studied both at low and high count rate, following the same procedure. The evaluation of the effectiveness of the correction on the PHS was performed in different ways according to the source (γ or X) used.

5.2 Results under low-flux

For this first test at low flux we used the two γ sources (Fig. 5.1 on the right) of ^{57}Co (E_γ=122 keV) and ^{241}Am (E_γ=59,5 keV) simultaneously for a total count rate of 250 c/s. In this condition the phenomenon of pile-up can be considered as negligible. Fig. 5.4 shows the uncorrected and correct spectra measured with the detector exposed simultaneously to the two γ-sources. The improvement of the stability over time is visible from the pulse height spectra. In the next Section, we will quantify the benefit of the correction method by accurately measuring the position of the photoelectric peak.

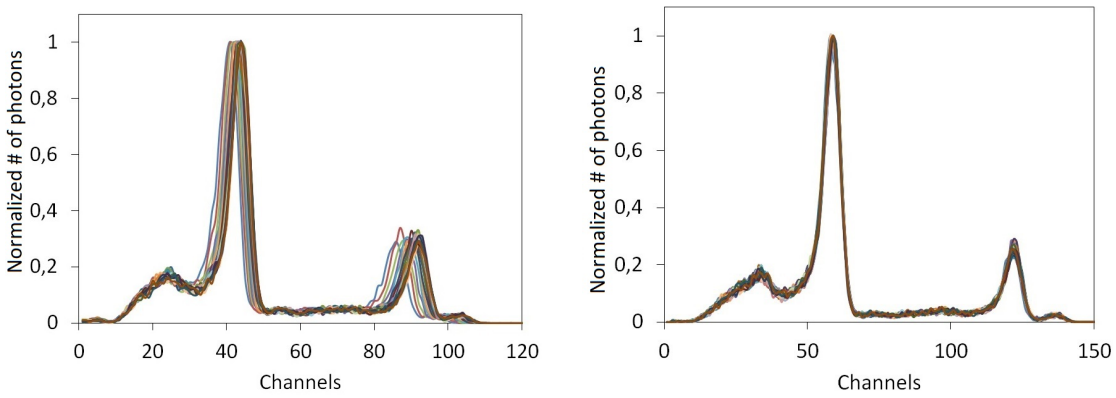

Figure 5.4: Results obtained with the two γ-sources superposed. Pulse height spectra performed with a SDL characterized by a T_D=50 ns before (right) and after (left) applying the compensation algorithm.

5.2.1 Evaluation of the method performances

The test at low count rate shows two important results. First, the stability of the detector response is reached immediately after biasing the system. Fig. 5.5 represents the position of the photoelectric peak over time before and after applying the compensation algorithm. The estimation of the photoelectric peak position is performed with a Gaussian fit on the main photoelectric peaks of the two γ-sources, i.e. at 122 keV for the ^{57}Co and 59,5 keV for the ^{241}Am. In order to evaluate the shift over time of the peak position, this latter was normalized by the final position of the peak, when the detector is stabilized.

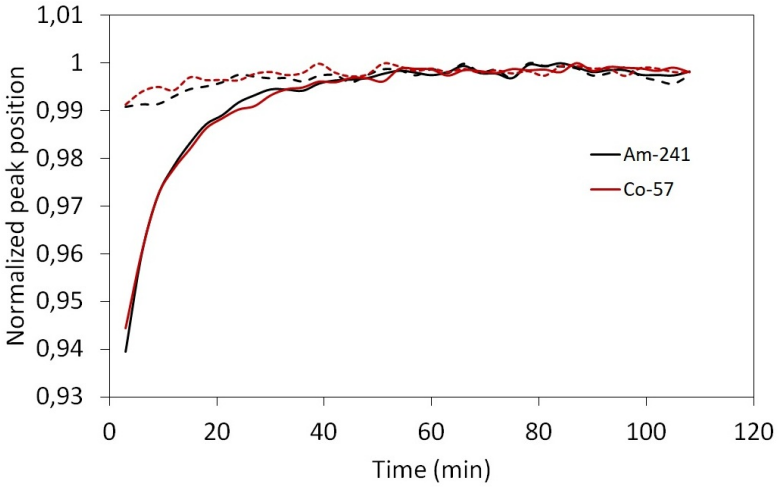

Figure 5.5: Normalized peak position over time of the spectra.

The estimation of the photoelectric peak position was performed for the main energies of the two sources in order to check the coherence of the results obtained.

The results show that before applying the compensation algorithm we have a shift of the photoelectric peaks of 6%, representing a shift of 5 channels. In order to give a temporal estimation of the unstable condition of the detector before and after the correction, we can estimate the time for which the variation of the normalized photoelectric peak position is smaller than 0,5%. From the obtained curves we can then notice that the response stability is reached around 60 minutes after biasing the detector before the correction algorithm is applied and around 7 minutes after the correction. The significant improvement obtained with the proposed method is represented by the important decrease of the shift of the photoelectric peaks over time, represented by only the 1% immediately after biasing the detector. This represents a shift on only 2 channels in the very first minutes of operation.

The second results obtained with this first test is that the energy resolution is almost unchanged. In order to compare the correct value of the measured energy resolution of the system we estimate the (FWHM) from the Gaussian fit for the acquired spectra at t=120 minutes, i.e. the stable one. We observed that the energy resolution is slightly worse when the correction is applied. We have measured that before applying the compensation method the energy resolution is estimated equal to 6,8% at 122 keV and 13,7% at 59,5 keV. When the correction is performed, we find a resolution of 7,4% at 122 keV and 14,1% at 59,5 keV. This slight increase is due to slight fluctuation of the measured correction factor $< \eta'_D >$ performed with the algorithm of the Exponential Moving Average (EMA) discussed in the previous Chapter. This result could be further improved by increasing the number of pulses used for the average calculation and this can be easily achieved at higher count rates.

5.3 Results under high-flux with material

Measurements under X-rays were performed in order to demonstrate that the spectral drift is also corrected at higher count rates. The X-ray tube was set at 160 kV and at different tube currents. In this way we could investigate on the effectiveness of the algorithm proposed at different count rates. Tab. 5.1 summarizes the beam characteristics adopted for this test.

Voltage (kV)	Current (mA)	Count rate (Mc/s)
160	1,5	0,74
160	2,3	1
160	3,5	1,5
160	5	2

Table 5.1: X-ray beams characteristics for the acquisition when the thin layer of W is used.

In this Section we are going to analyse the results obtained when a thin layer of 0,5 mm of Tungsten (W) was superposed to the X-ray beam. The spectrum is characterized by a narrow energy peak below the K-edge energy (69,5 keV) of Tungsten. This peak can be used to accurately measure the spectral drift of the detector. In this way, we can precisely quantify the drift of the detector response over time as well as the efficacy of the correction method. It was used the procedure described in Section 5.1 for the acquisition of the spectra over time. Fig. 5.6 shows the uncorrected and corrected spectra measured with the detector exposed to the X-ray beam at different values of current before and after the correction.

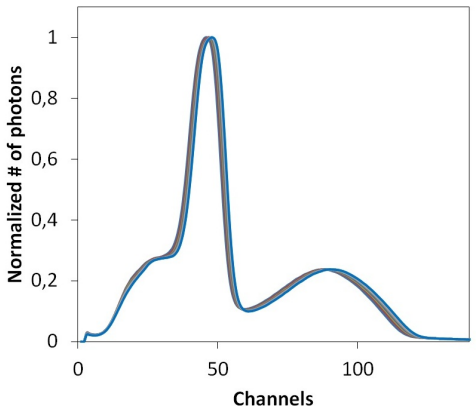

(a) 0,74 Mc/s before correction.

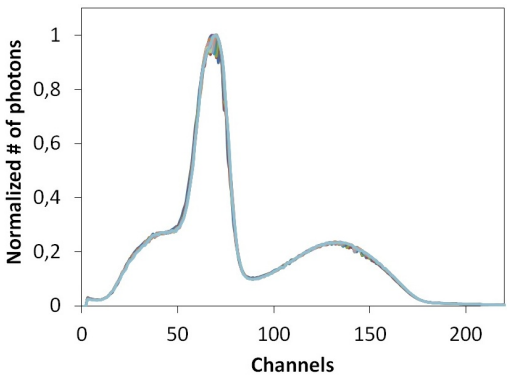

(b) 0,74 Mc/s after correction.

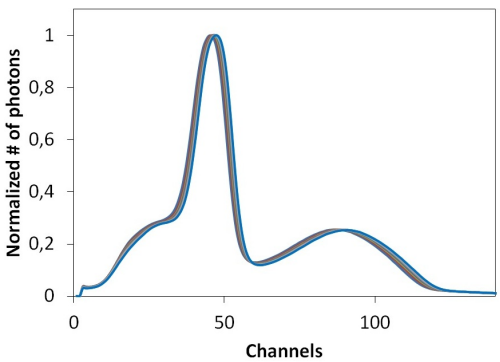

(c) 1 Mc/s before correction.

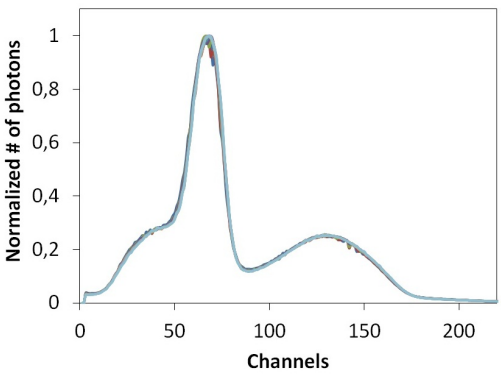

(d) 1 Mc/s after correction.

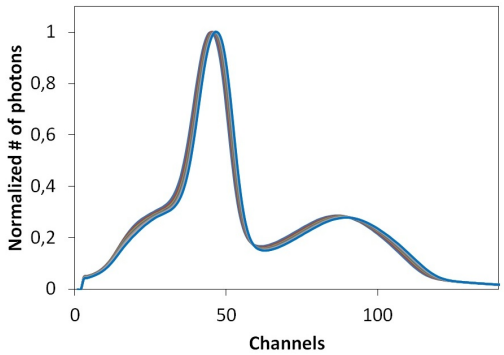

(e) 1,5 Mc/s before correction.

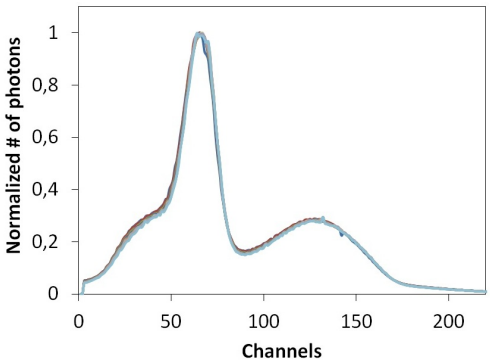

(f) 1,5 Mc/s after correction.

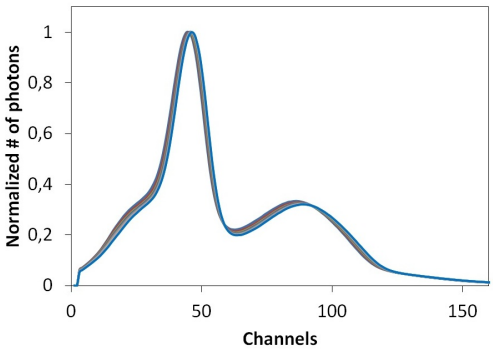

(g) 2 Mc/s before correction.

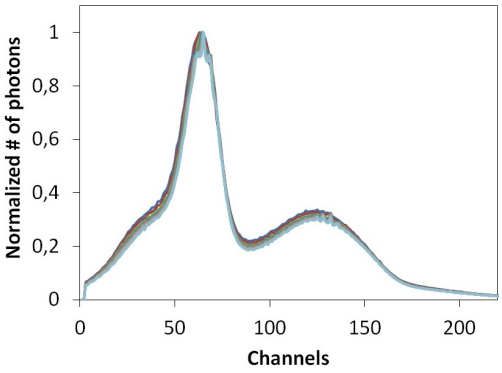

(h) 2 Mc/s after correction.

Figure 5.6: Pulse height spectra from the fast shaping circuit before (left) and after (right) applying the correction algorithm for different count rates involved.

From the pulse height spectra obtained it is possible to notice the effectiveness of the compensation algorithm.

5.3.1 Characterization of the drift for polychromatic spectra

Contrary to γ-sources, it is not possible to estimate the position of the spectra with a Gaussian fit because they are polychromatic spectra. For this reason, in this thesis work, we developed a new method for the characterization of the spectra position over time for polychromatic sources. The method is able to quantify the drift of the unstable spectra, $S_{unstable}$, in relation to a reference spectrum, S_{ref}. Our reference spectrum is recorded at the end of the acquisition sequence when we know that the detector response is stable. After the acquisition, the spectra are normalized on the count rate in order to correctly perform the comparison. After that we fixed an energy window on the reference spectrum equal to $(s_{Nmax} - s_{Nmin})$ where s_{Nmin} represents the lower value of the energy window and s_{Nmax} the upper one. Once the energy window is fixed, the drift is evaluated as follow:

$$D_k(i) = \sum_{s_N min}^{s_N max} |S_{unstable}(i \cdot k) - S_{ref}(i)| \tag{5.1}$$

$$drift = 1 - Argmin(D_k) \tag{5.2}$$

Where k is a parameter introduced for the minimization of the quantity D_k among the unstable spectrum and the reference one in the fixed energy window. This parameter defines the *drift*. Fig. 5.7 represent the concept here described.

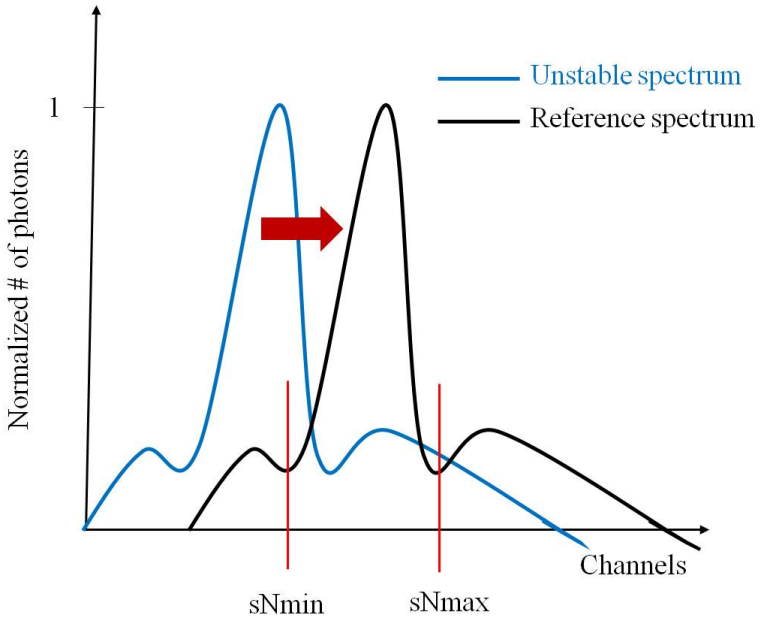

Figure 5.7: Concept of the distance evaluation among stable and unstable spectra.

5.3.2 Evaluation of the method efficiency

In this first study, the method of the spectra position evaluation is performed on the K-edge peaks, as Fig. 5.7 shows. For the uncorrected spectra (left column in Fig. 5.6) s_{Nmin}=40 and s_{Nmax}=70. For the corrected spectra (right column in Fig. 5.6) s_{Nmin}=70 and s_{Nmax}=95. Fig. 5.8 represents the position of the unstable spectra over time compared to the reference spectrum before and after the correction.

With the method for the spectra position evaluation, it is possible to observe that the measurements at different fluxes show that the correction algorithm is efficient at every count rate considered. Before the correction algorithm is applied the position of the normalized peaks over time increases by 4-7% during the first 60 minutes. In order to give a temporal estimation of the unstable condition of the detector before and after the correction, we can evaluate the time for which the

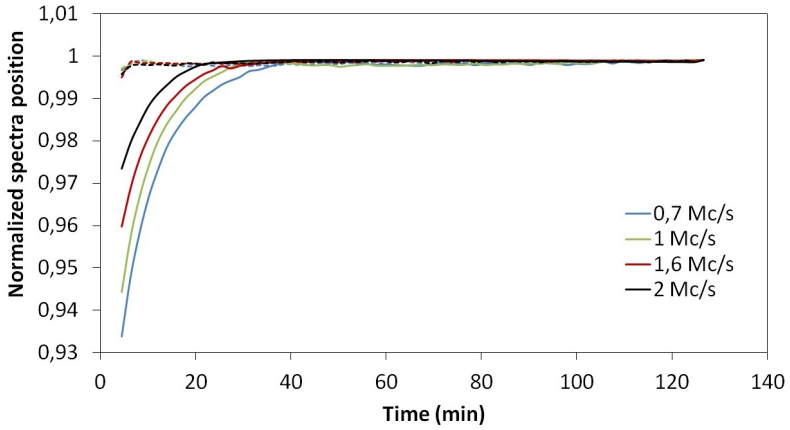

Figure 5.8: Normalized position of the Tungsten K-edge peak at different count rates, before (full lines) and after (dotted lines) ballistic deficit real-time compensation.

variation of the normalized photoelectric peak position is smaller than 0,5%. We can observe that the stability of the detector response is reached at a time t=40 minutes. Once the correction algorithm is applied the stability is reached at a time t=4 minutes. The very interesting result is that the position of the normalized peaks over time varies immediately after biasing the detector of a value smaller than 1% on the range. It is important to notice that these results are obtained without any loss of count rate, since we only apply a multiplicative correction to all pulses of the fast SDL circuit.

5.4 Results under high-flux with direct flux

The last test for the evaluation of the compensation method was performed with a direct flux, i.e. without any filter layers between the detector and the beam. In order to obtain the same count rates as with the Tungsten filter, smaller currents are now applied. Tab. 5.2 summarizes the characteristics of the beam for this last test.

Voltage (kV)	Current (mA)	Count rate (Mc\s)
120	0,06	0,696
120	0,1	1,102
120	0,15	1,537
120	0,21	2

Table 5.2: X-ray beams characteristics for the acquisition with the direct flux.

The same procedure (Section 5.1) was used for the spectra acquisition over time.

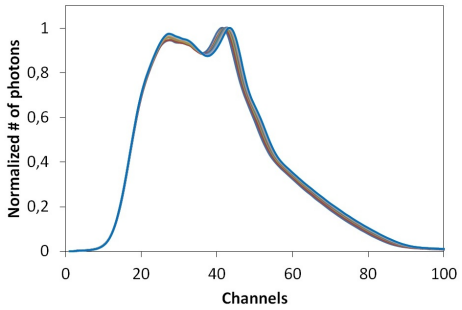

(a) 0,74 Mc/s before correction.

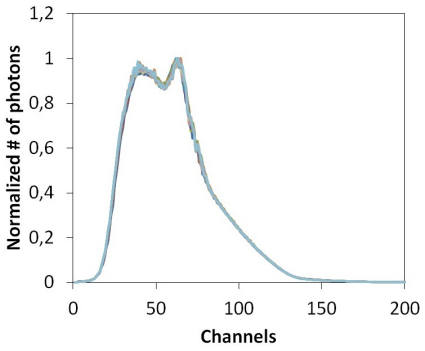

(b) 0,74 Mc/s after correction.

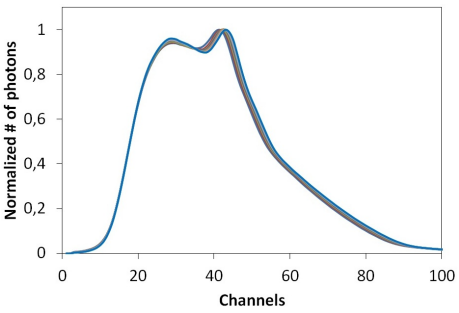

(c) 1 Mc/s before correction.

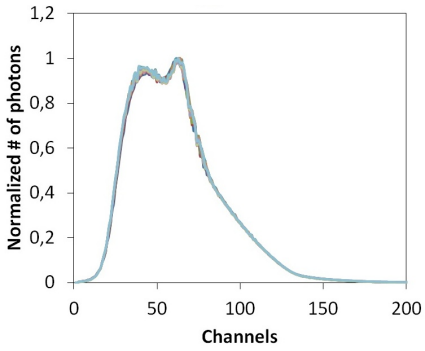

(d) 1 Mc/s after correction.

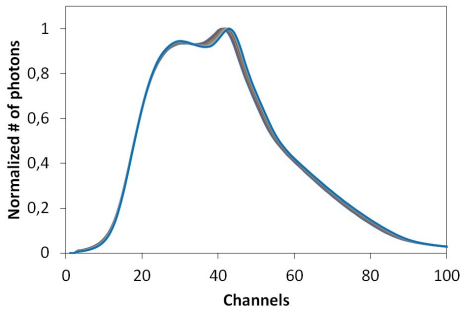

(e) 1,5 Mc/s before correction.

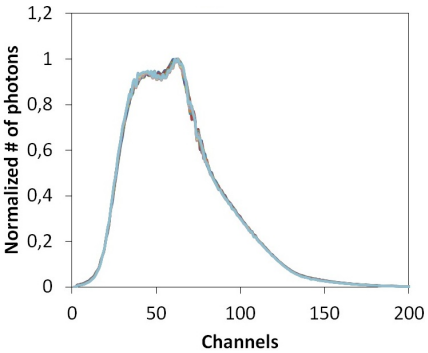

(f) 1,5 Mc/s after correction.

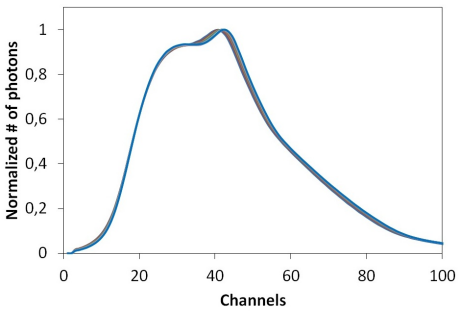

(g) 2 Mc/s before correction.

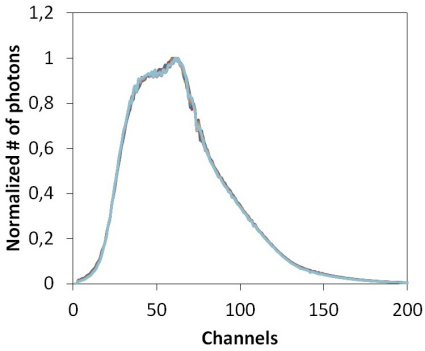

(h) 2 Mc/s after correction.

Figure 5.9: Pulse height spectra from the fast shaping circuit before (left) and after (right) applying the correction algorithm for different count rates involved.

Fig. 5.9 shows the uncorrected and correct spectra measured with the detector exposed to the X-ray beam at different value of currents.

5.4.1 Evaluation of the method efficiency

Because of the broad distribution of the non-attenuated pulse height spectrum, the drift on the channels of the energy spectra is evaluated with the method presented in Section 5.3.1. In this case, we notice the fluorescence lines of tungsten, whose energies ranging from 57 to 70 keV are combined into a single peak observable around channel 50 of the uncorrected spectra. Nevertheless, the use of only this small peak for the estimation of the spectra position was not sufficient for a correct measurement of the factor k in Eq. 5.1. For this reason, in order to estimate the position of the spectra over time compared to a reference spectrum, Eq. 5.1 and 5.2 are applied to the non-zero region of the spectra, i.e. were the value of the spectrum is different from zero. This mean that s_{Nmin}=10 s_{Nmax}=100 for the uncorrected spectra (left column in Fig. 5.9) and s_{Nmin}=25 s_{Nmax}=150 for the corrected one (right column in Fig. 5.9). Fig. 5.10 represents the concept of the drift evaluation for direct flux X-ray beam.

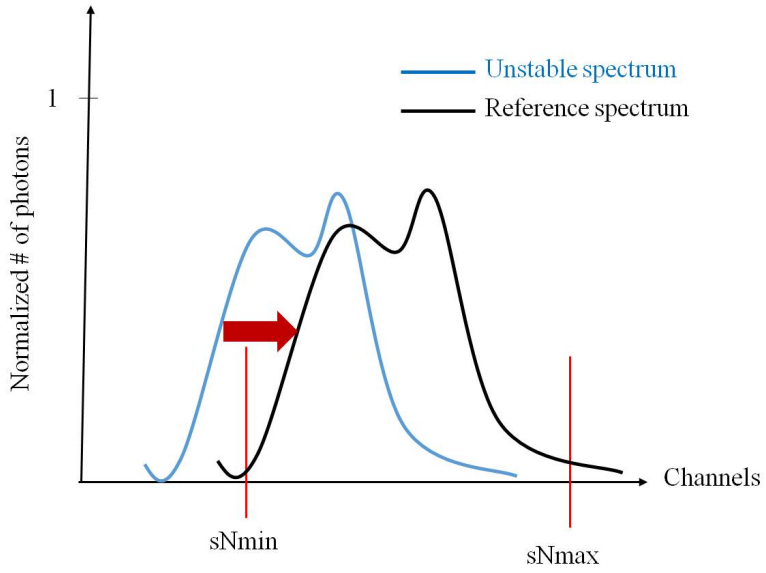

Figure 5.10: Concept of the drift evaluation among stable and unstable spectra.

Once the values of the *drift* are measured for all the spectra before and after apply the correction algorithm, the trend of the spectra position over time is traced. Fig. 5.11 represents the position of the unstable spectra over time compared to the reference spectrum before and after the correction.

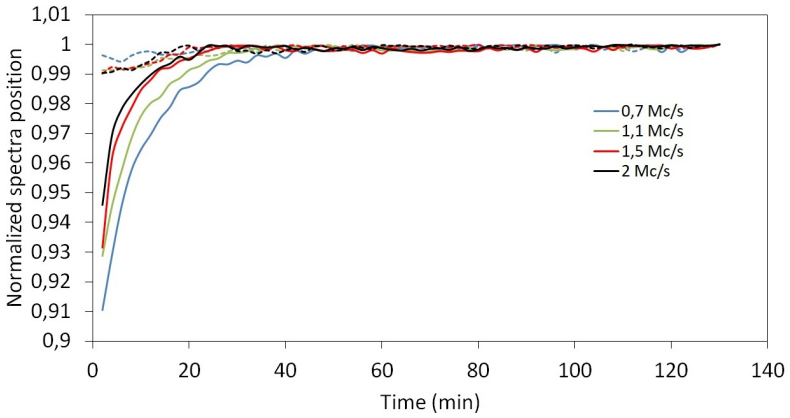

Figure 5.11: Normalized position of the normalized spectra position at different count rates, before (full lines) and after ballistic deficit real-time compensation (dotted lines).

The measurements at different fluxes show that the correction algorithm is efficient at every count rate considered. Before the correction algorithm is applied the position of the normalized peaks over time change of 6-9% on the range. We estimate the time from which the distance to the reference spectrum is less than 0,5% and we observe that before the correction the stability of the detector response is reached 40 minutes after biasing it for all the count rates considered. The same estimation can be done after applying the correction. We observe that the time in which the variation is smaller than 0,5% is only 4 minutes after biasing the detector. Moreover, the shift measured immediately after biasing the detector is smaller than 1%.

5.5 Conclusions and discussions

In this Chapter, we have shown that the ballistic deficit correction method provides a stable detector response over time. The method was validated with experimental measurements performed with γ and X-ray sources at different count rates. The method is based on the measure of the ballistic deficit with a double shaping circuit and perform the compensation of this phenomenon during all the operation time of the detector with a real-time process. The results obtained prove that the real-time correction method is capable to provide a stable response of the detector over time both at low and high count rate.

Measurements with the γ-ray sources show that the the stability of the detector response is reached after only 7 minutes of operation. In the first 7 minutes the estimated drift of the photoelectric peak is smaller than the 1%. Moreover, we

demonstrated that the energy resolution when the stability is reached is almost unchanged.

Measurements with the X-ray source both with the Tungsten material and with direct flux prove the efficiency of the method for count rates up to 2 Mc/s. We observed that once the correction is applied the drift of the spectra over time is reduce from 6% to 1%, immediately after biasing the detector. The stability of the detector response is reached some minutes after biasing the detector, when the drift of the spectra is smaller than 0,5%.

Chapter 6

Conclusion and perspectives

Recently, there is a growing interest for energy resolved photon counting detectors for X-ray imaging application. In this context, CEA-LETI Detector Laboratory has developed a CdTe pixel detector based on an original architecture where the signals of all pixels are continuously digitized and processed with an FPGA able to perform advanced pulse processing algorithms. The detector provides real-time high-energy resolution energy spectra over 256 energy channels. However, under certain conditions, the performances are degraded by stability problems that affect the spectral response of the detector. The goal of this thesis was to develop DPP algorithms to improve the performance and the stability of a spectrometric pixel detector for high-flux X-ray imaging applications.

After a first study of the State Of The Art on PCDs and on the pulse processing algorithms associated to these detectors (Chapter 1), the characterization of the spectrometric pixel detector developed in CEA-LETI in terms of energy resolution and dead-time was performed. We first studied the impact that the shaper has on the performances of the detector (Chapter 2). With this study we demonstrated that working with high fluxes imposes an important compromise between energy resolution and dead-time. Moreover, the study of the detector response stability (Chapter 3) has shown that it is difficult to have good spectrometric performances and a stable response of the detector over time. Detectors operating under high flux require the use of a fast shaping time of the shaper causing the phenomenon of the ballistic deficit. We demonstrated that the amplitude of the ballistic deficit is sensitive to variation of the electrical field profile inside the material. This effect is the cause of a slight increase of the rise-time of the transient signal. The consequence is an unstable response of the detector over time during the first two hours of operation.

This is the reason why a real-time compensation method for the improvement of the unstable response of the detector over time able to preserve its performances in terms of energy resolution and dead-time was developed. In Chapter 4 the principle and the characterization of the proposed method is presented. A double Single Delay Line, characterized by a fast and a slow delay, is used for the measurement of a correction factor η for the compensation of the ballistic deficit on the fast shaper. The measurement of the correction factor cannot be performed on a single pulse because of the noise, and thus the importance of measuring it on a big number of pulses and then average the values measured. Moreover, it was observed that undesirable effects such as pile-up, charge sharing and weighting potential cross-talk, affect the measurement of the correction factor $< \eta >$. For this reason, the rejection of these events is performed with a consequent improvement on the measurement accuracy of $< \eta >$ and thus on the compensation of the ballistic deficit.

The correction method was then implemented on the FPGA, after some adaptations. Experimental test at low and high flux were finally performed for the validation of the proposed method (Chapter 5). The results obtained show that the compensation of the ballistic deficit is well performed by the proposed algorithm. The stability of the detector response over time is reached and the performances in terms of energy resolution and dead-time are preserved.

Further tests and improvements have to be conducted to complete the characterization of the proposed method. At first, the behaviour of the correction method has to be tested under higher fluxes, e.g. 10^7 c/s or more. Once the limit of the algorithm is tested it is possible to investigate different methods for the rejection of undesirable effect for the measurement of the correction factor $< \eta >$. Finally it will be necessary to evaluate the efficiency of the method with regard to the final applications, in order to demonstrate that the detrimental effects on image quality, material discrimination performance or the induction of reconstruction artefacts in Computed Tomography (CT) applications will be effectively corrected.

The encouraging results obtained with the proposed method open new perspectives for different approaches. The architecture developed is adapted for 1D-linear detectors but the big challenge is to adapt it for 2D-matrix detectors. The various digital processing methods for the correction of the pile-up or charge sharing performed in FPGA were adapted for the implementation inside the pixel. The implementation of the ballistic deficit correction method in the same way is the challenging task. The two SDL can be represented by two delay circuits, the average can be thought as

an RC and the multiplication is simply a gain. On the other hand, these operations are difficult to perform in a pixel with a small size of 1 mm^2. For this reason, other type of solutions have to be found for a correct implementation of the method inside the pixel.

This method was developed because we work with a fixed geometry spectrometric pixel detector. A possible way to solve instability problems of the detector response is to improve the proprieties of the semiconductor material. As we studied in Chapter 3 it is also possible to optimise the geometry of the sensor in order to minimize or better remove, the phenomenon of the ballistic deficit. The compromises with the geometry optimisation is sometimes to increase phenomena such charge sharing.

Acknowledgements

Well.. The end of this special trip called PhD came to the end. I must mentioned all those people who made this experience unforgettable.

First of all I am grateful to the jury who came from far or close to assist to my thesis defense. A big thank you to Mr. Abbene, Mr. Ban, Mr. Calmon and Mr. Collot who had time to read and revise my thesis work and spent their time to assist to the final defense.

A rightful thanks goes to my supervisors Andrea and Olivier who suggested me and encouraged me during all these three years. Thanks to Sylvain too, who had the big patience to help and teach me some tricks of coding and how to face the PhD itself. A huge thanks to Patrice who shared with me my entire stay in the laboratory and teach me the basis of the job-life: "Un bon chef, c'est un chef mort".

And related to this... Thanks to Loick who permits to be part of the ex-LDET and to Sophie, even if we share only the very last months of my thesis.

Thanks to the colleagues and friends such as Pierre-Antoine, known as Jean-Pierre, who shared with me all the three years of thesis, Odran, who shared beers and super funny chats with me, Vera, Artur, all the other PhDs and the ones who only passed in the laboratory but they are still in my life: Kenza, Anne, Carlos and Daniel.

Thanks to all the others of the ex-LDET, starting from my corridor with Olivier and his "Bonjour" and "Bonsoir", Guillaume and Marcos. Thanks to the daily chats I had with Jean-Michel who let my stay less hard the first months talking to me in my native language. Thanks to Vincent for your sympathy and the little dog... it is still with me. Thanks to Caroline with her dynamic and smiley personality. Thanks for the interesting exchanges with Murielle, Marie-Claude and our chats about the future and life. Last but not the least, thanks to the "MA" and the smile of Michel.

I would really like to thank you because from all of you I learned a culture and I think it is the best gift someone can give to a person. Merci beaucoup à tous et toutes!
A special thanks goes to all of my friends. The ones who are in my life since years, the ones who are new in my life and also the ones who only passed for a short period. I should write a poem for some of you but no, thank you with all my heart summarizes very well my love for all of you. You helped me to enjoy this experience and appreciate everything of the PhD's life.

Last but not the least, thanks to my amazing family who supports me in my choices even when sometimes they didn't agree and for their presence in my daily life even at kms far away from me. Talking of family... thanks to my boyfriend and partner in life, you are a fixed point in my life, a friend, a partner, a supporter. Thanks for the patience and love you give me everyday.

Thanks to all those people who let this trip less hard and full of personal and professional richness!

Bibliography

[1] T. Takahashi and S. Watanabe, "Recent progress in CdTe and CdZnTe detectors", IEEE Transaction on Nuclear Science, 48(4), 2001.

[2] K. Taguchi, and Iwanczyk, "Vision 20/20: Single photon counting x-ray detectors in medical imaging", Med. Phys, No. 10, 2013.

[3] S. Mikkelsen, D. Meier, G. Maehlum, P. Oya, B. Sundal and J. Talebi, "An ASIC for multi-energy X-ray counting", IEEE Nucl. Sci. Symp. Conf. Rec., 1996.

[4] R. Ballabriga et al., "Medipix3: a 64 k pixel detector readout chip working in single photon counting mode with improved spectrometric performance", Nucl. Instrum. Meth. A 633, 2011.

[5] R. Ballabriga et al., "Review of hybrid pixel detector readout ASICs for spectroscopic X-ray imaging", JINST, 2016, P01007.

[6] Geronimo et al., "ASIC with multiple energy discrimination for high-rate photon counting applications", IEEE Trans. Nucl. Sci. 54, 2007.

[7] J.S. Iwanczyk et al., "Photon counting energy dispersive detector arrays for X-ray imaging", IEEE Trans. Nucl. Sci. 56, 2009.

[8] G. Gerardi, L. Abbene, "A digital approach for real time high-rate high resolution radiation measurements", Nuclear Instruments and Methods in Physics Research A 768, 46–54, 2014.

[9] A. Brambilla, P. Ouvrier-Buffet, J. Rinkel, G. Gonon, C. Boudou and L. Verger, "CdTe linear pixel X-ray detector with enhanced spectrometric performance for high flux X-ray imaging", IEEE Transaction Nuclear Science, Vol. 59, No. 4, 2012.

[10] A. Brambilla et al., "Fast CdTe and CdZnTe semiconductor detector arrays for spectroscopic X-ray imaging", IEEE Transaction Nuclear Science, Vol. 60, No. 1, 2013.

[11] A. Brambilla, A. Gorecki, A. Potop, C. Paulus, L. Verger, "Basis material decomposition method for material discrimination with a new spectrometric X-ray imaging detector", Journal of Instrumentation, 12 (8), art. No. P08014, 2017.

[12] K. Wells and D. A. Bradley, "A review of X-ray explosive detection techniques for checked baggage", Appl. Radiat. Isot. 70, 2012.

[13] V. Rebuffel, J. Rinkel, J. Tabary and L. Verger, "New perspectives of X-ray techniques for explosive detection based on CdTe/CdZnTe spectrometric detectors", Int. Symp. Digit. Ind. Radiol. Comput. Tomogr. 2, 2011.

[14] P .M. Shikhaliev, "Soft tissue imaging with photon counting spectroscopic CT", Phys. Med. Biol. 60, 2015.

[15] A. Potop, V. Rebuffel, J. Rinkel, A. Brambilla, F. Peyrin and L. Verger, "Investigation of the polynomial approach for material decomposition in spectral X-ray tomography using an energy-resolved detector", Proc. SPIE 9033, 2014.

[16] C. O. Schirra, B. Brendel, M. A. Anastasio and E. Roessl, "Spectral CT: a technology primer for contrast agent development", Contrast Media Mol. Imaging 9, 62, 2014.

[17] G.F. Knoll, "Radiation detection and measurements", John Willey and Sons, Inc., New York 2000.

[18] F. S. Goulding, D. A. Landis, "Ballistic deficit correction in semiconductor", IEEE Transactions on Nuclear Science, Vol. 35, No. 1, 1988.

[19] F. S. Goulding et al., "GAMMASPHERE, elimination of ballistic deficit by using a quasi-trapezoidal pulse shaper", IEEE Transaction on Nuclear Science, Vol. 40, No. 4, 2002.

[20] M. Moszynski and G. Duchêne, "Ballistic deficit correction methods for large Ge detectors", Nuclear Instruments and Methods In Physics Research, Vol. 308, No. 3, 1991.

[21] M. Salathe, T. Kihm, "Optimized digital filtering techniques for radiation detection with HPGe detectors", arXiv:1504.02039 [physics.ins-det], 2015.

[22] M. J. Yaffe and J. A. Rowlands, "X-ray detectors for digital radiography", Phys. Med. Biol. 42, 1997.

[23] R. Chen et al., "Readout of scintillator light with avalanche photodiodes for positron emission tomography", Nuclear Instruments and Methods in Physics Research Section A, Vol. 433, No. 3, 1999.

[24] M. Spahn, V. Heer, R. Freytag, "Flat-panel detectors in X-ray systems", NCBI, PubMed, 43(5):340-50, 2003.

[25] M. Chabbal et al., "New CsI/a-Si 17"x17" X-ray flat-panel detector provides superior directivity and immediate direct digital output for general radiography systems", NCBI, PubMed, 19(4): 362–370, 1998.

[26] T. Schulman, "Si, CdTe and CdZnTe radiation detectors for imaging applications", Thesis at University of Helsinki, Finland, 2006.

[27] S. O. Kasap and J. A. Rowlands, "Direct-conversion flat-panel X-ray image detectors", Proceeding Circuits Devices System, Vol. 149, No. 2, 2002.

[28] P. Delogu et al., "Characterization of Pixirad-1 photon counting detector for X-ray imaging", Journal of Instrumentation, doi:10.1088/1748-0221/11/01/P01015, 2016.

[29] Website "https://medipix.web.cern.ch/".

[30] T. Takahashi et al., "High-resolution CdTe detector and applications to imaging devices", IEEE Transactions on Nuclear Science, 48(3 I), 287-291. DOI: 10.1109/23.940067, 2000.

[31] L. Zhang, Y. Li, X. Zheng et al., "Multi-energy detection using CdZnTe semiconductor detectors", Proc IEEE NSS, pp. 428-433, 2008.

[32] K. Taguchi, and Iwanczyk, "Vision 20/20: Single photon counting x-ray detectors in medical imaging", Med. Phys, Vol. 40, No. 10, 2013.

[33] J. P. Schlomka et al., "Experimental fea-sibility of multi-energy photon-counting K-edge imaging in pre-clinical computed tomography", Physics in Medicine and Biology, vol. 53, no. 15, pp. 4031–4047, 2008.

[34] S. Basolo et al., "Application of a hybrid pixel detector to powder diffraction", Journal of Synchrotron Radiation, 14, 151–157, 2007.

[35] X. Llopart, M. Campbell "First Test Measurements of a 64k Pixel Readout Chip Working in Single Photon Counting Mode" Nucl. Instrum. Methods A, Vol. 509, No. 1–3, 2003.

[36] N.A. van Bakel et al., "Timepix detector at the X-ray Correlation Spectroscopy instrument at LCLS", Journal of Physics: Conference Series, 425-062011, 2013.

[37] R. Ballabriga et al., "Review of hybrid pixel detector readout ASICs for spectroscopic X-ray imaging" JINST 11 P01007, 2016.

[38] E. N. Gimenez, R. Ballabriga et al., "Study of charge-sharing in MEDIPIX3 using a micro-focused synchrotron beam", Journal of Instrumentation, Vol. 6, 2011.

[39] W. Barber et al., "Characterization of a novel photon counting detector for clinical CT: count rate, energy resolution, and noise performance", Medical Imaging, Vol. 7258, 2009.

[40] R. Steadman et al., "ChromAIX: a high-rate energy-resolving photon-counting ASIC for spectal computed tomography", Proc. SPIE 7622, 762220, 2010.

[41] S. Kappler et al., "A research prototype system for quantum-counting clinical CT", Proceeding SPIE, Vol. 7622, 2010.

[42] Website MULTIX, "http://www.multixdetection.com/".

[43] A. Brambilla, A. Gorecki, A. Potop, C. Paulus, L. Verger, "Basis material decomposition method for material discrimination with a new spectrometric X-ray imaging detector", Journal of Instrumentation, 12 (8), art. no. P08014, 2017.

[44] S. Lux et al., "Study of experimental performances at various fluence rates on CdTe spectrometric imaging detector",IEEE Transaction on Nuclear Science, Vol. 978, No. 1, 2016.

[45] D. Perion et al., "Material discrimination and imaging improvement using high count rate X-ray spectrometric detector for non-destructive testing and security applications", IEEE Transaction on Nuclear Science, Vol. 978, No. 1, 2016.

[46] L. Abbene, G. Gerardi, "Digital performance improvements of a CdTe pixel detector for high flux energy-resolved X-ray imaging", Nuclear Inst. and Methods in Physics Research, A, Volume 777, p. 54-62, (2015).

[47] A. Peizerat et al., "A 256 energy bin spectrum X-ray photon-counting image sensor providing 8Mcounts/s/pixel and on-chip charge sharing, charge induction and pile-up corrections", Proceeding IEEE-Symposium on VLSI Circuits, 2017.

[48] Z. He et al., "Review of the Shockley-Ramo Theorem and its Application in Semiconductor Gamma-Ray Detectors", Nucl. Instr. Meth., Vol. 463, No. 1–2, pp. 250-267, 2001.

[49] W. Shockley, "Currents to conductors induced by a moving point charge" J. Appl. Phys., 1938.

[50] S. Ramo, "Currents induced by electron motion", Proc. IRE, 1939.

[51] M.C. Veale, S.J.Bell, D.D.Duarte, A.Schneider, P.Seller, M.D.Wilson, K. Iniewski, "Measurements of charge sharing in small pixel CdTe detectors", Nuclear Instruments and Methods in Physics Research, 218–226, 2014.

[52] A. Brambilla et al., "CdTe Linear Pixel X-Ray Detector With Enhanced Spectrometric Performance for High Flux X-Ray Imaging", IEEE Transaction on Nuclear Science, Vol. 59, No. 4, 2012.

[53] A. Brambilla et al., "Fast CdTe and CdZnTe Semiconductor Detector Arrays for Spectroscopic X-Ray Imaging", IEEE Transactions on Nuclear Science, Vol. 60 ,No 1, 2013.

[54] A. Brambilla et al., "CdTe linear pixel X-ray detector with enhanced spectrometric performance for high flux X-ray Imaging", IEEE Nuclear Science Symposium Conference Record, 978-1, 2011.

[55] K. Mathieson et al., "Charge sharing in silicon pixel detectors", Nuclear Instruments and Methods in Physics Research, Vol. 487, No. 1–2, 2012.

[56] S. Abdalla et al., "Circuit implementation of mechanism for charge-sharing suppression for photon-counting pixel arrays", Nuclear Instruments and Methods in Physics Research, 2006.

[57] R. Ballabriga et al., "The Medipix3 Prototype, a Pixel Readout Chip Working in Single Photon Counting Mode With Improved Spectrometric Performance", IEEE Transaction on Nuclear Science, Vol. 54, No. 5, 2007.

[58] R. Ballabriga et al., "Characterization of the Medipix3 pixel readout chip", Journal of Instrumentation, 6-C01052, 2010.

[59] M. C. Veale et al., "An ASIC for the Study of Charge Sharing Effects in Small Pixel CdZnTe X-Ray Detectors", Transaction on Nuclear Science, Vol.58 ,No. 5, 2011.

[60] M. C. Veale et al., "Measurements of charge sharing in small pixel CdTe detectors", Nuclear Instruments and Methods in Physics Research, Vol. 767, 2014.

[61] L. Abbene et al., "Digital fast pulse shape and height analysis on cadmium–zinc–telluride arrays for high-flux energy-resolved X-ray imaging", Journal of Synchrotron Radiation, 25(Pt 1):257-271, 2018.

[62] R. Ballabriga et al., "The Medipix3RX: a high resolution, zero dead-time pixel detector readout chip allowing spectroscopic imaging", Journal of Instrumentation, 8 C02016, 2013.

[63] G. Hall et al., "The deconvolution method for fast pulse shaping at hadron colliders", Nucl. Instrum. Methods, Vol. 320, No. 1–2, 1994.

[64] M. W. Raad et al., "A novel approach for pileup detection in gamma-ray spectroscopy using deconvolution", Measurement Science and Technology, 19 065601, 2008.

[65] R. J. Komar, H. B. Mak, "Digital signal processing for BGO detectors", Nuclear Instruments and Methods in Physics Research, Vol. 336, No. 1–2, 1993.

[66] S. Marrone et al., "Pulse pile-up and dead time corrections for digitized signals from a BaF calorimeter", IEEE Nuclear Science Symposium, Vol. 768, 2004.

[67] T. Oishi, M. Baba, "Development of Pile-up Separation Method Using Digital Signal Processing", Journal of Nuclear Science and Technology, Vol. 45, No. 5, 2008.

[68] M. D. Haselman et al., "FPGA-Based Pulse Pile-Up Correction With Energy and Timing Recovery", IEEE Transaction Nuclear Science, Vol. 59, No. 5, 2012.

[69] F. Belli et al., "Application of a digital pileup resolving method to high count rate neutron measurements", Review of Scientific Instruments, 79(10):10E515, 2008.

[70] M. Nakhostin et al., "A digital method for separation and reconstruction of pile-up events in germanium detectors", Review of Scientific Instruments,81(10):103507 , 2010.

[71] I. Mahmoud et al., "Pile-up recovery algorithms for digital gamma ray spectroscopy", Journal of Instrumentations, 7 P09013, 2012.

[72] D. Lee, K. Park, K. T. Lim and G. Cho, "Energy-Correction Photon Counting Pixel for Photon Energy Extraction under Pulse Pile-up", Nuclear Inst. and Methods in Physics Research, Vol. 856, Pages 36-46, 2017.

[73] D. Lee, K. Park, K. T. Lim and G. Cho, "A new cross-detection method for improved energy-resolving photon counting under pulse pile-up", Nuclear Inst. and Methods in Physics Research, Volume 867, Pages 154-162, 2017.

[74] A. S. Wang et al., "Pulse pileup statistics for energy discriminating photon counting x-ray detectors", Nuclear Inst. and Methods in Physics Research, 38(7):4265-75, 2012.

[75] A. Dragone et al., "The PDD ASIC: highly efficient energy and timing extraction for high-rate applications", IEEE Nuclear Science Symposium Conference Record, N16-7, 2006.

[76] M. W. Raad, L. Cheded "Novel Peak Detection Algorithms for Pileup Minimization in Gamma Ray Spectroscopy", IMTC 2006 - Instrumentation and Measurement Technology Conference, Sorrento, Italy 24-27 April, 2006.

[77] Y. Valenciaga et al., "Matched filter for event identification and processing in PET", IEEE Instrumentation and Measurement Technology Conference Proceedings, Mll-2, 2012.

[78] G. Sharma et al., "X-ray spectroscopy technique for the pile-up region", arXiv:1512.08399 [physics.ins-det], 2015.

[79] H. Kun et al., "An FPGA-Based Pulse Pile-up Rejection Technique for Photon Counting Imaging Detectors", Chinese Physics Letters, Vol. 32, No. 3, 2015.

[80] Z. Gu et al., "A New Pulse Pileup Rejection Method Based on Position Shift Identification", IEEE Transactions on Nuclear Science, Vol.3, No. 1, 2016.

[81] L. Abbene, G. Gerardi, F. Principato, "High-rate dead-time correction in a general purpose digital pulse processing system", Journal of Synchrotron radiation, 22(Pt 5): 1190–1201, 2015.

[82] S. M. Hinshaw, D. A. Landis, "A practical approach to ballistic deficit correction", Nuclear Inst. and Methods in Physics Research, Vol.37, No. 2 1990.

[83] V. Radeka, "Low noise techniques in detectors", Annual Review Nuclear Particle Science, Vol. 38:217-277, 1988.

[84] A. Brambilla, C. Boudou, P. Ouvrier-Buffet, F. Mougel, G. Gonon, J. Rinkel, L. Verger, "Spectrometric Performances of CdTe and CdZnTe Semiconductor Detector Arrays at High X-ray Flux", IEEE Nuclear Science Symposium Conference Record, 2009.

[85] V.T. Jordanov, GF Knoll, "Digital synthesis of pulse shapes in real time in high resolution radiation spectroscopy", Nucl. Instrum. Methods A, vol. 345, pp. 337-345, 1994.

[86] O. Alirol, "Simulation d'un détecteur CdTe:Cl de rayonnement X en mode comptage a fort flux pour la radiographie et la tomographie", PhD thesis at Insitut National des Sciences Appliquees de Lyon, 2010.

[87] L. Rossi, P. Fischer, T. Rohe, N. Wermes, "Pixel detectors – From fundamentals to applications", Spinger, 2005.

[88] P. Grybos "Front-end Electronics for Multichannel Semiconductor Detector Systems", EuCARD Editorial Series on Accelerator Science and Technology, vol 8, 2012.

[89] H.H. Barrett et al., "Charge Transport in Arrays of Semiconductor Gamma-Ray Detectors", Phys. Rev. Lett., vol. 75, no. 1, pp. 156-159, 1995.

[90] S.E. Anderson et al., "Digital waveform analysis techniques for pixelated semiconductor detectors", NSS Conference Record, N24-344, 2007.